HOKKAIDO UNIVERSITY

Title	Studies on the tropospheric and stratospheric water vapor measurements for climate monitoring
Author(s)	杉立, 卓治
Degree Grantor	北海道大学
Degree Name	博士(環境科学)
Dissertation Number	甲第11343号
Issue Date	2014-03-25
DOI	https://doi.org/10.14943/doctoral.k11343
Doc URL	https://hdl.handle.net/2115/55416
Type	doctoral thesis
File Information	Takuji_Sugidachi.pdf

Hokkaido University Collection of Scholarly and Academic Papers : HUSCAP

Studies on the tropospheric and stratospheric water vapor measurements for climate monitoring

Takuji Sugidachi

Graduate School of Environmental Science,
Hokkaido University

February 2014

Abstract

Atmospheric water vapor plays a critical role in the climate system because it acts as a medium for heat exchange and transport, and because it is linked to the formation of clouds and precipitation. It is also the most dominant greenhouse gas. Thus, it is important to monitor and understand long-term variability in atmospheric water vapor in the upper troposphere and lower stratosphere.

Routine radiosonde observations provide the longest record of upper-air conditions. However, it is known that the original radiosonde record contains various errors and inhomogeneity because of changes in instrumentation. In this study, the author investigates the measurement uncertainty of the Meisei RS-06G. Comparisons of relative humidity (RH) measurements from the RS-06G radiosonde and from a chilled mirror hygrometer revealed that the RS-06G RH shows a stepwise change of ~3% RH at 0 °C (drying when air temperature decreasing). This is due to a discontinuous correction factor in the processing software that compensates for the temperature dependence of the RH sensor. Using the results from chamber experiments, the author develops a new temperature-dependence (T-D) correction scheme to resolve the artificial stepwise change at 0 °C. Because the RS-06G radiosonde is a successor to the Meisei's previous radiosonde, RS-01G and RS2-91, on which the same RH sensor material had been installed since July 1999, the new T-D correction should be applied to the data obtained by these radiosondes as well. Here, the author applies the new correction into the data at Japan Metrological Agency's Sapporo and Tateno stations. Because the present (original) T-D correction has only been applied only since February 2003, the time series of RH at both stations show apparent large downward trends between 1999

and 2009. The new T-D correction is found to result in a much smaller (mostly negligible) downward RH trend at Sapporo and almost no trend at Tateno.

Because the operational radiosonde observation is designed to obtain the lower tropospheric water vapor for weather forecasting, the RH sensors on operational radiosondes have very poor response in and above the upper troposphere. To measure water vapor precisely in the upper troposphere and stratosphere, special research-quality instruments are required. For example, the Cryogenic Frostpoint Hygrometer (CFH) is regarded as a reference instrument for balloon-borne water vapor observation. However, the CFH needs cryogen material for the observation, and the cryogen material has a strong greenhouse effect. Meanwhile, the Meteolabor Snow White is a Peltier-based chilled mirror hygrometer, which needs no cryogen. Although the operation is simple and environmentally-friendly, it is known that the Snow White cannot measure the stratospheric water vapor even within the cooling capability. In this study, a Peltier-based digitally-controlled chilled-mirror hygrometer has been developed to measure atmospheric water vapor accurately. The developed instrument is environmentally-friendly in nature because this instrument does not use a cryogenic material in addition to a merit of easy-to handle. Also, this instrument has an advanced feedback controller and algorithm to maintain the condensate on the mirror because of the digital circuit. Since January 2011, the author has conducted nine test flights to evaluate the performance. The results showed that the developed instrument can measure water vapor from the surface to the lower stratosphere (~25km). The results of simultaneous measurements with the CFH showed that the frost point temperature from the

developed instrument is consistent with that from CFH within ~0.5 K throughout the troposphere.

Also, several chamber experiments were conducted to investigate the behavior of chilled-mirror hygrometers. The observation of the condensate by a microscope shows that more and smaller ice crystals are formed on the mirror at lower temperatures. Because the evaporation/condensation rates depend on the particle size as well as water vapor content in the ambient air, the response time and the stability of chilled-mirror hygrometers are considered to depend on the particle size on the mirror, water vapor concentration, and the value of the feedback gain to maintain the constant condensate amount. Based on the experimental results, the author discusses the measurement uncertainty of developed chilled-mirror hygrometers.

Contents

1. Introduction ------ 5

1.1 Atmospheric water vapor

1.2 Lower tropospheric water vapor measurements

1.3 Upper tropospheric and lower stratospheric water vapor measurements

1.4 Water vapor observation requirement

1.5 Structure of the thesis

2. Measurement uncertainty of operational upper-air observations. ------ 22

2.1 Radiosonde history and artificial changes at the JMA stations.

2.2 Correction of the stepwise change at 0 °C in Meisei RS2-91, RS-01G, and RS06G radiosonde relative humidity

2.3 Impact of the proposed correction on historical humidity data at the JMA stations

3. Development of a Peltier-based chilled-mirror hygrometer ------ 64

3.1 Chilled-mirror hygrometry

3.2 Instrument development description

3.3 Test flights

3.4 Condensate on the mirror

3.5 Measurement uncertainty

3.6 Discussion of the issue/problems on the Snow White hygrometer

3.7 Summary and concluding remarks

4. Summary ------ 114

Appendix ------ 117

Acknowledgment ------ 126

Reference ------ 127

Chapter 1
Introduction

1.1 Atmospheric water vapor

Atmospheric water vapor plays a critical role in the climate system because it acts as a medium for heat exchange and transport, and because it is linked to the formation of clouds and precipitation. It is also the most dominant greenhouse gas, accounting for about 60% of the natural greenhouse effect under the clear sky condition, and provides the largest positive feedback in model projections of climate change (Held and Soden 2000). Thus, it is important to monitor and understand long-term variability in atmospheric water vapor in the upper troposphere and lower stratosphere.

Water vapor is a highly variable gas. The tropospheric water vapor concentration depends strongly on air temperature (and thus location and altitude). The near-surface air includes much water vapor, and the water vapor content typically reduces with height in the troposphere (Fig. 1.1). On the other hand, water vapor in the stratosphere is extremely dry (Fig. 1.2), because tropospheric air enters the stratosphere typically through the very cold (~-80˚C) tropical tropopause (Brewer 1949).

There are several expressions for the water vapor content, including vapor pressure, dew-point or frost point temperature, relative humidity (RH), mass or volume mixing ratio, and specific humidity. Using physical relationships, it is possible to convert one to the others. The Clausius-Clapeyron equation provides an

expression for the boundary curve of phase equilibrium in the pressure-temperature (p-T) plane. Mathematically, it is written as

$$\frac{d\ln p}{dT} = \frac{\mathrm{L(T)}}{RT^2} \tag{1.1}$$

where L(T) is the latent heat as a function of temperature T, and R is the molecular gas constant of water vapor. Based on experimental data, several empirical equations are developed for the temperature – water vapor pressure relationship (Murphy and Koop 2005). Saturation water vapor pressure e_w of pure water vapor with respect to liquid water is the pressure of the vapor when in a state of neutral equilibrium with a plane surface of pure liquid water at the same temperature and pressure. Similarly, e_i stands for the water vapor pressure with respect to ice. e_w and e_i are functions of temperature only, namely:

$$e_w = e_w(T)$$
$$e_i = e_i(T) \tag{1.2}$$

Although e_w and e_i are needed to correct for the mixture of dry air using an enhancement factor $f(T,p)$ to obtain saturation vapor pressure e'_w, e'_i of moist air, in the meteorological range of pressure and temperature e'_w, or e'_i are almost equal to e_w,or $e_i$with an error of 0.5 percent or less (Buck 1981; Murphy and Koop 2005). Using these equations, dew point temperature T_d or frost-point temperature T_f is converted into the partial pressure of water vapor, $e(T_d)$ or $e(T_f)$. When air temperature T_{air} is given, we can calculate the relative humidity (RH) by using the following equations. When T_d is given,

$$\mathrm{RH} = \frac{e_w(T_d)}{e_w(T_{air})} \times 100\% \,, \tag{1.3}$$

and when T_f is given,

$$\mathrm{RH} = \frac{e_i(T_f)}{e_w(T_{air})} \times 100\% \,. \tag{1.4}$$

It should be noted that RH at temperature less than 0˚C is often evaluated with respect to water (WMO, 2008). In the upper troposphere/lower stratosphere (UT/LS) science community, RH with respect to ice, RH_i is also used as

$$\mathrm{RH_i} = \frac{e_i(T_f)}{e_i(T_{air})} \times 100\%. \tag{1.5}$$

The specific humidity (SH), which is mass concentration or moisture content of moist air is the ratio of the mass of water vapor m_v to the total mass (the sum of dry air m_a and m_v) is defined as

$$\mathrm{SH} = \frac{m_v}{m_v + m_a} \,. \tag{1.6}$$

The volume mixing ratio χ is written as

$$\chi = \frac{e}{P} \times 10^6 \text{ [ppmv(parts per million by volume)]} \tag{1.7}$$

where P is air pressure.

1.2 Lower tropospheric water vapor measurements

Water vapor variability has been assessed using radiosonde data (e.g., Dai et al.

2011), satellite data (e.g., Soden et al. 2005), and precipitable water (PW) data obtained from the Global Navigation Satellite System (GNSS) atmospheric delay measurements (e.g., Wang et al. 2013). Figure 1.3 shows the time series of total column water vapor from the Special Sensor Microwave/Imager (SSM/I), after the merging of records from successive satellites. The linear trend based on monthly SSM/I data over the global oceans was 1.2 % per decade (0.40 +/- 0.09 mm per decade) for the period from 1988 to 2004. The trends are positive over most of the regions, but also suggestive of an El Niño-Southern Oscillation (ENSO) influence. Most of the patterns associated with the interannual variability and linear trends can be reproduced from the observed SST changes over this period by assuming a constant relative humidity (Trenberth et al. 2005). The column water vapor is primarily weighted by the lower troposphere, and the variability of vertical distribution of water vapor cannot be assessed, although water vapor in the upper air is important for the radiative process.

Routine radiosonde observations have been made globally since the 1940s and these data provide the longest record of upper air temperature, humidity, geopotential height, pressure, and horizontal winds. However, the original radiosonde record contains various errors and biases because of changes in instrumentation and observational practices, which cause non-climate-related changes or inhomogeneities (e.g., Seidel et al. 2009). Such inhomogeneities in the record have severely hampered the application of radiosonde humidity data in climate studies.

The radiosonde humidity data need to be homogenized to estimate long-term trends. The homogenization often involves first detecting stepwise change points in

time series statistically and then adjusting the time series to remove the discontinuities. For the case of radiosonde temperature records, many homogenization methods have been developed to remove non-climatic changes without using metadata that describe the change points in instrumentation and bias information for each radiosonde type, because these metadata are often incomplete or not available. Meanwhile, for the radiosonde humidity records, there have been very few attempts to homogenize these data (e.g., Dai et al. 2011). Statistical homogenization methods can resolve many of the discontinuities in the historical radiosonde record. However, they may also remove some of the real climate signals (Sherwood 2007). If possible, homogenization should be performed with the metadata and bias information for each sensor type, rather than statistically.

For operational upper-air observation from radiosondes, metadata (including a list of locations and instruments with dates) is incomplete and sometimes incorrect. But, metadata of the Japan Metrological Agency (JMA) stations are described relatively well (e.g., Sakota et al. 1999; Shibue et al. 2000; Kobayashi et al. 2012). To investigate the humidity trend over Japan using radiosonde data with metadata, the author evaluates the measurement uncertainty of the Meisei RS-06G (RS2-91) radiosonde, which is used at the JMA stations since the 1990s. (Chapter 2)

Relative humidity controls the cloud formation and cloud lifetime. The information of the relative humidity inside clouds is important for mesoscale and climate modeling. The water vapor pressure in clouds is commonly assumed to be saturated with respect to liquid water in liquid clouds, and with respect to ice in ice clouds. The water vapor in mixed-phase clouds, which are often observed at high latitudes

in cold seasons, is often approximated as a weighted average of the respective saturation values over liquid and ice. The weighting factor in models is usually specified as a function of temperature or cloud liquid/ice content (e.g., Jakob 2002). Such a treatment for the mixed-phase clouds is an oversimplified one, but the detailed microphysical processes involved in mixed-phase clouds are not completely understood due to the lack of the observation. The "in-situ" measurement of water vapor in clouds is a great challenge (Korolev and Mazin 2003). "In-situ" instruments are plagued by the contamination errors caused by supercooled cloud droplets. The temperature measurement also has large uncertainty near cloud-top due to wet-bulb effect (e.g., Immler et al. 2010). To improve the understanding of cloud microphysics, the accurate "in-situ" measurement of water vapor and temperature is crucial. In this study, however, the author will mainly focus on the water vapor measurement in conditions of clear sky or upper-level (ice) clouds. Although improving the water vapor measurement in clouds is one of the important problems, the detailed discussion of the measurement in low-level clouds is beyond the scope of this study.

1.3 Upper tropospheric and lower stratospheric water vapor measurements

The long-term record of the stratospheric water vapor at a mid-latitude site indicates the decadal positive trend of ~1.0%/year (Fig. 1.4). Small changes in the stratospheric water vapor can have a large impact on the Earth's radiation budget. It was pointed out that stratospheric water vapor is an important driver of decadal global climate changes (Solomon et al, 2010). Although the methane oxidation is one of the sources of stratospheric water vapor, and methane has been increasing over

the industrial period, the trend of the stratospheric water vapor is too large to attribute to methane oxidation alone (Oltmans et al. 2000). It has been assumed that the temperature near the Tropical Tropopause Layer (TTL) region controls the stratospheric water vapor through the dehydration processes in the TTL (SPARC 2000; Fujiwara et al. 2010).

Because the operational radiosonde observations are designed to obtain the lower tropospheric water vapor for weather forecasting, the RH sensors on operational radiosondes have very poor response at low temperatures in the UT/LS. Currently, some special research-quality instruments such as the chilled-mirror hygrometers, Lyman-α hygrometers and various satellite and ground-based remote sensing instruments are the main source of information on UT/LS water vapor. There are, however, often large differences among the measured concentrations by different instruments. The large measurement uncertainty limits our understanding of water vapor changes and processes in the UT/LS. Figure 1.5 shows an example of large discrepancies of different water vapor instruments, that is, a comparison of water vapor mixing ratios from the balloon-borne Cryogenic Frostpoint Hygrometer (CFH) and Harvard Lyman-α hygrometer (HWV) on the WB57 aircraft, and the Microwave Limb Sounder (MLS) onboard the NASA Aura satellite near San Jose, Costa Rica on 1 February 2006. It shows large differences between the CFH and HWV up to 50 -100 % or 1-2 ppmv at the UT/LS, while a relatively good agreement between AURA/MLS and CFH can be found. The disagreement among these instruments at low mixing ratios continues to limit our understanding of the physical processes controlling dehydration in the TTL (Fueglistaler et al. 2013). Recent studies (e.g., Rollins et al. 2014) showed that difference between instruments has reduced in

comparison with some previous campaigns, but non-negligible biases (0.38 - 0.89 ppmv or ~10% - 20%) still remain between balloon-borne frostpoint hygrometers (CFH) and some hygrometers on the WB57 aircraft. The cause of these systematic uncertainties remains unresolved, and there is no physical explanation for why these instruments would have a systematic bias. These measurement uncertainties will continue to limit our understanding of the dehydration in the TTL.

Relative humidity controls the cloud formation. Cirrus clouds play an important role in the complex mechanisms of the climate change (Solomon et al 2007). As a major uncertainty in climate modeling, cirrus cloud's radiative forcing are influenced not only by macroscopic properties (i.e., coverage, thickness and height), but also by microphysical properties (i.e., ice crystal number density and size distribution). Cirrus microphysical processes depend on atmospheric conditions such as RHi and aerosol components (Peter et al. 2006; Murray et al. 2010; Cziczo et al. 2013). To understand the microphysical processes of cirrus clouds, it is required to measure RHi (i.e., air temperature and water vapor pressure) accurately inside and outside cirrus clouds. For example, to distinguish between hexagonal and cubic phases (Murphy and Koop 2005; Murray et al. 2005), RHi measurement accuracy on the order of 10% is necessary. RHi measurements in the UT often indicate significantly higher values than what can be explained given the current understanding of ice nucleation, both inside and outside of clouds (Peter et al. 2006). Hygrometers on aircraft observed sustained RHi of ~130% in dense cirrus where the equilibrium between ice and vapor phase should be rapidly achieved, and RHi near 100% is expected (Jensen and Pfister 2005). Also, RHi exceeding 160%, the homogeneous nucleation threshold (Koop et al. 2000), was observed in the TTL

(e.g., Jensen et al 2005). Current measurement uncertainties of water vapor in UT/LS limit our understanding of cirrus ice nucleation. To understand the microphysical processes of cirrus cloud, we need to measure air temperature and water vapor inside and outside of cirrus cloud accurately.

1.4 Water vapor observation requirement

Accurate measurement is also essential to detect long-term changes. Table 1.1 shows the climate observation requirements proposed by the Global Climate Observing System (GCOS) Reference Upper-Air Network (GRUAN). The primary goals of the GRUAN are to provide the vertical profiles of reference measurements suitable for reliably detecting climate change on decadal time scales. For trend detection, the appropriate frequency of measurement is also needed. Whiteman et al. (2011) found that due to the high natural variability in atmospheric water vapor, the amount of time to detect trends in upper troposphere is relatively insensitive to instrumental random uncertainty and that it is much more important to increase the frequency of measurement than to decrease the random error in the measurement. However, the systematic uncertainty is considered to influence the trend detection seriously, especially in the stratosphere. The trend detection in the LS will be much more sensitive to instrumental systematic uncertainty than in the UT, because anticipated trends in the LS is expected to be smaller than in the UT (WMO 2013). A high-accuracy and high-frequency water vapor measurement in the LS is required to detect the trends.

There are many methods for measuring atmospheric water vapor. Satellite observations provide global distribution of water vapor, and thus represent an

important source of information over the oceans, where radiosonde observations are scarce. Microwave radiation is less affected by cloud and thus is a useful method of humidity measurement from the space. The MLS can observe atmospheric water vapor above ~350 hPa. Since the 1990s, the estimation of atmospheric water vapor (PW) from the GNSS atmospheric delay is available and is being continuously evaluated. The PW measurement from the GNSS atmospheric delay has important advantages as an absolute measurement because it does not need an independent calibration and is not being affected by clouds. However, this method estimates only the column integrated water vapor amount in the atmosphere, and thus cannot estimate upper-air water vapor. Raman lidars are a technique for retrieving high-resolution water vapor mixing ratio profiles. The measurement accuracy is limited by calibration uncertainties (systematic errors) and by photon-counting noise (random errors which increase rapidly with altitude). Raman lidar calibration can be performed by comparisons with other collocated sensors, such as high-quality radiosondes (Whiteman et al. 2006). For the calibration and validation of these remote sensing techniques, high accuracy “in-situ” instruments are required.

The chilled-mirror hygrometry is a high-accuracy sensor based on the thermodynamic principle in wide temperature ranges. In this study, the author develops a new instrument, a Peltier-based chilled-mirror hygrometer, with a goal of the high-accuracy water vapor measurement from surface to LS for the climate monitoring. (Chapter 3).

Table 1.1. the climate observation requirement (GRUAN 2009)

Variable	Temperature	Water Vapour	Pressure
Priority (1-4)	1	1	1
Measurement Range	170 – 350 K	0.1 – 90000 ppmv	1 –1100 hPa
Vertical Range	0 – 50 km	0 to ~30 km	0 – 50 km
Vertical Resolution	0.1 km (0 to ~30 km)	0.05 km (0 – 5 km)	0.1 hPa
Precision	0.2 K	2% (troposphere) ** 5% (stratosphere)	0.01 hPa
Accuracy	0.1 K (troposphere) 0.2 K (stratosphere)	2% (troposphere) ** 2% (stratosphere)	0.1 hPa
Long-Term Stability	0.05 K *	1% (0.3%/decade) **	0.1 hPa

*The signal of change over the satellite era is in the order of 0.1–0.2K/ decade, therefore long-term stability needs to be an order of magnitude smaller to avoid ambiguity

**Precision, accuracy and stability are relative with respect to mixing ratio

1.5 Structure of the thesis

The purposes of the present study are to assess the uncertainty of water vapor measurements from operational upper-air observation, and to improve the accuracy of the atmospheric water vapor measurements for climate monitoring. In particular, the author conducts the following researches:

1) The evaluation of the measurement uncertainty of an operational radiosonde RH sensor, and the development of a new correction scheme on the Meisei radiosondes;

2) the investigation of impacts of the new correction on historical operational radiosonde water vapor data; and

3) the development of a high-accuracy environmentally-friendly chilled-mirror

hygrometer for climate monitoring.

In Chapter 2, the measurement uncertainty of an operational RH sensor on Meisei radiosondes is evaluated, and a new correction for some Meisei radiosonde types is proposed. Furthermore, the author investigates the impact of a new correction on historical Meisei radiosonde humidity data taken in Japan. In Chapter 3, a newly developed chilled-mirror hygrometer for meteorological balloons to measure tropospheric and stratospheric water vapor is presented. Instrument descriptions and results of chamber experiments and test flights are described. Finally, a summary of this study is provided in Chapter 4 .

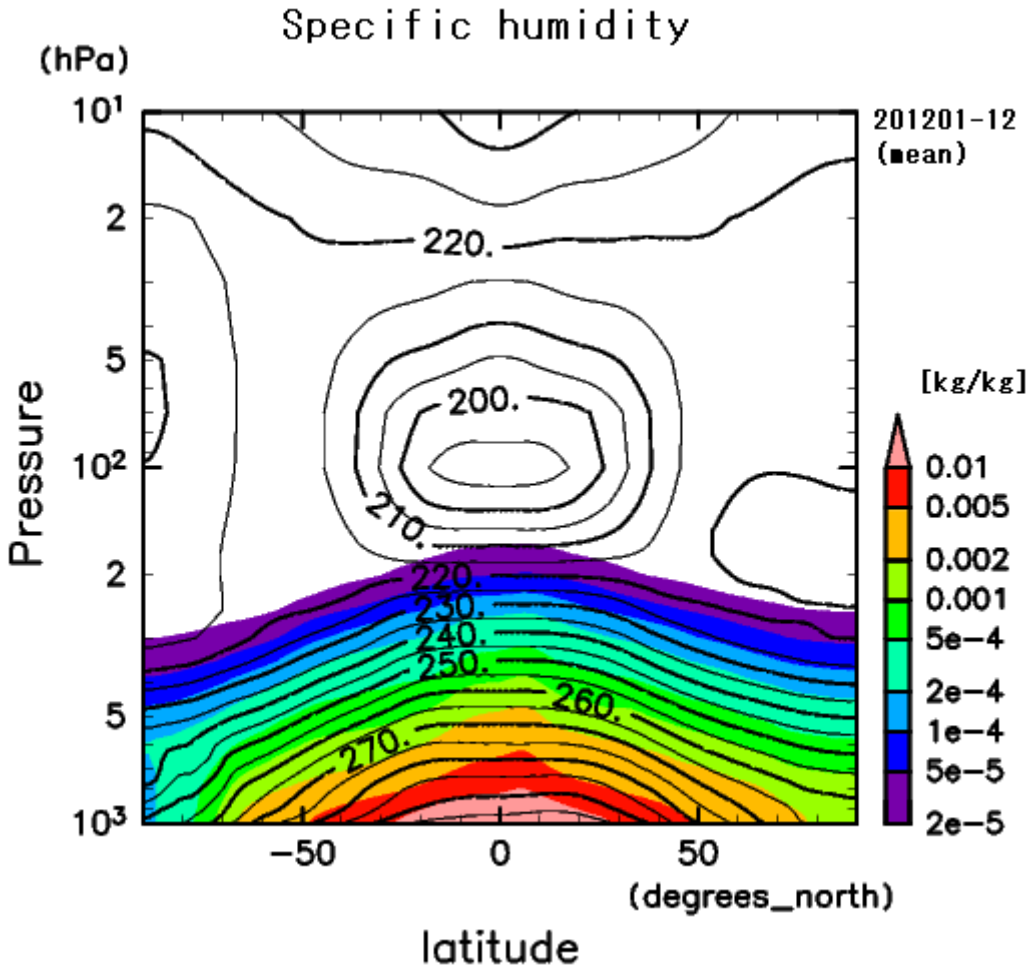

Fig.1.1 Height-latitude cross-sections of the annual mean temperature (contours) and specific humidity in the troposphere (color shades) in 2012 as obtained from a reanalysis dataset (ERA-interim, Dee et al., 2011).

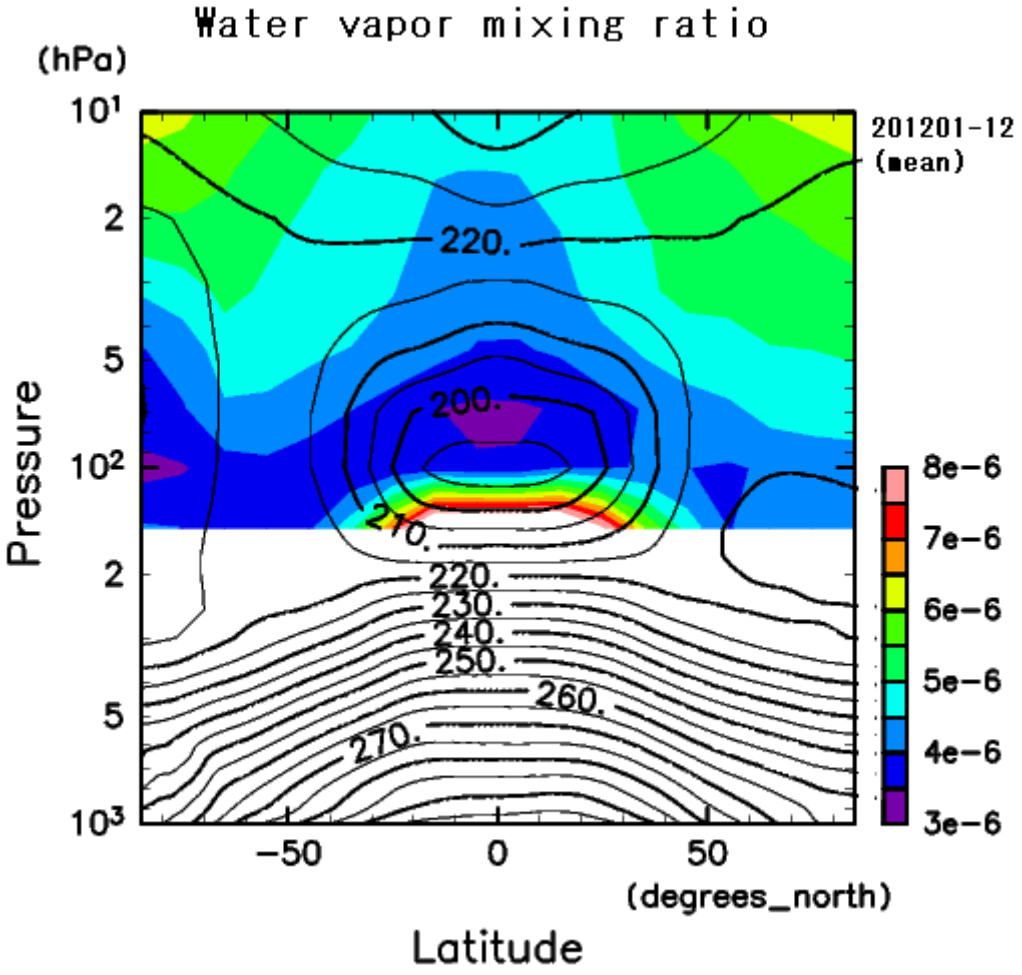

Fig.1.2 Height-latitude cross-sections of the annual mean temperature (contours) and water vapor mixing ratios at 10-147 hPa (color shades) in 2012 as obtained from a reanalysis dataset (ERA-interim) and a satellite data (GozMmlpH2O, the H2O dataset merged with the HALOE (Halogen Occultation Experiment), the ACE-FTS (Atmospheric Chemistry Experiment - Fourier Transform Spectrometer) and the Aura MLS), respectively.

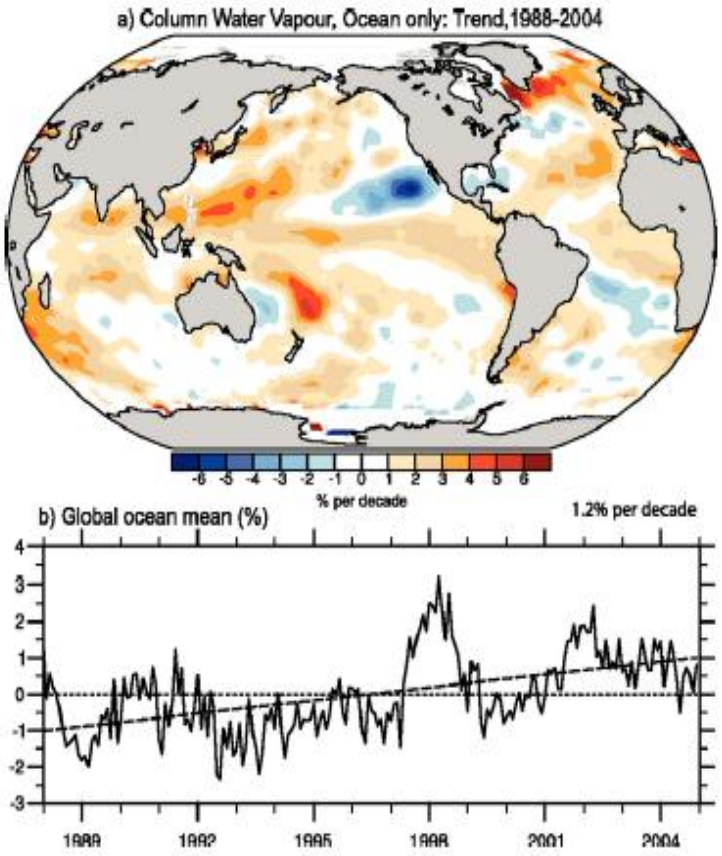

Fig 1.3 Linear trends in precipitable water (total column water vapor) in % per decade(top) and monthly time series of the anomalies over the global ocean (bottom) from SSM/I (Trenberth et al., 2005)

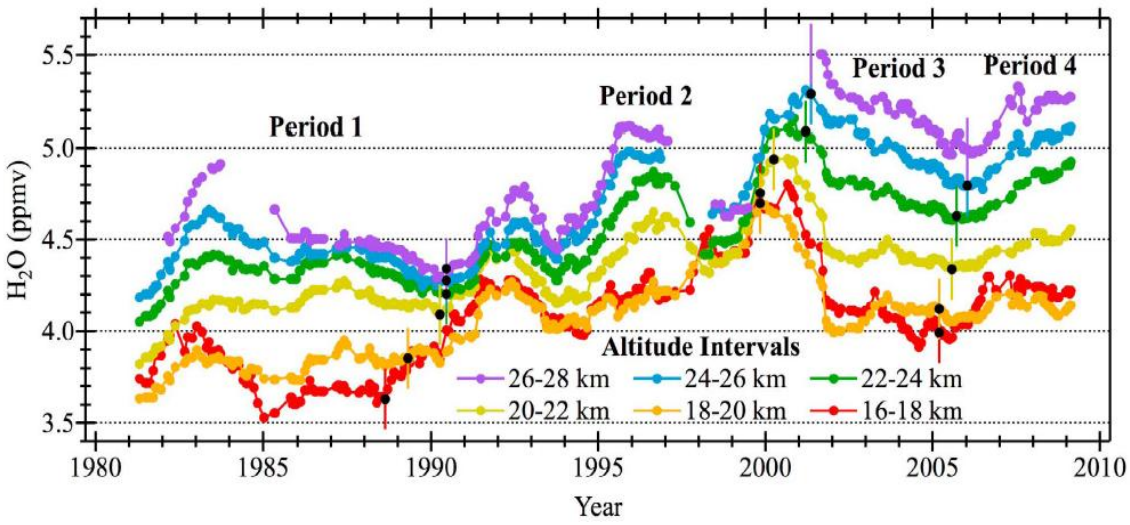

Fig. 1.4 Moving averages of the 2 km water vapor mixing ratio averages in each of the six altitude layers at Boulder, USA measured with the National Oceanic and Atmospheric Administration (NOAA) Frost Point Hygrometer (FPH). The averaging window had a width of ±1 year and a threshold of 12 data points to compute an average. (Hurst et al, 2011)

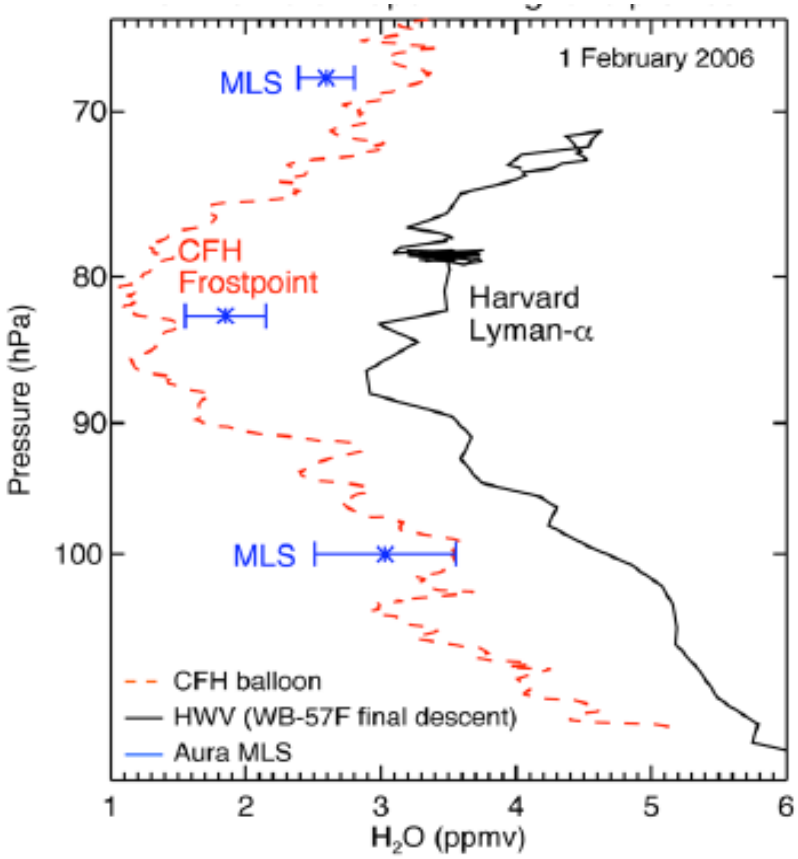

Fig. 1.5 Comparison of water vapor mixing ratios from balloon-borne CFH (red) and airborne HWV (black), and the AURA/MLS (blue) near San Jose, Costa Rica (10°N, 84°W) on 1 February 2006. (Fahey et al. 2009)

Chapter 2
Measurement uncertainty of operational upper-air observations

In this chapter, we focus on the measurements of the tropospheric water vapor of operational upper-air observations. Section 2.1 points out the problem of operational radiosonde observations at the Japan Meteorological Agency (JMA) to detect its long-term variability. Section 2.2 describes the results from chamber experiments to evaluate the measurement uncertainty of the RH sensor on the Meisei RS-06G, RS-01G, and RS2-91 radiosondes, and the development of a new temperature-dependence (T-D) correction. Section 2.3 discusses the impact of the new T-D correction on historical Meisei radiosonde humidity data.

2.1 Radiosonde history and artificial changes at the JMA stations.

Routine radiosonde observations have been made globally since the 1940s and these data provide the longest record of upper air conditions (Elliott 1995). In Japan, the operational radio sounding first started in 1938 at Tateno station (WMO station No. 47646, 36°03'N, 140°08'E, surface level 26 m; Sakota et al. 1999). The humidity sensor of the JMA /Meisei RSⅡ-56 and the earlier models were a hair hygrometer (e.g., CMO-S38, S-48, RSⅡ-56). The RSⅡ-80 (1981~) has a carbon hygristor. The Meisei RS2-91 (1992~) has a thin-film capacitive sensor. The RH sensor material for RS2-91 was changed in 1999, and then a temperature-dependence (T-D) correction, hereafter referred to as the original T-D correction, was introduced in 2003 to

compensate the wet bias of this sensor below the freezing point. Although the performances of the radiosonde instruments are expected to improve at each model change in general, such changes in instrumentation and observational practices often inevitably cause non-climate-related changes or inhomogeneity in the time series (e.g., Elliott 1995).

Radiosonde instrument information, reported in the 31313 section of data submitted to the World Metrological Organization (WMO) by JMA stations since 1995, is not included in the Integrated Global Radiosonde Archive (IGRA; http://www.ncdc.noaa.gov/oa/climate/igra/). IGRA is known as the largest and most comprehensive dataset of quality-assured radiosonde observations from National Climatic Data Center, which consists of radiosonde and pilot balloon observations at over 1500 stations (Durre et al. 2006). However, reported instrument codes only indicate the basic model identifier such as Meisei RS2-91 (code 47) or RS-01G (code 55), so that the information from original soundings is still insufficient for climate studies. For example, the exact dates when the RS2-91 RH sensor changed to a new sensor type and when the T-D correction was introduced at the JMA stations are not given. Therefore, we need to obtain this information directly from the JMA station (Sapporo District Meteorological Observatory for the Sapporo station and the JMA Aerological Observatory for the Tateno station). According to the information thus obtained, the RS2-91 radiosonde was introduced on 7 February 1993 at Sapporo and on 1 October 1992 at Tateno, and the new RH sensor was introduced for RS2-91 on 24 June 1999 at Sapporo and on 13 July 1999 at Tateno. The original T-D correction was introduced on 1 February 2003 at both stations.

Meisei RS2-91 was replaced by Vaisala RS92 radiosonde on 1 December 2009 at

both stations. Vaisala RS92 RH sensor has been found to have a substantial daytime dry bias due to solar heating of the RH sensor, which is not protected by a reflective cap due to its design. The dry bias increases significantly with height and has a clear diurnal variation with its maximum at local noon (Vömel et al. 2007b; Yoneyama et al. 2008). The bias and some other errors are considered to be corrected by DigiCORA version 3.64 (Wang et al. 2013). This software version was not installed at Sapporo and Tateno stations and the version 3.63 was used through the period of RS92 (Kobayashi et al. 2012). Vaisala RS92 was further replaced recently with Meisei RS-11G at Sapporo starting on 1 September 2013 and at Tateno starting on 2 July 2013. Analysis of Vaisala RS92 and Meisei RS-11G is beyond the scope of this paper.

Figure 2.1 shows the time series of temperature and RH at 500 hPa at Sapporo and Tateno, using the original data obtained from the IGRA. We can see that the instrumental change points correspond to the discontinuities in the RH time series. Fujiyoshi (2010) pointed out that the frequency of appearance of upper-level clouds estimated from radiosonde humidity data shows sudden changes when radiosonde instrumental changes occurred. Such inhomogeneity in the record has severely hampered the application of radiosonde humidity data in climate studies. In the next section, we investigate the measurement uncertainty of the RS2-91 by the chamber experiment.

2.2 Correction of the stepwise change at 0 °C in Meisei RS2-91, RS-01G, and RS06G radiosonde relative humidity

2.2.1 Introduction

The Meisei RS-06G radiosonde is a successor to the Meisei RS-01G (introduced in 2002) and the Meisei RS2-91 (introduced in 1991) rawinsonde, and has been used operationally in Japan, Indonesia, Sri Lanka, and Taiwan. All of these models are currently in use, with the same RH sensor installed since July 1999 (Ishihara 2004), although the models have had changes in the sensor cap (Shimizu et al. 2008). For brevity, references in this paper to the RS-06G RH sensor also apply to the same sensor on the RS-01G and RS2-91 (only after the middle of 1999) models. During development of the balloon-borne chilled mirror hygrometer (Chapter 3), on the other hand, we used the RS-06G radiosonde and found that the RS-06G RH profiles always showed a stepwise change of ~ 3% RH at 0 °C. Figure 2.2 shows an example of simultaneous soundings from the RS-06G and the Cryogenic Frostpoint Hygrometer (CFH) (Vömel et al. 2007a), and the RS-06G RH profile shows a stepwise drying (wetting) of ~ 3% RH at 3850 m, 4000 m, and 4600 m; i.e., at 0 °C air temperature, when the temperature is decreasing (increasing) through 0 °C. A similar stepwise change of this magnitude is commonly found in RS-06G RH data from other soundings.

This stepwise change is related to the correction of the RS-06G RH measurements by the processing software to compensate for the temperature dependence of the RH sensor. The RS2-91 (and subsequently RS-01G and RS-06G) RH sensor is a thin-film capacitive sensor, in which a thin hydrophilic polymer layer on a glass substrate acts as the dielectric of a capacitor (Sakota et al. 1999). The capacitance changes in response to the number of water molecules permeating from the ambient air into the polymer. The relationship between the capacitance and the RH of the ambient air is determined by factory calibration procedures. As the individual

thin-film capacitive RH sensors differ slightly, every RS2-91 (and subsequently RS-01G and RS-06G) RH sensor is calibrated in the factory at RH levels of 15%, 30%, 50%, 70%, 90%, and 95% RH at a constant air temperature of +25 °C to obtain a set of instrument-specific calibration coefficients (Sakota et al. 1999). According to Ishihara (2004), RS2-91 started using a new RH sensor in July 1999 and the same sensor was used later in RS-01G and RS-06G. After a moist bias was discovered, especially below freezing, the following temperature dependence correction has been applied, starting about February 2003, to all RH measurements at air temperatures between -40 ˚C and 0 ˚C obtained using these models:

$$\Delta RH = K_0 + K_1 T + K_2 T^2$$

$$RH_{\mathrm{corr}} = RH_0 - \Delta RH$$

$$(-40\,^{\circ}\mathrm{C} \leqq T \leqq 0\,^{\circ}\mathrm{C}) \qquad (2.1)$$

where ΔRH (%) is the correction amount, T (°C) is the air temperature uncorrected for solar heating, RH_0 (%) is the uncorrected RH, RH_{corr} (%) is the corrected RH, and K_{i} is a constant ($K_0 = 2.86$, $K_1 = -1.68 \times 10^{-1}$, $K_2 = -2.02 \times 10^{-3}$). While the Japan Meteorological Agency (JMA) only officially reports radiosonde RH measurements above –40 °C, in RS-06G RH measurements for research applications the correction in Eq. (2.1) is further extrapolated to below –40 °C (Meisei 2012, personal communication). The largest correction factor is 6.4% RH at –40 °C, and the smallest is 2.86% RH at 0 °C. Therefore, the correction has a finite value of 2.86% RH at 0 °C, causing an artificial stepwise change of ~ 3% RH at 0 °C as shown in Fig. 2.2. Although the manufacturer claims that the accuracy of the RS-06G is 7% RH, this correction for the temperature dependence produces an

unrealistic stepwise change at a key atmospheric level, the 0 °C level, and this requires revision.

The atmospheric 0 °C level (~ 3 km in mid-latitudes, and ~ 5 km in the tropics) is the melting layer, where falling ice particles or snowflakes become liquid water (Houze 1993). This melting layer is important for precipitation processes and cloud dynamics. In radar meteorology, the melting layer is known as the bright band, and produces intense radar echoes. Although atmospheric characteristics can change significantly at the 0 °C level, the stepwise change of ~ 3% RH obtained using the RS-06G RH sensors is not realistic, but is artificially generated as explained above. In this study, the author investigates the temperature and RH dependence of the RS-06G RH sensor in a chamber, with the aim of developing a more appropriate correction curve that is continuous at 0 °C.

In general, thin-film capacitive RH sensors may be subject to several other sources of error, depending on the manufacturer and model of radiosonde, including a slow sensor response at low temperatures, contamination errors caused by supercooled cloud droplets, bias errors related to non-water molecules being absorbed into the hydrophilic polymer layer, and dry bias errors due to differences between the RH sensor temperature and the ambient air temperature caused by a thermal lag of the RH sensor during radiosonde ascent and by solar heating during daytime flights (e.g., Miloshevich et al. 2001; Wang et al. 2002; Vömel et al. 2007b; Yoneyama et al. 2008). Among these errors, the thermal lag of the RH sensor is caused by the finite time required for RH sensors to reach equilibrium with the changing ambient air temperature during a flight (e.g., Morrissey and Brousaides 1970; Williams and Acheson 1976; WMO 2008). In this study, the author also

investigates the thermal lag of the RS-06G RH sensor using a laboratory based thermostatic chamber test.

We can understand the bias errors and sensor characteristics for each radiosonde type by conducting radiosonde intercomparisons for simultaneous flights (e.g., WMO 2011; Kobayashi et al. 2012; Sakota et al. 1999) and laboratory experiments using thermostatic chambers (e.g., Sugidachi and Fujiwara 2013). RH sensor on radiosonde has various bias errors such as manufacturer calibration error, solar radiation heating during daytime observations, contamination by cloud droplets, slow sensor response at low temperatures, and so on. Comparisons using flight tests can assess the net bias errors among different radiosondes during flights, but it is difficult to quantify each of the potential bias errors. Laboratory experiments cannot completely replicate the actual flight conditions such as solar radiation and ventilation around the RH sensor, but they are useful in quantifying radiosonde sensor characteristics such as the temperature dependence, response time, and individual differences.

The remainder of Section 2.2 is organized as follows. Section 2.2.2 describes two experiments, and their results, which test the temperature dependence and thermal lag of the Meisei RS-06G RH sensor, Section 2.2.3 proposes a new correction for RS-06G RH measurements based on results from these two experiments, and provides an example of the application of the new correction, and Section 2.2.4 provides the application period of the new correction.

2.2.2 Experiments

2.2.2.1 Estimation of temperature dependence between –50 and +40 °C

We estimate the temperature dependence of ten RS-06G RH sensors by comparing them with reference instruments under various chamber conditions, at air temperatures from –50 to +40 °C, and at RH levels from 20% to 80% (The Ishihara (2004) correction was derived using tests in a similar chamber). We built a special experimental setup for this experiment. Figure 2.3 shows the overall configuration of this experiment. Five RS-06G RH sensors and the reference sensors were placed in a polyvinyl chloride (PVC) pipe with an inner diameter of 65 mm, which was then placed in the thermostatic chamber (Espec PSL-4KH). This chamber can control temperature within -70 to +150 °C, and humidity within 20 - 98% RH above ~ +10 °C. The internal volume of the chamber is 800 l. The Electronic Temperature Instruments (ETI) RF-100 platinum resistance thermometer was used as a reference temperature sensor, and the Azbil Corporation FDW10 chilled-mirror hygrometer (Ibata and Kanai 2008) as a reference dew point sensor (see Table 2.1 for the manufacturer's specifications for these instruments). Airflow of about 2 m s^{-1} was produced within the pipe using a fan located at its entrance to ensure uniformity in the measurement air. Although the sensor in flights is usually exposed to stronger airflow (~6 m s^{-1}) than this condition, we cannot replicate the flight condition of the radiosonde due to the experimental constraints. Two sets of five RS-06G RH measurements were made. As stated in note (1) in Table 2.1, the first set of five radiosondes represented four manufacturing batches, and the second set of radiosondes was from the same batch. Figure 2.4 (bottom) shows the temperature and RH conditions for all measurements in this experiment. RH values are with respect to liquid water and no experiments were performed with RH values supersaturated with respect to ice. For each set, the

RH and temperature in the chamber were changed every 30 to 60 minutes under surface pressure conditions (~1000 hPa) to ensure the steady measurement condition. This made it possible to ignore errors derived from the slow sensor response and the thermal lag of the RH sensor. Readings were taken five times every 10 to 20 s for each set of conditions.

We analyze the data which are not corrected using Eq. (2.1) (hereinafter referred to as "RS-06G RH_0"). We calculate the reference RH values from the reference temperature and reference dew point readings using Buck's equations (Buck 1981; Appendix A), which is also used for the RS-06G calibration by the manufacturer (WMO 2011; Meisei 2012, personal communication). In the upper air observation, RH is usually evaluated with respect to liquid water even at air temperatures below 0°C (WMO 2008). Accordingly, if the condensate on the mirror of the FDW10 is liquid water,

$$RH = 100\,\frac{e_w(T_m)}{e_w(T_a)} \tag{2.2}$$

where e_w is the saturation vapor pressure of moist air with respect to water, T_m is the mirror temperature, and T_a is air temperature. If the condensate on the mirror of the FDW10 is ice,

$$RH = 100\,\frac{e_i(T_m)}{e_w(T_a)} \tag{2.3}$$

where e_i is the saturation vapor pressure of moist air with respect to ice.

The measurement uncertainties associated with these experiments are expressed according to the Guide to the expression of Uncertainty in Measurement (GUM)

(JCGM/WG1 2008). Conceivable measurement uncertainties in the reference RH are derived from the instrument performance, errors in reading, and spatial and temporal non-uniformity in the PVC pipe. The combined standard uncertainties are calculated from these sources of uncertainty. The error bars in Fig. 2.4 represent the 95% level of confidence (the coverage factor k = 2). The expanded uncertainties of the reference RH level range within 0.7% - 3.2% RH. Meanwhile, the five readings of RS-06G RH_0 values are closely comparable, with typical standard deviation ~0.1% RH, an order of magnitude smaller than the measurement uncertainty of the reference RH. The error bars for the RS-06G RH_0 values are omitted in Fig. 2.4. Calculation of the measurement uncertainties is described in detail in Appendix B.

Figure 2.4 shows the difference between values of RS-06G RH_0 and the reference RH at each temperature and RH condition for all measurements. RS-06G RH_0 is wetter than the original manufacturer's correction factor (dashed line in Fig. 2.4) by 7% RH or more for some conditions below +10 °C. Figure 2.5 shows the difference between RS-06G RH_0 and the reference RH with respect to RH, and shows that RS-06G RH_0 has an RH dependence in addition to the temperature dependence. These biases can be approximated by a linear regression between 20% and 80% RH. The wet bias is greater in wetter conditions when air temperatures are below +20 °C. The wet bias approaches 10% RH at high RH and low temperature conditions. In contrast, a small dry bias is found at +40 °C. From these results, the RS-06G RH_0 levels show a tendency towards a dry bias above about +25 °C, and a wet bias below about +25 °C. It should be noted again that the temperature of +25 °C is the calibration condition used by the manufacturer. These results, the large bias of over 7% RH and the RH dependence, are surprising, and will be further

explored in the next section.

2.2.2.2. Estimation of thermal lag for the RS-06G RH sensor

Figure 2.4 showed that our measured values of RS-06G RH_0 were significantly different from the original manufacturer's correction curve, exceeding 7% RH under some conditions. However, such a large bias was not reported in in-flight intercomparisons with other models of radiosonde (e.g., WMO 2011). We speculate that this discrepancy arises due to the differences in the measurement conditions; i.e., in a chamber or in flights. Here, we focus on the difference in air temperature conditions; air temperatures in our chamber experiments were stable by experimental design, while air temperatures in flights can change dramatically over a short period. If the thermal lag of the RH sensor is not negligible, the RH sensor temperature will not immediately correspond to the temperature of the ambient air. During an ascending flight through the troposphere, the RH sensor temperature would usually be warmer than the ambient air temperature. The warmer RH sensor would result in RH measurements that are biased dry. Therefore, there is a possibility that the RS-06G RH measurements always have a dry bias component in the troposphere. It should be noted that the RS-06G RH sensor is mounted in a sensor hood to minimize solar heating effects and contamination by supercooled cloud droplets and rain.

To estimate the dry bias component caused by the thermal lag of the RS-06G RH sensor, we investigate the response time of the RH sensor temperature to a stepwise air temperature change in a chamber. A thermistor, which is used as an air temperature sensor of the RS-06G, was used to measure the RH sensor temperature.

The thermistor has a negligible heat capacity with the response time of 1.3 s at 1000 hPa even without airflow (Shimizu et al. 2008). Furthermore, the use of the same type of thermistors for the RH sensor and air temperatures minimizes error in the thermal lag evaluation. The thermistor was attached to the surface of the RH sensor using aluminum tape whose heat capacity is also sufficiently small. We measured the response time in the chamber as the air temperature was changed from 0 °C to +10 °C over a short period of around 100 s. This experiment was conducted under the following three conditions:

(1) without the sensor hood;

(2) with the sensor hood, and in an airflow perpendicular to the sensor arm; and

(3) with the sensor hood, and in an airflow parallel to the sensor arm.

Airflow was ~ 3 m s^{-1} for all conditions. The sensor in flights is usually exposed to stronger airflow than these conditions because the ascent rate of the radiosonde is usually set as ~ 6 m s^{-1}. However, we cannot replicate the flight condition of the radiosonde due to the experimental constraints. Specifically, the maximum wind speed by the fan we used is ~3 m s^{-1} at ~1000 hPa. Also, it is impossible for us to control the airflow under reduced pressure conditions. For these reasons, we conducted this experiment only under surface pressure, and estimate the thermal lag in ascent flight using these experimental results and some assumptions.

Figure 2.6 shows the response time of the RH sensor temperature, T_s, and the applied measurement condition, T_a. On the basis of Newton's Law of Cooling, the relationship between T_s and T_a can be written as

$$\tau \frac{dT_s(t)}{dt} + T_s(t) = T_a \tag{2.4}$$

where τ is the time constant. By replacing $dT_s(t)/dt$ with $(T_s(t) - T_s(t - \delta t))/\delta t$, where δt is a finite time step, $T_s(t)$ is solved as

$$T_s(t) = \frac{T_a\,\delta t + \tau\,T_s(t - \delta t)}{\tau + \delta t} \tag{2.5}$$

Figure 2.6 also shows an estimated RH sensor temperature, T_{s_est}, profile derived from Eq. (2.5) with a constant τ for each experiment; i.e., 10 s in Fig. 2.6 (1), 25 s in Fig. 2.6 (2), and 50 s in Fig. 2.6 (3). We see that the assumed value of τ explains the evolution of T_s reasonably well.

We also estimate the thermal lag of the RH sensor during actual flights. The thermal lag should depend on the heat transfer between the ambient air and the surface of the RH sensor. As air density decreases with height, the temperature difference between the ambient air and the RH sensor is expected to increase at higher altitudes. Williams and Acheson (1976) give the time constant, τ, theoretically as

$$\tau = \frac{mc}{hA} \tag{2.6}$$

where m is the mass of the sensor, c is the specific heat, h is the convective heat-transfer coefficient, and A is the total surface area of the sensor. Morrissey and Brousaides (1970) proposed that, assuming the RH sensor is a flat plate with a zero angle of attack to airflow, h can be calculated from:

$$\mathrm{h} = \frac{1}{L}\int_0^L 0.332k\,Pr^{\frac{1}{3}}\left(\frac{\rho v'}{\mu x}\right)^{\frac{1}{2}} dx \tag{2.7}$$

where L is the width of the RH sensor, k is the thermal conductivity of air, Pr is the Prandtl number, ρ is the density of air, v' is the flow rate on the RH sensor, and μ is the viscosity coefficient. The values of Pr, k, and μ depend on air temperature. For the RS-06G RH sensor, v' is not equal to the ascent rate v because of the sensor hood and the irregular payload movement in the flight. Here, we assume that v' is proportional to v, that is,

$$v' = Cv \tag{2.8}$$

where C is a constant that indicates the effect on how the ventilation changes by the sensor hood and the airflow direction. Substituting Eqs. (2.7) and (2.8) into Eq. (2.6), τ can be rewritten as

$$\tau = C'k^{-1}Pr^{-\frac{1}{3}}\left(\frac{\mu}{\rho v}\right)^{\frac{1}{2}} \tag{2.9}$$

where C' is a constant depending on the RH sensor property and the value of C. To estimate τ during actual flights, we calculate the value of C' by using the time constant obtained from the chamber experiment (Fig. 2.6). It is considered that the sensor hood may cause poorer ventilation, while the pendulum motion of the payload during ascent flights may cause better ventilation. We assume the condition without the sensor hood [i.e., Fig.2.6(1)] as the best ventilated condition, because nothing blocks the airflow. On the other hand, we assume the condition with the sensor hood and in an airflow parallel to the sensor arm [i.e., Fig.2.6(3)] as the worst ventilated condition, because the sensor hood substantially obstructs the airflow. Given these assumptions, it is considered that the actual flight condition lies between the conditions in Fig. 2.6(1) and 2.6(3), i.e., we use the results from Fig.

2.6(1) and 2.6(3) as the upper and lower limits, respectively. The values of C' become 102 $\mathrm{kg\,m^{\frac{1}{2}}\,s^{-2}\,K^{-1}}$ for Fig. 2.6(1), and 512 $\mathrm{kg\,m^{\frac{1}{2}}\,s^{-2}\,K^{-1}}$ for Fig. 2.6(3). Assuming that the possible value of C' at the flight condition lies equally likely between these values (i.e., a rectangular distribution), the expected value of C' is the midpoint of the interval, 307 $\mathrm{kg\,m^{\frac{1}{2}}\,s^{-2}\,K^{-1}}$. Then, the standard uncertainty, $u_{C'}$ is

$$u_{C'} = \frac{512 - 102}{2\sqrt{3}} = 118\ \mathrm{kg\,m^{\frac{1}{2}}\,s^{-2}\,K^{-1}} \tag{2.10}$$

Also, we estimate τ during actual flights with the ascent rate of $6.0 \pm 1.0\ \mathrm{m\,s^{-1}}$. While the ascent rate of the radiosonde is usually set at ~ 6 m $\mathrm{s^{-1}}$, the value may vary according to the meteorological condition by ~1.0 m $\mathrm{s^{-1}}$ even in the troposphere. The standard uncertainty from the ascent rate fluctuation, u_v, is

$$u_v = \frac{1}{\sqrt{3}} = 0.58\ \mathrm{m\,s^{-1}} \tag{2.11}$$

Using this C' values, the ascent rate of $6.0 \pm 1.0\ \mathrm{m\,s^{-1}}$ and the atmospheric profile from the U.S. standard atmosphere (NOAA, NASA, and USAF 1976), we calculate τ and the temperature difference between the RH sensor and the ambient air, ΔT, in the upper air (considering only the lag error of temperature response of the sensor substrate, not other errors mentioned above such as solar heating in daytime).

Finally, we estimate the uncertainty of τ using the law of propagation of uncertainty. The combined standard uncertainty of τ, u_τ, is written as

$$u_\tau = \sqrt{\left(\frac{\partial \tau}{\partial C_l}\right)^2 u_{C_l}{}^2 + \left(\frac{\partial \tau}{\partial v}\right)^2 u_v{}^2}$$

(2.12)

To determine the expanded uncertainty, we use $k = 2$ as coverage factor. Thus, the expanded uncertainty of RH, U_τ, becomes

$$U_\tau = k\, u_\tau = 2\, u_\tau$$

(2.13)

Figure 2.7 shows the air temperature and density profiles from the U.S. standard atmosphere, and the calculated values of τ and ΔT. The light and dark gray lines show the expanded uncertainties estimated by Eq. (2.13). This figure suggests that ΔT is larger at higher altitudes; e.g., 0.9 ± 0.7 °C at 5 km and 1.3 ± 1.0 °C at 10 km. The RH sensor which is too warm due to the thermal lag indicates drier RH than the actual RH because the saturation vapor on the surface of the RH sensor is not $e(T_a)$ but $e(T_a + \Delta T)$, i.e.,

$$RH_{flight} = 100\, \frac{e}{e_w(T_a + \Delta T)}$$

(2.14)

where RH_{flight}, is the RH obtained from the RS-06G in flight, and e is the vapor pressure of measurement air. On the other hand, the RH in a chamber, $RH_{chamber}$, is calculated by Eq.(2.2) or (2.3). Accordingly, the relationship between $RH_{chamber}$, and RH_{flight} is

$$RH_{chamber} = RH_{flight} \times \frac{e(T_a + \Delta T)}{e(T_a)}$$

(2.15).

When $\Delta T > 0$, RH_{flight} has drier than $RH_{chamber}$. Because the RS-06G RH

sensor become $\Delta T > 0$ in tropospheric ascents as shown in Fig. 2.7, it is considered that the thermal lag could cause dry bias for the RS-06G RH measurements.

2.2.3. A new correction for RS-06G RH measurements

The results of these two experiments show that the RS-06G RH_0 value has a wet bias component caused by the temperature and RH dependence of the sensor material, and a dry bias component related to the thermal lag of the RH sensor, which is warmer than the ambient air temperature during a tropospheric balloon ascent. It is expected that the two biases are, at least in part, cancelled out during a flight, and the measurement accuracy of 7% RH (k = 2) proposed by the manufacturer is achieved. To fully characterize the sensor's behavior in flight, and to obtain a complete correction algorithm, we need to take account of all other measurement errors, in addition to the two biases outlined above. Major errors include the slow response of the RH sensor at low temperatures (Miloshevich et al. 2004), and the solar heating dry bias (Vömel et al. 2007b; Yoneyama et al. 2008). Consequently, we propose here a simple correction to remove the artificial stepwise RH change at 0 °C resulting from the use of Eq. (2.1). We assume that the two biases discussed in Section 2.2.2 are the major sources of error. As a test, we add the dry bias component to the wet bias component shown in Fig. 2.3. Using the relationship of Eq. (2.15), the correction factor during tropospheric ascents then becomes

$$\begin{aligned} \Delta RH &= RH_{flight} - RH_{ref} \\ &= RH_0 \times \frac{e(T_a)}{e_w(T_a + \Delta T(T_a))} - RH_{ref} \end{aligned} \tag{2.16}$$

Although $\Delta T(T_a)$ depends on the actual vertical gradients of air temperature and air density, and the ascent rate of the radiosonde, we use the results in Fig. 2.7 for simplicity. Figure 2.8 shows the $\Delta T(T_a)$ and corresponding linear fits. Figure 2.9 shows the RH difference between the reference RH and the corrected value by applying the correction for the thermal lag expressed by Eq. (2.16). Figure 2.9 also shows the original manufacturer's correction curve extrapolated up to +14.5 °C. The upper limit of +14.5 °C is chosen because the original manufacturer's correction curve intersects $\Delta RH = 0$ at +14.5 °C. The marks in the figure indicate the value derived from ΔT_τ in Fig.2.8, and the light gray vertical bars indicate the uncertainties derived from $\Delta T_\tau \pm U_\tau$ in Fig.2.8. We see that the corrected experimental results and the extrapolated correction curve show better agreement above 0 °C, as well as below 0 °C. Consequently, we propose to extrapolate the original manufacturer's correction up to +14.5 °C to resolve the artificial stepwise change at 0 °C. Extrapolating the correction above +14.5 °C to adjust for the dry bias at higher temperatures (Fig. 2.9) is not recommended because biases with no correction, even at 40 °C, are within specifications.

In addition, we observed that the RS-06G RH_0 value has an RH dependence as shown in Fig. 2.5. Equation (2.16) is effective at reducing the bias associated with the RH dependence below +20 °C. Figure 2.10 shows the difference between the RS-06G RH_0 corrected by Eq. (2.16) and the reference RH with respect to RH, and the corresponding linear fit. The RH dependence corrected by Eq. (2.16) (i.e., Fig. 2.10) is smaller than in the uncorrected result (i.e., Fig. 2.5), except at +40 °C.

Figure 2.11 shows the estimated bias in the RS-06G RH measurements during a tropospheric balloon ascent, that is, the result of subtracting the proposed

correction amount from the results in Fig. 2.9. The error bars in Fig. 2.11 show the uncertainty (k = 2), including the uncertainty from the dry bias estimation, that from the reference RH in our chamber experiment, and that from the individual differences of the RS-06G RH sensor. Each component of the uncertainty (k = 2) is estimated as 0.3% to 3.8% RH for the dry bias estimation, 0.7% to 3.3% RH for the reference RH, and 0.3% to 0.9% RH for the individual differences among the 10 sensors (twice the standard error). We find that the differences among the individual RS-06G RH sensors are very small. Figure 2.11 indicates that there remains a wet bias (< 5% RH) at –40 to +10 °C, but these biases are within 7% RH, which is the manufacturer's specification. For daytime flights, solar heating is expected to cause an additional dry bias component. The RH profiles from the RS-06G in the WMO radiosonde intercomparison campaign at Yangjiang in 2010 showed day–night differences (Figure 8.2.5, lower left, of WMO, 2011). The nighttime intercomparison results in WMO (2011) showed that the RS-06G RH measurements are ~ 5% RH higher than the CFH measurements in the middle troposphere; this is quantitatively consistent with our experiment results in Fig. 2.11. Meanwhile, the daytime intercomparison results in WMO (2011) showed that the RS-06G and CFH RH measurements agree within ~ 3% RH in the middle troposphere; this can be interpreted that during the daytime, an additional dry bias by the solar radiation heating accidentally cancels out the wet bias at –40 to +10 °C shown in Fig. 2.11.

Figure 2.12 shows the RH profile from Fig. 2.2 corrected using our new simple approach, and it shows that the stepwise change in RH has been eliminated.

2.2.4. Application of the new correction

The new correction should be applied to the RH measurements using the RS2-91 (only after the middle of 1999), RS-01G, and RS-06G radiosondes at least until the development of a more accurate correction. Operational soundings made with RS2-91, RS-01G, and RS-06G radiosondes are identified in text format soundings by instrument codes 47, 55,and 30 respectively in the 31313 section (Code Table 3685 in WMO, 1995). For users of either current or archived soundings, perform the following steps:

1. From the 31313 section of the original sounding (usually reported in part TTBB, or possibly several sounding parts), if the instrument and sounding system code is 74702, 55504, 55508, 75508, or 73008, continue to step 2. Besides most Japanese stations, this includes 12 stations in Indonesia, 1 station in Sri Lanka, and 2 stations in Taiwan reporting one or more of the above codes starting between 2004 and 2010 (Aerological Observatory 2012, personal communication; Meisei 2012, personal communication). If the 31313 section is completely omitted or is any other value, it is unlikely that the RS-06G humidity sensor is used.
2. If the code is 74702 (RS2-91), the old humidity sensor is used before July 1999 at JMA stations and before about the beginning of 2000 at stations 47580 and 47681 (Japanese Self-Defense Forces stations) and 89532 (Syowa, Antarctica) (Schroeder 2008). If the new sensor is used, continue to step 3. None of the corrections in this paper apply to the old humidity sensor.
3. At any station except 47991 before approximately February 2003 (station 47991 before August 2003), the new sensor is used with no correction. Apply the manufacturer correction (2.1) at all temperatures up to +14.5 °C.

4. After the date in step 3, the correction is applied up at temperatures up to 0 °C, so apply (1) at all temperature levels from +0.1 to +14.5 °C to eliminate the RH discontinuity.

2.3 Impact of the proposed correction on historical humidity data at the JMA stations

In this section, the author applies the new T-D correction to operational radiosonde data, and investigates the impact of the original and new T-D corrections on the long-term radiosonde humidity record at two JMA stations: Sapporo (WMO station 47412, 43°04'N, 141°20'E; surface level 26 m until 30 November 2009, 18 m starting 1 December 2009) and Tateno (WMO station 47646, 36°03'N, 140°08'E, surface level 31 m before 30 November 2009, 26 m after 1 December 2009). Elevation changes at these stations on 1 December 2009 were not launch site relocations, but the definition of the radiosonde surface data level (which determines the reported surface pressure) was changed from the station barometer elevation (inside the meteorological office) to the actual launch elevation (1 meter above the surface by the balloon inflation building).

2.3.1 Data and method

The IGRA provides daily radiosonde data at more than 1500 stations for the period from 1938 to the present. The archive contains information extracted from each transmitted sounding and is expressed in common units, including limited metadata (WMO station ID, year, month, day, UTC hour, and launch time), and each reported standard and significant level (pressure, geopotential height,

temperature, dew point depression [DPD, temperature minus dew point], wind direction, and wind speed [m s^{-1}]). As specified by WMO code formats, each station converts the original radiosonde RH values to DPD.

The JMA uses the following equation to convert RH values to DPD values (JMA 1995):

$$DPD = \frac{(T + 243.5)^2 ln\,(\frac{RH}{100})}{(T + 243.5)\,ln\left(\frac{RH}{100}\right) - 4303.4} \tag{2.17}$$

where T is air temperature [°C]. In this study, we recover the RH value from T and DPD using Eq. (2.17). We also convert RH to specific humidity (SH) to understand the variability of water vapor alone by using the following equation (Bolton 1980):

$$e = 6.112 \exp(\frac{17.67\ T_d}{T_d + 243.5})$$

$$s = \frac{\varepsilon e}{P - (1 - \varepsilon)e} \tag{2.18}$$

where e is water vapor pressure [hPa], T_d is dew point temperature [°C], s is SH [kg kg^{-1}], P is air pressure [hPa], and ε = 0.622 is the ratio of the molecular weight of water vapor and dry air.

We saw that the instrumental change points correspond to the discontinuities in the RH time series in Fig. 2.1. In this study, the author focuses on the period with the new RH sensor; that is, from 24 June 1999 to 30 November 2009 at Sapporo and from 13 July 1999 to 30 November 2009 at Tateno. the author applies the new T-D correction proposed in Section 2.2 to the original data over these periods, and evaluate its impact on the humidity record. Figure 2.1 also shows the difference

between the daytime (9:00 JST, or 0:00 UTC) and nighttime (21:00 JST, or 12:00 UTC) measurements. This difference is probably due to the dry bias from solar radiation heating (e.g., WMO 2011), in addition to the real atmospheric diurnal variability. The relative daytime dryness is about the same in the entire Meisei RS2-91 period as in the Vaisala RS92 period at both stations, suggesting that daytime heating of the RH sensor is similar with Meisei RS2-91 (under a rain-protective cap) and Vaisala RS92 (with no cap). The Meisei RS2-80 carbon RH sensor in a duct was only slightly drier in daytime, but it registered neither very dry nor very moist conditions. Since the Meisei RS2-91 correction formula does not account for possible solar heating, the following discussion considers only nighttime data to avoid complications.

2.3.2 Results and discussion

Figure 2.13 shows the deseasonalized time series and their linear fits for RH at 925, 700, and 500 hPa at Sapporo and Tateno. Lines in color are daily anomalies from daily means based on the Meisei RS2-91 period at each station, smoothed by averaging anomalies for 31 days centered on each day, with the annual mean RH added to each smoothed anomaly value. In the top panels, the input RH values and corresponding means are based on the original data obtained from IGRA, where the T-D correction (Eq. 2.1) is applied only below 0 °C and only starting February 2003. In the bottom panels, anomalies are computed and smoothed in the same way, but the input data for means and anomalies is corrected by applying the T-D correction where it was not applied originally, below +14.5 °C through January 2003 and between 0 and +14.5 °C starting February 2003. The corrected linear fits show

smaller downward trend values than the original linear fits. The new T-D correction is found to result in much smaller downward trend values at 500 hPa at Sapporo and almost no trend at Tateno. In this paper, the likelihood of RH (SH) trends is based on the results of statistical significance testing (T-testing) performed at confidence levels of 95% (JMA 2012). For the effective degrees of freedom, the number of data is divided by the effective decorrelation time (i.e. 31 for the averaged data for 31 days). It should be noted that the uncertainty estimation of these linear fit values does not consider the measurement uncertainty.

Figure 2.14 shows the original and corrected SH time series. The corrected SH values are derived from dew point values calculated from the RH values with the new T-D correction shown in the bottom panel of Fig. 2.13. We can see that the original SH linear fits show spurious large downward trends, especially at 500 and 700 hPa, at both stations. The corrected SH linear fits show no significant trends at Sapporo and Tateno.

Previous observational studies (e.g., Soden et al. 2005; Trenberth et al. 2005) show that tropospheric water vapor is globally increasing under the assumption of near-constant RH, although there is strong interannual variability. The corrected results at Tateno are consistent with the near-constant RH hypothesis, but the results at Sapporo are not, and show downward RH trends at 500 in the 2000s. This is probably in part because the period in this study is too short to detect RH trends with the warming climate. To extend our analysis over longer periods, we need to investigate the biases between the RS2-91 and the older radiosonde models such as the Meisei RS2-80 and RS2-91 with the old RH sensor, which had been used in the 1980s and the 1990s at JMA stations. In addition, the RS2-91 RH corrected by the

new T-D correction still contains a small bias error depending on temperature and RH, which is up to about +5 ± 4% RH (the confidence interval represents the expanded uncertainty with the coverage factor k = 2) around –10°C. Because such a bias error has a large impact on the uncertainty estimation of RH linear trends, further efforts are needed to reduce the measurement uncertainty by making more simultaneous flights and detailed laboratory experiments. Where possible, we will make laboratory experiments and in-flight comparisons with reference instruments such as chilled-mirror hygrometers to quantify the errors in radiosondes used in the past.

Also, instrument transitions of operational radiosondes may affect the reanalysis data quality. Figure 2.15 shows the time-series of anomalies of specific humidity in July for each year at Sapporo (42.75˚N, 141˚E). Note that only July data are used for simplicity. The ERA-interim assimilates radiosonde humidity observations except at high altitude (typically P < 300 hPa) and extreme cold conditions (typically T < 233 K), while a homogenized dataset (RAOBCORE_T_1.3 by Haimberger et al.(2008)) is used for the radiosonde temperature assimilation (Dee et al. 2011). We can see that sudden change in specific humidity correspond to the change points of radiosondes in some case. Further investigation is needed to evaluate how measurement biases of radiosondes affect the quality of the reanalysis dataset.

2.3.3 Conclusions

The original and new T-D corrections on the RH measurements from the Meisei RS2-91, RS-01G and RS-06G radiosondes not only correct the bias error of individual soundings, but also influence the analysis of long-term humidity

variability in the upper air. For these radiosonde RH measurements, the new T-D correction proposed in Section 2.2 should be applied to the historical RH record. However, information on the exact dates of updating of the sensor in the RS2-91 and the introduction of the original T-D correction was not available publicly (e.g., in the IGRA). Thus, we obtained the information directly from the Sapporo and Tateno stations to investigate the impact of the T-D corrections. We hope that in the near future, complete metadata will be made available by the operational agencies, as these metadata are critical for climate studies.

The corrected linear fits show smaller downward trend values than the original linear fits. These results show that the humidity variability in the 2000s at stations using the Meisei RS2-91, RS-01G, and RS-06G radiosondes strongly depends on whether or not the new T-D correction is applied. However, this correction does not consider the solar radiation heating during daytime observations, contamination by cloud droplets, or slow sensor response at low temperatures. Also, the humidity values corrected by the new T-D correction may still include small wet biases during nighttime observations. To further reduce uncertainties in humidity trends, we need more laboratory experiments and in-flight comparisons with reference instruments.

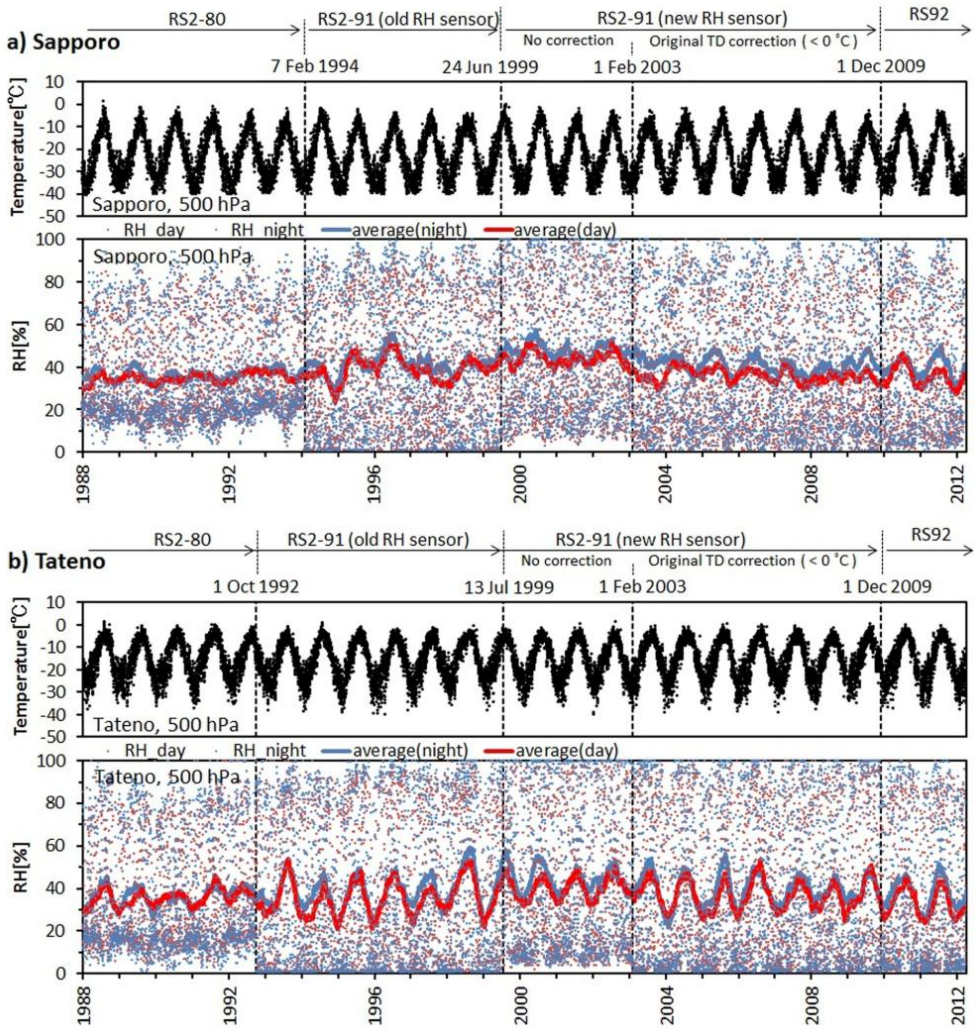

Fig. 2.1. Time series of temperature (top panels, black) and relative humidity (RH) (bottom panels, red and blue) at 500 hPa at Sapporo (a) and Tateno (b), using the original IGRA data. Dots represent the 12-hourly daily RH data and solid lines represent 4-month running averages, to improve the presentation, for the daytime (red) and nighttime (blue) measurements.

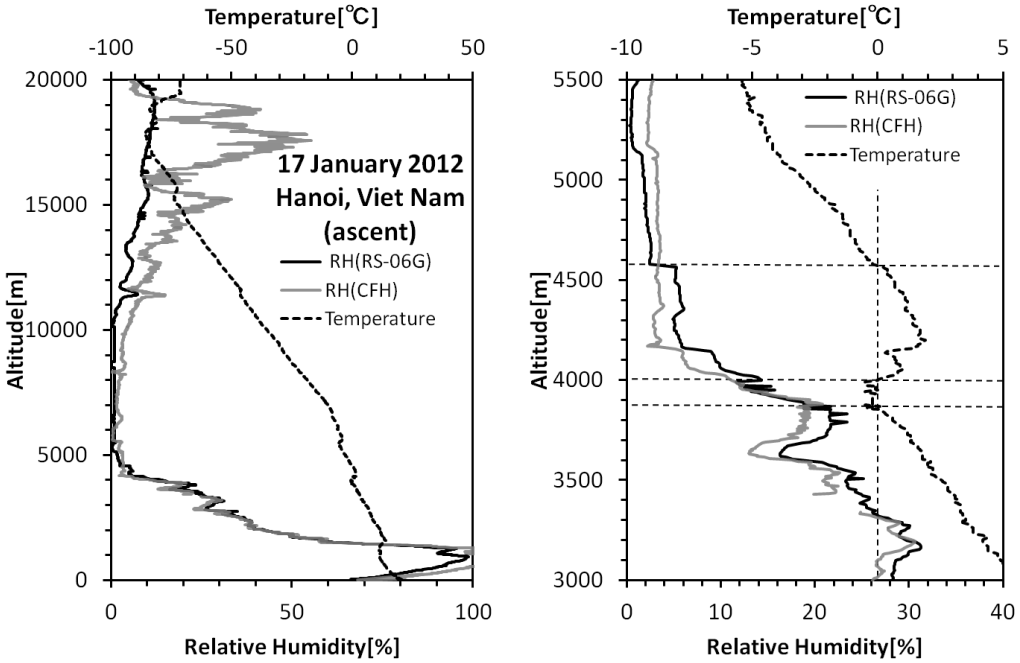

Fig. 2.2. Simultaneous daytime RH profiles from the Meisei RS-06G radiosonde (black) and the CFH (gray) at Hanoi, Viet Nam (21.01°N, 105.80°E). Dashed curves show air temperature measured with the RS-06G. Left panel shows profiles for the whole troposphere, while the right panel shows the region around 0 °C.

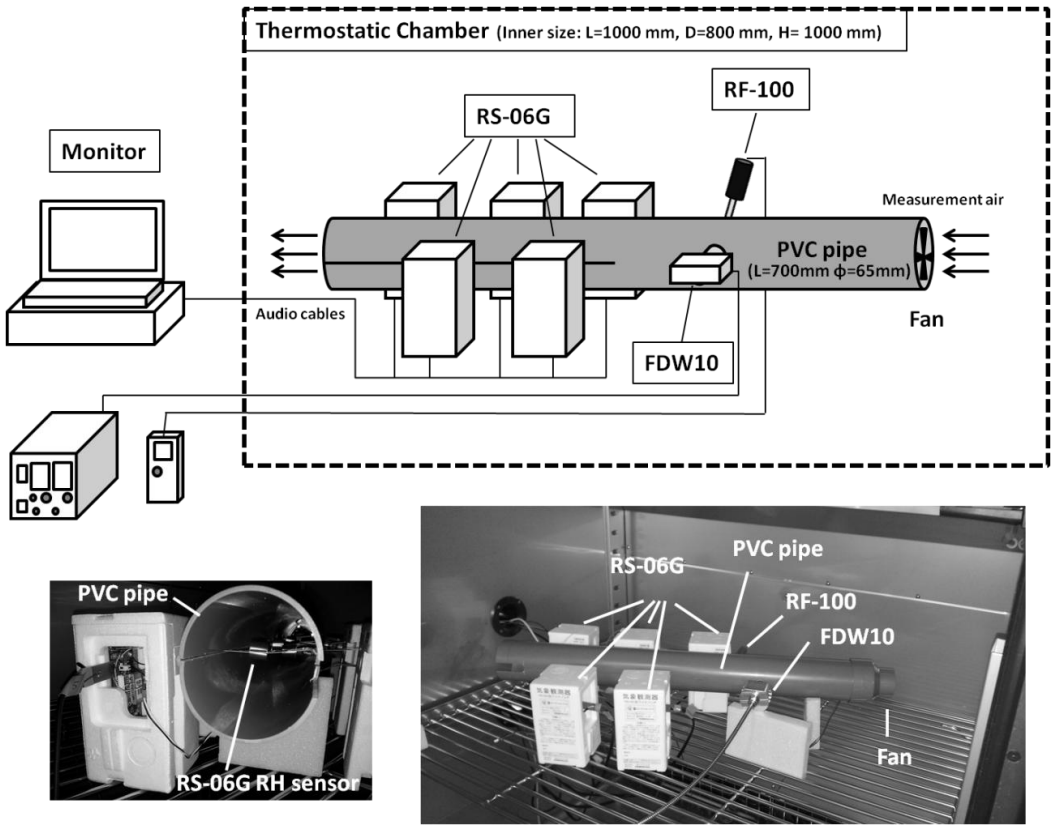

Fig. 2.3. Experimental setup in the thermostatic chamber. The bottom left picture shows the sensor probe of the RS-06G in the PVC pipe. The bottom right picture shows the five RS-06G radiosondes and the two reference instruments set in the PVC pipe.

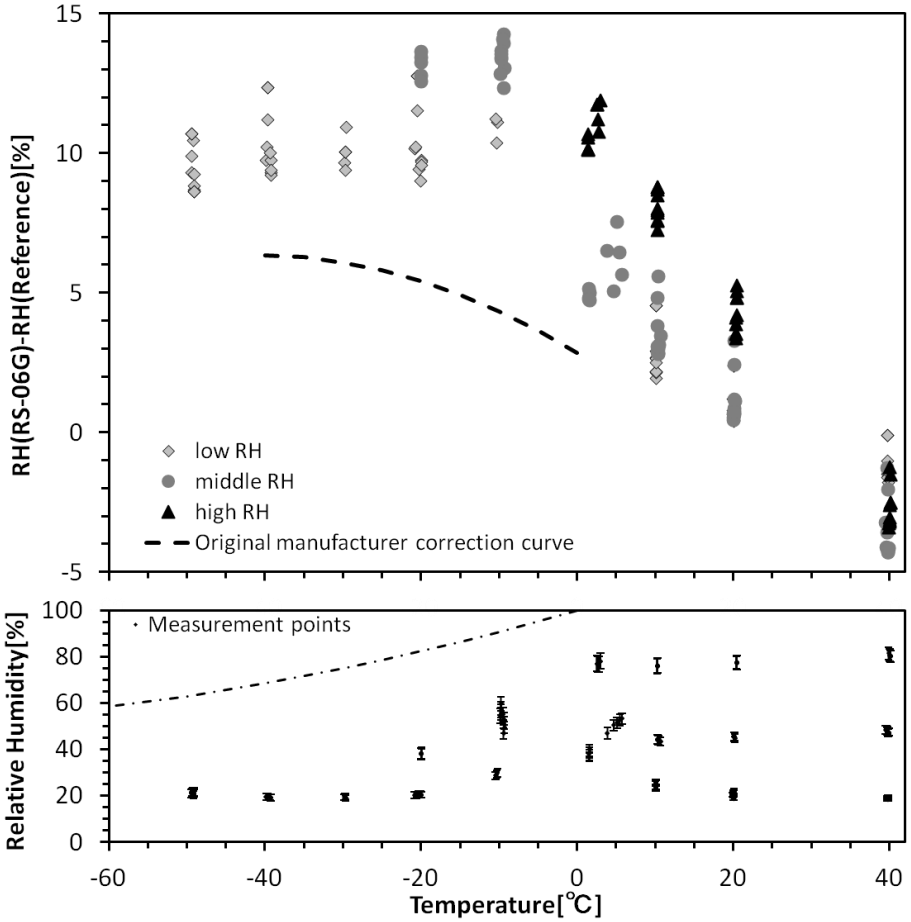

Fig. 2.4 (top) Temperature dependence of RS-06G RH measurements under different RH conditions. The RH difference between the reference and the uncorrected RS-06G RH_0 is indicated by gray squares (for < 30% RH), dark gray circles (for 30% to 70%RH), and black triangles (for > 70% RH). The dashed curve represents the original manufacturer's correction curve. (bottom). The experimental conditions (dots) and the uncertainties (vertical bars). The dot-dashed curve in the bottom panel indicates the ice saturation.

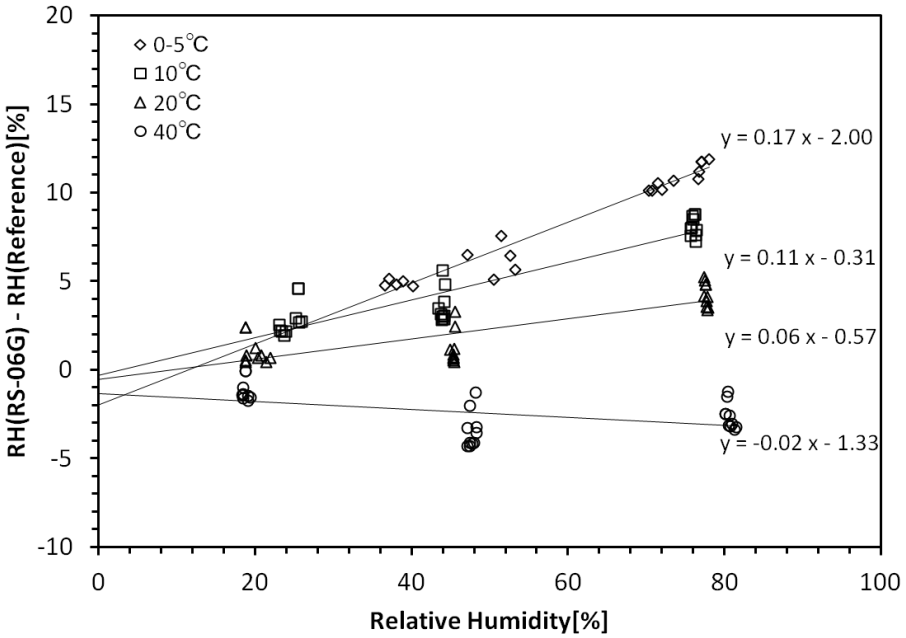

Fig. 2.5 RH dependence of the RS-06G RH measurements under different temperature conditions. The RH difference between the reference and the uncorrected RS-06G RH_0 is indicated by the rhomboids (for 0 to +5° C), squares (for +10 °C), triangles (for +20 °C), and circles (for +40 °C). The lines are linear fits for each temperature group.

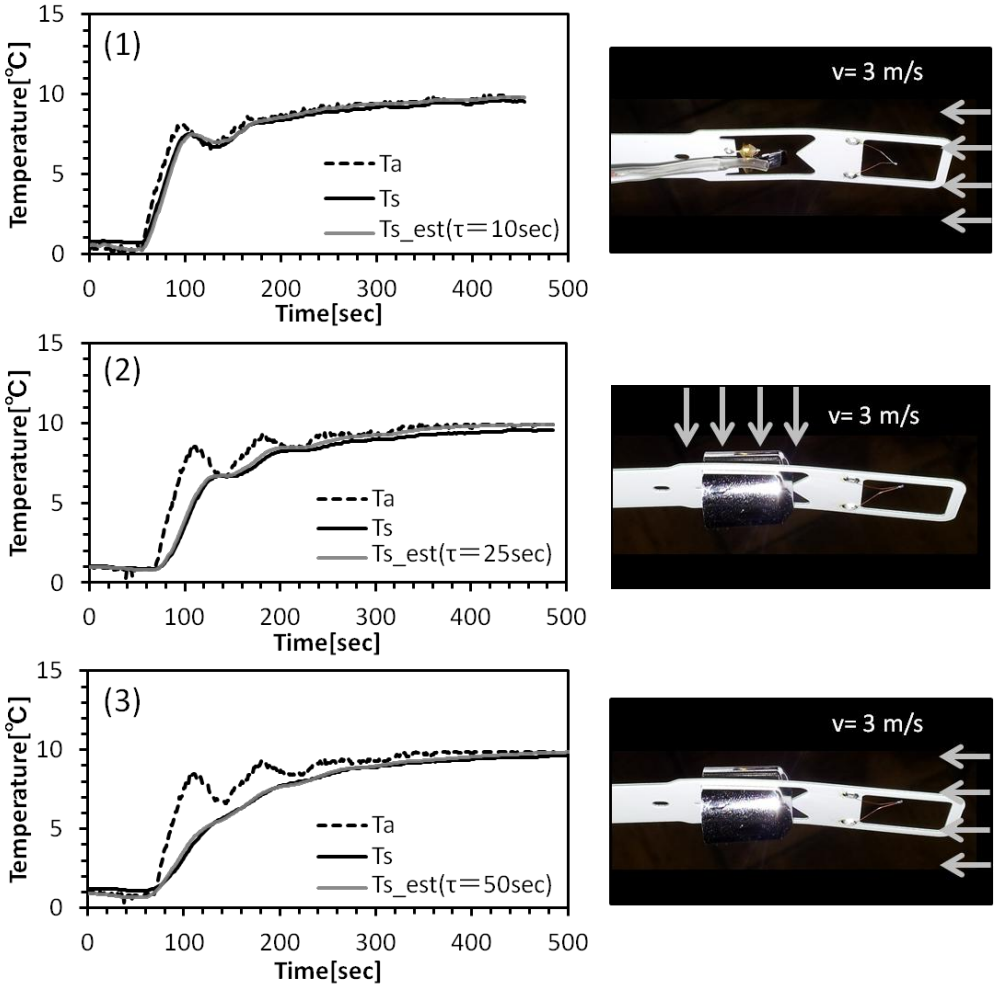

Fig. 2.6. Temperature profiles of the RS-06G RH sensor in response to a stepwise change in air temperature in a chamber (left), and photo showing the three different measurement conditions (right). Dashed lines show applied air temperature, black lines show the change in the sensor's surface temperature, and gray lines show estimated sensor temperatures; i.e., air temperature data filtered with Eq. (5) using the indicated value of τ.

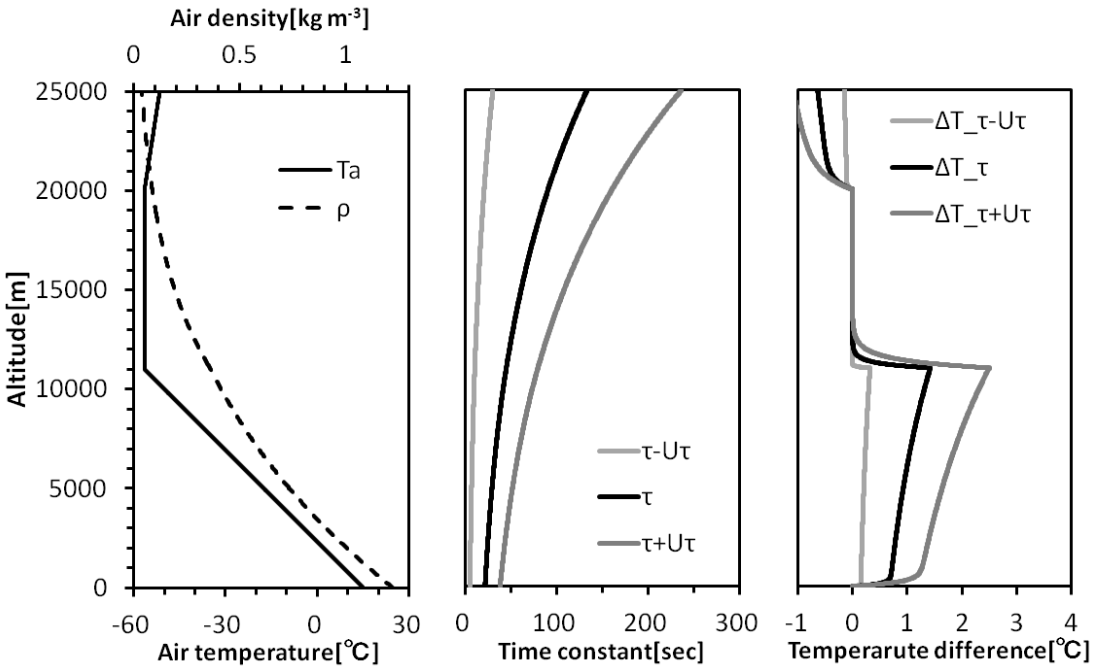

Fig. 2.7.(left) Temperature and density profiles from the U.S. standard atmosphere. (center) The time constant calculated by Eq. (2.9).The black line indicate the value derived from $C' = 307\ \mathrm{kg\,m^{\frac{1}{2}}\,s^{-2}\,K^{-1}}$. The light and dark lines indicate the expanded uncertainties, i.e., $\tau - \mathrm{U}_\tau$ and $\tau + \mathrm{U}_\tau$ The difference between the RH sensor temperature and ambient air temperature for the three conditions.

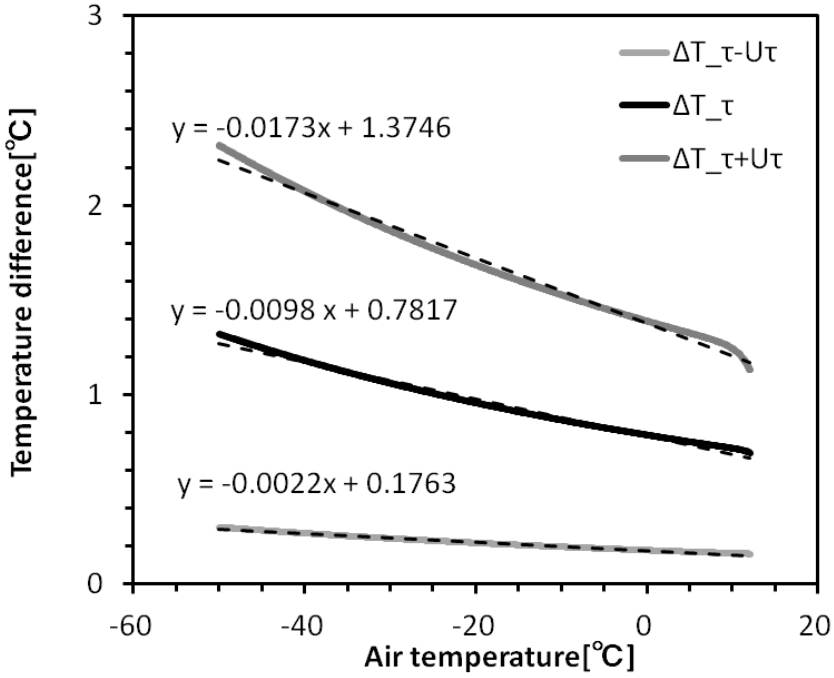

Fig. 2.8. Temperature difference shown in the right panel of Fig. 2.7 against the ambient air temperature shown in the left panel of Fig. 2.7. Dotted lines show the linear fit.

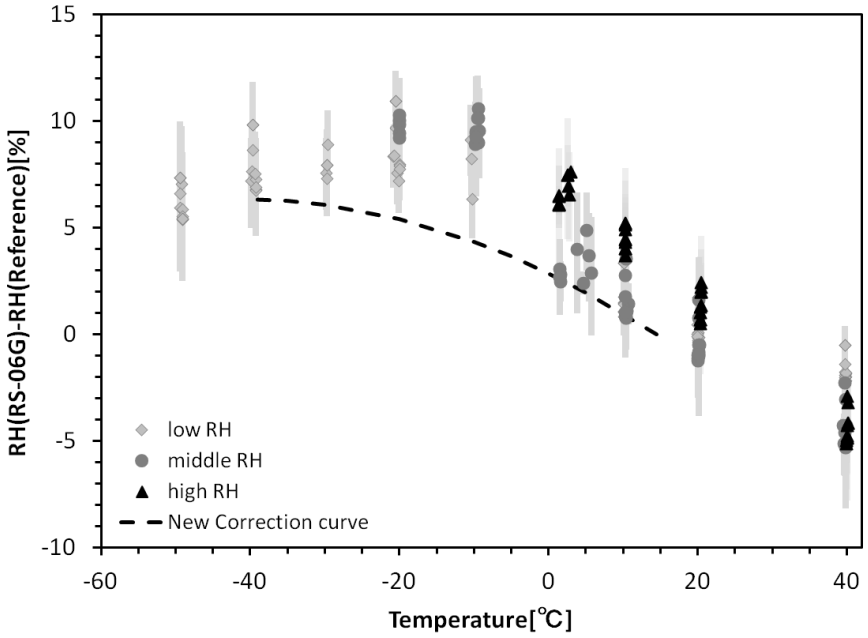

Fig. 2.9. As in Fig. 2.4 (top), but corrected by Eq. (2.16) for a modeled thermal lag effect. The dashed line represents the correction curve extrapolated up to +14.5 °C. Vertical light gray bars represent the estimated magnitude of uncertainty from the thermal lag effect. The marks indicate the value derived from $C' = 307\,\mathrm{kg\,m^{\frac{1}{2}}\,s^{-2}\,K^{-1}}$ and the upper and lower limits of the light gray vertical bars indicate the uncertainty derived from Eq. (2.13).

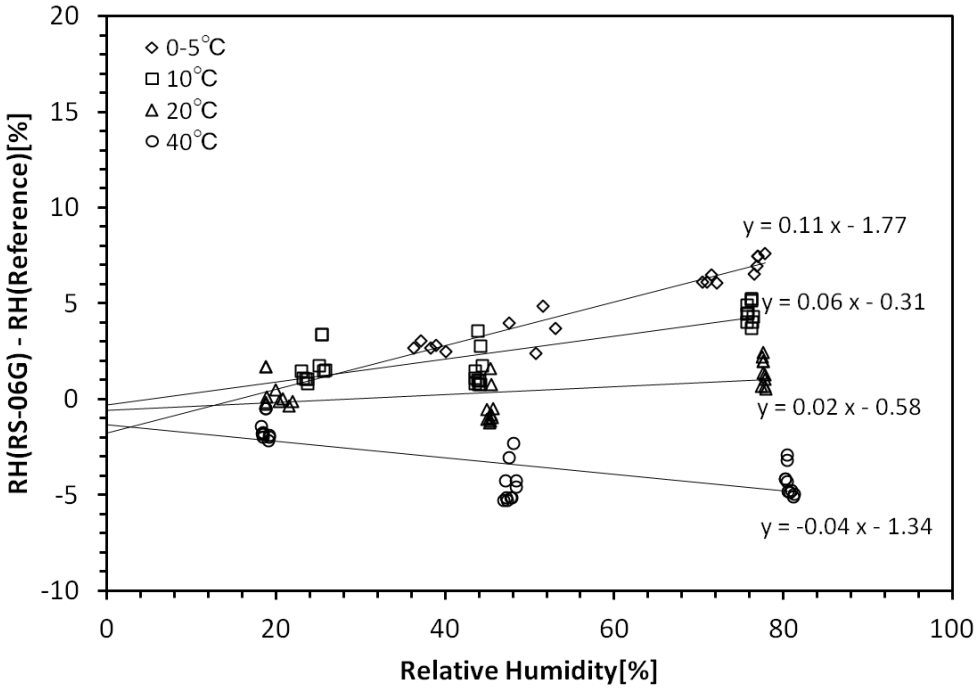

Fig. 2.10. As in Fig. 2.5, but corrected by Eq. (2.16) for a modeled thermal lag effect.

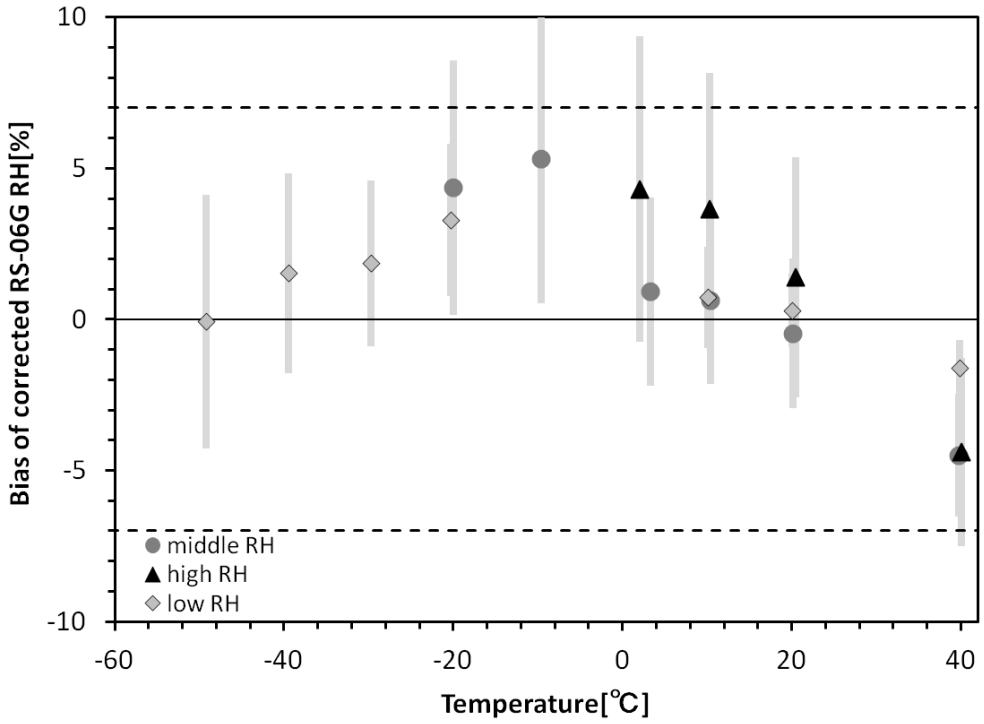

Fig. 2.11. Expected biases in the RS-06G RH measurements during a tropospheric balloon ascent based on the temperature and RH dependence of the sensor material and the thermal lag of the RH sensor. The results are indicated by gray squares (for < 30% RH), dark gray circles (for 30% to 70% RH), and black triangles (for > 70% RH) show that there remains a wet bias (< 5% RH) at –40 to +10 °C. Vertical light gray bars represent the uncertainty (k = 2). Dashed lines show ±7% RH, which indicate the manufacturer's specifications.

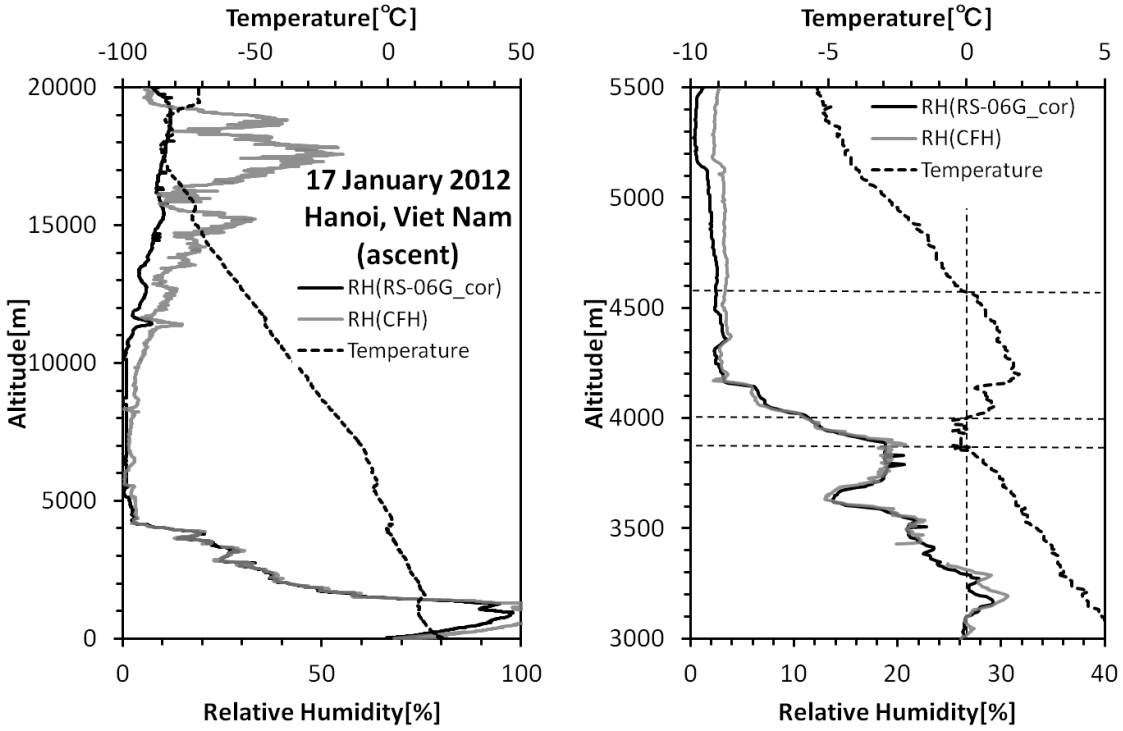

Fig. 2.12. As in Fig. 2.2, but for the RS-06G RH profiles with the new correction applied.

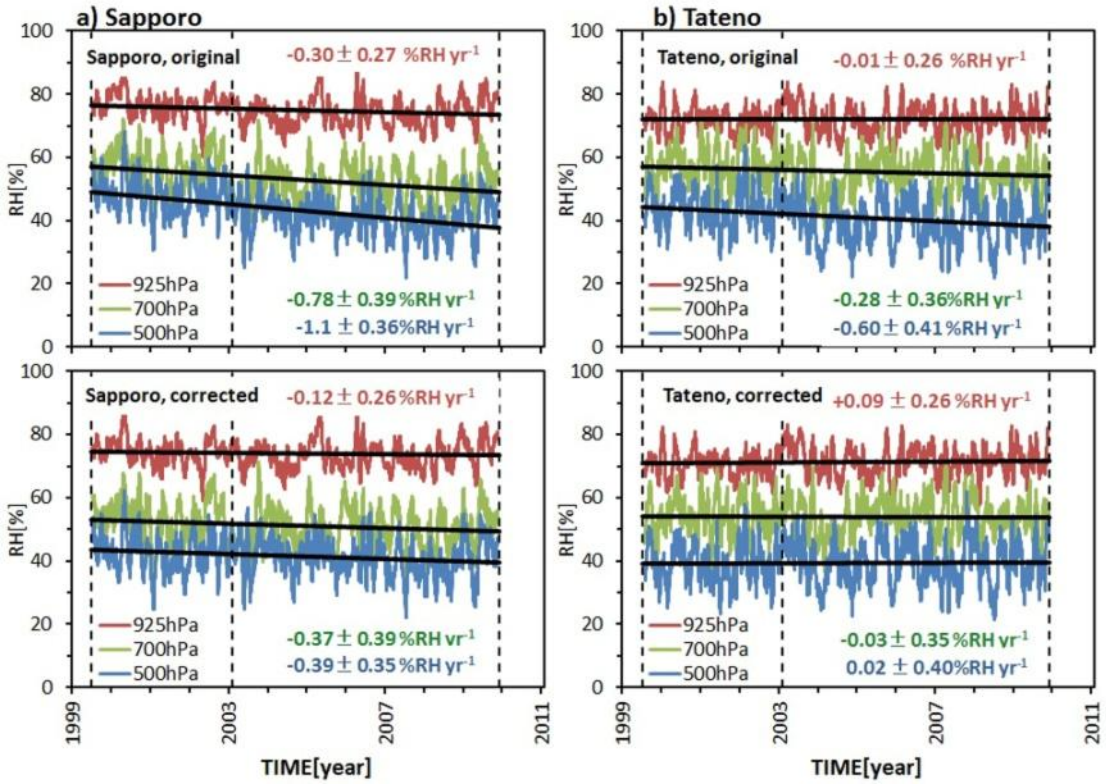

Fig. 2.13. Time series of deseasonalized and averaged RH for 31 days at 500 hPa (blue), 700 hPa (green), and 925 hPa (red) at Sapporo (a) and Tateno (b). Linear fits for the period from 24 June 1999 to 1 November 2009 for Sapporo, and from 13 July 2009 to 1 November 2009 for Tateno are shown as black lines. The values of the regression and 95% confidence interval for each time series are also shown. Top panels show the original IGRA time series; bottom panels show the corrected time series using the new T-D correction.

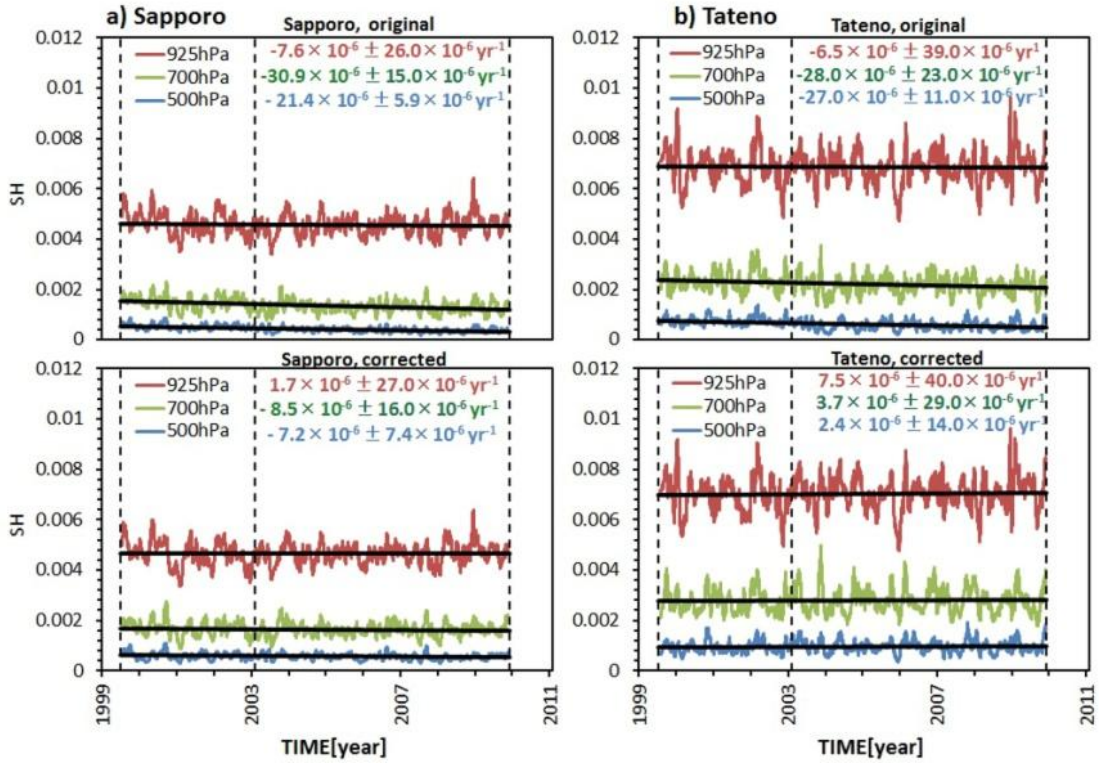

Fig. 2.14. As for Fig. 2.13, but for specific humidity.

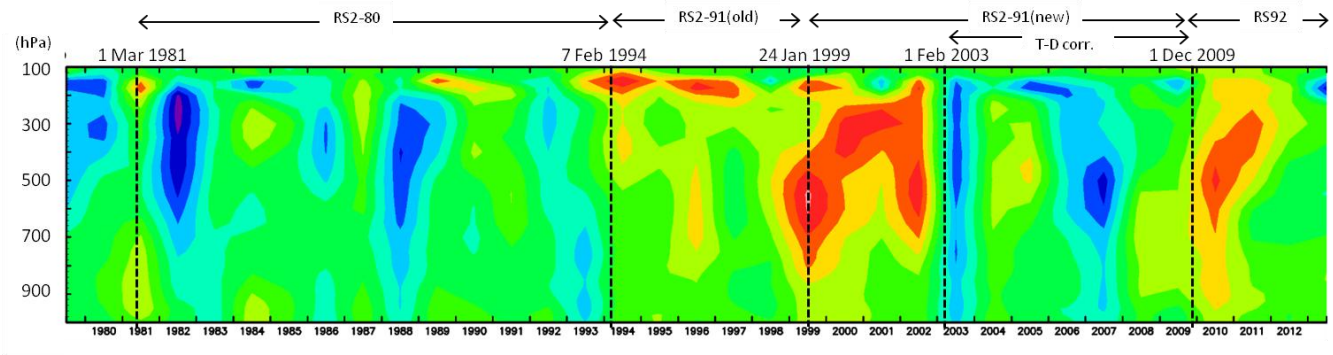

Fig. 2.15. Time series of anomalies of specific humidity in July for each year at 42.75°N, 141°E (the closest grid to the Sapporo station), using a reanalysis dataset (ERA-interim, Dee et al. 2011). The anomaly is with respect to the average for the whole period at each level. Dashed lines represent the change points in instruments.

Table 2. 1. Manufacturer's specification details for the instruments.

	RS-06G[1)]		FDW10	RF-100
	thermometer	hygrometer		
Manufacturer	Meisei	Meisei	Azbil Corporation	ETI
Principle	thermistor	thin-film capacitive sensor	Chilled mirror hygrometer	platinum thermometer (PT100)
Range	-90°C ~+40°C	1~100%RH	-40~+100°C DP [2)]	-199.9 ~+199.9°C
Resolution	0.1°C	0.1% RH	0.1°C DP	0.01°C
Accuracy	±0.5°C (2σ)	±7%(2σ)	±0.5°C DP	±0.05°C (-30°C ~+150°C) ±0.1°C (other conditions)

1) Serial numbers (and the sensor age, months after the production date) of radiosondes used in the experiment are 100261 (0 months), 100262 (0 months), 100270 (9 months), 100977 (5 months), 101587 (2 months), 102259 (0 months), 102260 (0 months), 102261 (0 months), 102262 (0 months), and 102263 (0 months).

2) °C DP represents dew/frost point temperature.

Chapter 3
Development of a Peltier-based chilled-mirror hygrometer

A chilled-mirror hygrometer is a high-accuracy sensor based on the thermodynamic principle, which is used as a transfer standard to compare between national humidity standards (Amano 2011). In this study, we have developed a chilled-mirror hygrometer for upper-air measurement, using the sensor probe of the FINEDEW™, which is a commercial chilled-mirror hygrometer for industry use produced by Azbil Corporation (the former Yamatake Corporation).

Section 3.1 describes the principle of chilled-mirror hygrometry and conventional chilled-mirror hygrometers. Section 3.2 describes the details of the newly developed instrument. Section 3.3 provides the results of some test flights including comparison results with other hygrometers. Section 3.4 provides experiments in a chamber, and Section 3.5 discusses the measurement uncertainty of the developed instrument. Finally, we summarize the development of the chilled- mirror hygrometer in Section 3.6.

3.1 The chilled-mirror hygrometry

3.1.1 Measurement principle

A chilled-mirror hygrometer can directly measure the dew point or frost point temperature of the ambient air. This hygrometer actively maintains the equilibrium of a two phase consisting of liquid water (or ice) on the mirror and water vapor in

the adjacent air. The mirror temperature, i.e. the temperature of the condensate, is continuously adjusted so that the condensate amount on the mirror to be maintained constant. When the condensate does not grow nor shrink, the mirror temperature is expected to be equal to the dew point or frost point temperature of the ambient air, depending on the phase of the condensate. The Clausius-Clapeyron equation (Eq. 1.1) describes the relationship between the vapor pressure and the dew/frost point temperature in equilibrium between the two phases. We can calculate water vapor pressure from the mirror temperature using the Clausius-Clapeyron equation.

Most chilled-mirror hygrometer uses optical detection system to monitor the condensate amount on the mirror. Some instruments (e.g., the Surface Acoustic Wave (SAW) frost point hygrometer developed at Jet Propulsion Laboratory; the SAW frost point hygrometer developed at the University of Cambridge (Hansford et al. 2006)) use a crystal to detect the condensate amount with changes in the oscillation frequency. For the optical detection method, the intensity of the reflected light or scattered light from the mirror is monitored by a photo-detector. Since the intensity of reflected/scattered light corresponds to the condensate amount, the chilled-mirror hygrometers keep the intensity to be constant by a feedback controller (e.g., using a proportional-integral-derivative (PID) controller.), and measure the mirror temperature continuously as dew/frost point temperature. In general, the temporal change of condensate amount becomes smaller and slower under low-temperature conditions because of smaller water vapor content in the air. Therefore, a high-resolution and low-noise detecting system is required for stable measurements at low temperatures. Also, the ambient light such as sunlight often

causes problems for the optical detectors. Some instruments reduce this light contamination by shielding the sun light and/or by filtering out electronically using electronically modulated light.

There are two main methods to control the mirror temperature. One is cooling by a Peltier device. The other is cooling/heating using a cryogen material and an electrical heater. The Peltier device consists of two semi-conductors, one n-type and one p-type, which can transfer heat from one side of the device to the other with consumption of electrical energy. When Direct Current (DC) electricity flows through the Peltier device, one side becomes cooler while the other becomes hotter. A heatsink to the ambient air is attached to the hot side so that its temperature becomes close to the ambient air temperature by heat transfer. In this way the mirror, which is attached to the cold side, can be cooler than the ambient air, and thus can reach the dew/frost point temperature of the ambient air. In principle, the Peltier-based chilled-mirror hygrometers can measure the atmospheric water vapor from the surface to the lower stratosphere, if the dew/frost point depression is within the maximum temperature difference limit of the Peltier device used. In practice, the temperature of the hot side cannot be cooled up to the ambient air temperature especially at low pressure such as the stratosphere. The warming of the hot side causes the depression of the maximum cooling. Therefore, the aggressive cooling of the hot side is also required to measure stratospheric water vapor.

3.1.2 Conventional chilled-mirror hygrometer for balloon observation.

There are 3 conventional chilled-mirror hygrometers for meteorological balloons.

・National Oceanic and Atmospheric Administration (NOAA) frost point hygrometer (NOAA FPH)

The NOAA FPH is the balloon-born frost point hygrometer of NOAA's Earth System Research Laboratory (NOAA/ESRL), which have been used since 1980 at Boulder, USA (Mastenbrook and Oltmans 1983; Vömel et al 1995). This instrument provides the longest stratospheric water vapor record (Hurst et al. 2011). The NOAA FPH uses a liquid cryogen material (Trifluoromethane, CHF_3) to cool the mirror, and an electrical heating wire to heat the mirror. The controller uses only a proportional controller with two step parameters. This controller inherently produces oscillations in measured frost point temperature in the stratospheric region, and the data are moving-averaged (Vömel et al. 2007). The measurement uncertainty for this instrument is limited by the controller stability and is around 0.5K in frost point temperature under optimal performance. Also, several minor improvements have been added to this instrument since 1980 (e.g. Vömel et al. 1995). However, the principle has not been changed, and it is believed that the data quality is almost constant.

The weak point of this instrument is that the cryogen (CHF_3) is needed to cool the mirror. CHF_3 has more than ten thousand times stronger greenhouse effect as compared with CO_2 (Montzka et al. 2009). The NOAA FPH needs about 300 cc of liquid CHF_3 at one observation.

・Cryogenic Frostpoint Hygrometer (CFH)

The CFH was developed in the mid-2000s, based on the NOAA FPH. The significant improvements enabled the CFH to measure the tropospheric water vapor as well as stratospheric water vapor (Vömel et al, 2007a). The improvements

are as follows: (1) the power consumption, weight, and cost are reduced; (2) a digital PID controller is applied using a microprocessor; and (3) solar light contamination is reduced by using an electronically modulated light. Many researchers consider that the CFH is a reference instrument for balloon-borne water vapor observation. The measurement uncertainty is estimated as less than 0.5 K from the surface to the mid-stratosphere. However, it was recently reported that there is a measurement bias more than 0.5 K in the lower troposphere (e.g., WMO 2011).

In chilled-mirror hygrometers, the phase of the condensate on the mirror often brings an ambiguity; it is not clear whether the mirror temperature is frost point or dew point temperature if the phase is not known. The CFH control algorithm eliminates this ambiguity by a forced freezing, that is, applying an artificial strong cooling the mirror up to -38˚C, at a preset mirror temperature of -12.5˚C. This forced freezing allows a clear identification of the liquid to ice transition. Murphy and Koop (2005) suggested that at very cold temperatures (T < 200 K) water ice may exist not only with its normal hexagonal crystal structure but also with a cubic crystal structure. The vapor pressure of the cubic ice is 3 – 11 % higher than that of hexagonal ice, which would influence the frost point hygrometer measurement. The CFH controller operates so as to evaporate and immediately reform the frost layer at -53˚C. It is known that at this temperature only hexagonal ice will form from water vapor. In this way, the frost layer is maintained into the colder region and will remain in the hexagonal phase. The performance is evaluated by comparison with various hygrometers, e.g., NOAA FPH, the Microwave Limb Sounder (MLS) on the Aura satellite, Fluorescent Advanced Stratospheric Hygrometer for Balloon (FLASH-B) Lyman-alpha instrument, and Vaisala RS92 radiosonde (Miloshevich et

al 2006; Vömel et al. 2007a, 2007b, 2007c).

・Snow White hygrometer

The Sow White is a Peltier-based chilled-mirror hygrometer, which has been in production by a Swiss meteorological instrument company, Meteolabor AG since 1996. The preparation and the operation are very simple, only connecting the dry-cell batteries. The Snow White has a 3 mm×3 mm mirror, which is at the same time a thermocouple thermometer, consist of two thin metal (copper, and constantan plated with gold), attached on the cold side of a Peltier device. The mirror and optical devices are situated in a separated 3 cm ×1 cm ×5 cm metallic sensor housing. There are two types of the Snow White, a "day" type and "night" type. For the day type, the sensor housing is enclosed in a Styrofoam housing. For the night type, on the other hand, the sensor housing is exposed to the ambient air, to minimizing the water vapor contamination.

The Snow White's accuracy of the mirror temperature measurement is <0.1 K. The response time, which is largely determined by the time constant for the vapor-water or ice-vapor equilibrium, is negligible at +20˚C, 10 s at -30˚C, and 80 s at -60˚C (Fujiwara et al. 2003). The Snow white exhibits a lower detection limit of about 3%- 6% RH, depending on the cooling capacity of the Peltier device (Vömel et al. 2003). In some cases, loss of the frost point control within layers with RH below this detection limit caused inaccurate measurements even above these dry layers where the RH is within the detection range of the instrument (Vömel et al, 2003). In the stratosphere, the mirror temperature often indicates higher frost point temperatures than expected values even within the cooling limit, while the housekeeping data indicates that frost layer is under control (in other words, the

signal of the reflected lights indicates almost constant, i.e., in equilibrium). This problem makes us think that the measurements from the Snow White are doubtful even in the UT region. We assume that the cause of this problem is due to inappropriate controller setting. It should be noted that the electric circuit of the Snow White is analog and cannot set the advanced controller algorithm to keep the condensate in equilibrium. The author will develop a Peltier-base chilled-mirror hygrometer with a much advanced digital controller. The author will also discuss the reason of the problem in the Snow White hygrometer in Section 3.6, based on the knowledge obtained during the development of the new chilled-mirror hygrometer.

・Fluorescent Advanced Stratospheric Hygrometer for Balloon (FLASH-B) Lyman-alpha (FLASH-B)

The FLASH-B instrument was developed at the Central Aerological Observatory, Russia, for balloon-borne water vapor observations in the upper troposphere and stratosphere (Yushkov et al. 1998, 2000). The instrument is based on the fluorescent method (Kley and Stone 1978), which uses the photodissociation of water vapor (H_2O) molecules at a wavelength < 137 nm, followed by the detection of the fluorescence of excited OH radicals. The FLASH-B is not an absolute instrument for water vapor measurements, and thus needs the calibration processes in laboratory, but has fast response even at the stratosphere.

3.1.3 Purpose of the development of a new instrument

Conventional hygrometers do not fulfill the measurement accuracy required for climate monitoring. Although the required accuracy shown in Table 1.1 corresponds

to ~ 0.1 °C frost point (FP), the accuracy of the most reliable instrument (CFH, NOAA FPH) is ~0.5 °C FP. It is essential to improve the water vapor measurement technique for climate monitoring.

The CFH and NOAA FPH are currently considered as a most reliable instrument for climate monitoring purpose. However, these instruments need a cryogen material (CHF_3), which has a very strong greenhouse effect. Because the emission of CHF_3 is regarded as an issue environmentally, it is considered that the CFH and NOAA FPH are unsuitable for the climate monitoring. Also, the use of cryogen makes the operation complex. On the other hand, although the Snow White hygrometer can measure the lower and middle tropospheric water vapor, the measurements in the UT/LS are not reliable and their uncertainty cannot be quantified. Therefore, in this study, we have developed a new Peltier-based chilled-mirror hygrometer with a digital controller, by converting a chilled-mirror hygrometer for industry use, the FINEDEW™.

3.2 Instrument development description

Figures 3.1 and 3.2 show the schematic of the developed chilled-mirror hygrometer and the photo, respectively. The mirror is a thick silicon wafer, whose size is 2 mm × 2.5 mm(Fig. 3.2 (b)). A PT100 thermometer is located between the mirror and the cold side of a Peltier device. A two-stage Peltier device is used, and has larger cooling capacity than the Snow White. This instrument uses the intensity of the scattered light from the mirror to monitor the condensate (dew/frost) amount. Therefore, the surround of the mirror is relatively clear because the photo-detector

and the light source are at the same location. Also, the individual deference of the detection sensitivity is considered to be smaller than that of the reflectivity detection method of the Snow White, CFH, and NOAA FPH. An electrically modulated light is used to prevent light contaminations as well as the CFH. The weight of the developed instrument is less than 300 g, including dry-cell batteries (one 9V type battery and four CR123 type batteries). This instrument is environmentally-friendly and ease-to-handle in nature because this sensor does not use a cryogen material.

This instrument does not have transmitter itself. We usually connect it with the Meisei RS-06G radiosonde, which can send the additional data of 25 byte/sec from the externally-connected instrument together with the basic data (temperature, relative humidity, position information by the global positioning system (GPS), etc). This instrument monitors the mirror temperature at 2 Hz and the intensity of the scattered light at 2Hz, the DC electricity of the Peltier device, the heatsink temperature, and the battery power levels. Data other than the mirror temperature are used as the housekeeping data to monitor whether the system is working properly and assess the measurement uncertainty. The mirror temperature is expected to correspond to the dew/frost point temperature when the equilibrium is established between vapor and liquid water/ice. We can convert the dew/frost point temperature to the vapor pressure using the Clausius-Clapeyron equation (Eq. 1.1). Combining other simultaneous radiosonde measurements (e.g., temperature and air pressure) from the RS-06G, we can convert the vapor pressure data to the other forms of the water vapor concentrations (e.g., relative humidity and volume mixing ratio).

3.2.1 Cooling capacity of the Peltier device

The mirror is cooled by a two-stage Peltier device. Figure 3.3 shows the cooling capacity measured in an environmental chamber, which indicates the dependence on air temperature, air pressure, and flow rate near the mirror. The cooling capacity is calculated by the heat budget on the mirror: the heat transfer by the Peltier effect, the Joule heat, and heat exchange with ambient air (Sugidachi 2011). The temperature difference ΔT that is created by a Peltier device is written as

$$\Delta T = \frac{\frac{R_e I^2}{2} + \alpha I T_{air}}{-\alpha I + \beta + HS} \tag{3.1}$$

where R_e [Ω] is the resistance of the Peltier devise, I [A] is the DC through the Peltier device, α [V K^{-1}] is the capacity of the Peltier device derived from the material and the size, T_{air} is air temperature, β [W K^{-1}] is the coefficient associated with the thermal conduction of the Peltier device, H [W m^{-2} K^{-1}] is the heat transfer coefficient between the mirror surface and air temperature. Under the assumption of laminar flow, H can be written as

$$H = 0.0143 U \rho \left(\frac{\kappa}{\mu}\right)^{\frac{2}{3}} c_a^{\frac{1}{3}} \tag{3.2}$$

where U is air flow, ρ [g m^{-3}]is air density, κ [W K^{-1}] is thermal conduction, μ [m s^{-1}] is the viscosity of air, c_a [J g^{-1} K^{-1}] is heat capacity of air (Sakata 2005; Kubota 2009; Sugidachi 2011).

Equations (3.1) and (3.2) show quantitatively the environmental dependence of the Peltier device. When temperature is higher and pressure is lower, ΔT becomes

larger. We estimate from the experimental results (Fig. 3.3) and from the equations to be the ΔT is more than 55˚C at the surface (corresponding to ~1%RH at air temperature of 25˚C) and ~30˚C in the LS region (corresponding to less than 0.1 ppmv at 100 hPa).

The Peltier device creates the temperature difference between the cold side (mirror) and the hot side (heatsink). When the air is dry, the peltier DC continues to flow to cool the mirror, and then the heatsink would become warmer and warmer even if the heat release of the heatsink is efficient. The warming of the heatsink causes the depression of the maximum cooling. To reduce this effect and to add extra cooling effect on the hot side, we also use liquid ethanol as an additional cooler of the heatsink. With evaporation of the ethanol from the heatsink surface, the heatsink loses heat because of the latent heat. Ethanol is easily-handled material, and non-freezing at stratosphere. The latent heat of evaporation for ethanol is 853 J/g. Heat capacity of the hotside is about 30 J/K. Therefore, if all latent heat is ideally provided from the heatsink, ethanol of 10 g can have cooling capacity of accumulated temperature of ~200 ˚C. If we use the system shown in Fig. 3.4, we can pour the ethanol simply when air pressure is decreased gradually because the ethanol is pushed out by the expansion of air. This technique is used at the silicone oil supply in the HYVIS (HYdrometeor VIdeoSonde) (Orikasa and Murakami 1997). Figure 3.5 shows the effect of the heat of evaporation in a chamber experiment. In this experiment, the ethanol of 15 g can cool the heatsink by 15˚C compared to the case of no ethanol. Although we have applied this technique for some of the test flights, the effectiveness during the actual sounding has not been quantified yet. Further test flights under various conditions are needed to determine the optimum

amount of ethanol.

3.2.2 PT100 thermometer.

Mirror temperature is measured with a platinum resistance temperature detector (PT100), which measures temperature by correlating the resistance of the PT100 element with temperature. The PT100 has a unique and repeatable and predictable resistance-temperature (R-T) relationship. Platinum is the best metal for resistance temperature detector because it follows a very linear resistance-temperature relationship in a highly repeatable manner. The unique properties of platinum make it the material of choice for temperature standards (Immler et al. 2010). We use the four-wire configuration to measure the resistance of the PT100. The four-wire configuration increases the accuracy and reliability of the resistance being measured; the resistance error due to the lead wire resistance is cancelled out.

The accuracy is determined by the calibration of the PT100 and a constant current circuit to measure the resistance (voltage) of the PT100. We have calibrated the PT100 individually to characterize individual R-T relationship of the PT100. We have calibrated the PT100 to the working standard used at the factory of the Meisei Electric Co. LTD. over the temperature range +40 to -85°C. Also, we have calibrated the constant current circuit individually to measure the resistance of the PT100 accurately. Figure 3.6 shows an example of the relationship between the reference resistance and the resistance measured from the circuit (top panel), and the error from the calibration curve (bottom panel). The standard uncertainty is 0.07 K in this case. The error value is different for each circuit, but the degree is nearly equal (0.07 K ± 0.02 K). Figure 3.7 shows the relationship between the reference

temperature from the working standard and the resistance of PT100 (top panel), and the error from the calibration curve. This standard uncertainty is 0.03 K. Also, the error of the working standard is 0.058 K (0.1/√3). As a result, the measurement uncertainty (σ =1) of the mirror temperature is 0.1 K.

3.2.3. Feedback Controller

In this study, a proportional-integral-derivative (PID) controller is used as the feedback controller to maintain the equilibrium of the condensate amount. The PID controller is widely used in industrial control systems. The PID controller calculates an output value by using an "error" value as the difference between a measured process value and a desired set point. The controller attempts to minimize the error by adjusting the process control inputs. In the chilled-mirror hygrometer developed here, the measured process value, the desired set point, and the control outputs correspond to the scattered light intensity from the condensate, the desired scattered light intensity (arbitrary set), and the DC of Peltier device, respectively.

In general, the control output of the PID controller is calculated as follows:

$$u(t) = K_p\{e(t) + \frac{1}{T_i}\int_0^t e(\tau)d\tau + T_d\frac{de(t)}{dt}\} \tag{3.3}$$

where $u(t)$ is the control output, $e(t)$ is error, K_p is a proportional gain, T_i is the integration time, and T_d is the derivative of time. A high K_p results in a large change of the output. Increasing the gain will make the feedback control go highly-responsive and unstable. Decreasing the gain will the feedback controller stable and low-responsive. If the controller has only proportional term, an offset error will remain. The second term in the parenthesis is the integral term. The

integral action eliminates the offset. The last term is the derivative term. The derivative action predicts the system behavior and thus improves the stability.

We need to set the PID parameters (i.e., K_p, T_i, and T_d) to achieve optimal control. The PID parameter for a chilled-mirror hygrometer needs to be changed with various atmospheric conditions by gain scheduling (Vömel et al. 2007a). Physically, the feedback control on a chilled-mirror hygrometer is related to the speed of the deposition and evaporation of condensate, which depend strongly on the degree of supersaturation around the condensate on the mirror. It is a reasonable assumption that the PID parameters should be changed with the water vapor pressure, i.e., the mirror temperature. We have tuned the PID parameters using the ultimate sensitivity method proposed by Ziegler and Nichols (1942). It is performed by setting as $T_i = \infty$, and $T_d = 0$. The K_p is then increased gradually until it reaches the ultimate gain K_u, at which the output oscillates with a constant amplitude. K_c and the oscillation period T_u are then used to set the PID parameters according to the empirical rule, $K_p = 0.6K_u$, $T_i = 0.5T_u$, and $T_d = 0.125T_u$

We have conducted the experiment for PID tuning in a thermostatic chamber. Figure 3.8 shows examples of the PID tuning. For these examples, four different values of K_p were given for ~100 sec. The final ultimate gain values are $K_p = 1/4$ at -20 °C and $K_p = 1$ at -50 °C. We found that the value of K_c tends to become larger at low temperatures and that T_u is almost constant with temperature. We have determined the PID parameters under the empirical rule, and adjusted by further trial and errors. We have finally set K_p as a function of mirror temperature T_m. T_i and T_d are constant. The PID parameters are updated every second during the sounding.

3.2.4. Inlet tube

We use the relative movement (ascent/descent) of the payload to introduce the measurement air to the sensor. The mirror is put in a short inlet tube of ~ 5 cm long. The strong airflow makes the cooling limit smaller as shown in Fig. 3.3, and the disturbed airflow makes the feedback controller unstable. Therefore, we have adjusted the airflow by using an inlet tube, whose shape is such that the cross-section area of inlet is about half of that of the exit. This inlet tube is expected to bring a half of the ascent speed near the mirror.

Also, there was a concern whether the airflow is enough in the inlet tube under low-pressure conditions, i.e., in the stratosphere. To confirm the airflow in the inlet tube during the sounding, we have measured the airflow in some inlet tubes with different cross-section areas during a balloon ascent by an airflow meter which has been developed for this purpose (Sugidachi 2011). This airflow meter uses the principle of a hot-wire airflow meter, which is calibrated under low pressure and low-temperature conditions to measure the airflow in the upper-air. The uncertainty (σ =2) is within +/- 1.0 m/s. We prepared four kinds of inlet tube: (1) the one with diameter (D) = 15 cm, length(L) = 30 cm, (2) D = 3 cm, L = 30 cm, (3) D= 2 cm, L = 30 cm, and (4) area of inlet = 2 cm $\times$2 cm, area of outlet = 3 cm $\times$3 cm. Figure 3.9 shows the photo and schematic of the inlet tubes and profiles of the airflow in each inlet tubes. The effects of the pendulum motions are filtered out by a moving average of 100 sec. We found that the airflow in the inlet tube (4) is about half of those of (1) and (3) throughout the ascent sounding. The airflow of all the tubes is weaker at higher altitudes although the airflow does not become zero even

in the stratosphere.

We have used the inlet tube whose cross-section area of the inlet is about half of that of the exit. To minimize the contamination error by cloud droplets, however, we have not used the inlet tube, i.e., the mirror is exposed at atmosphere, at the 7th sounding (daytime). Also, we have used the shorter inlet tube shown in Fig. 3.2 at the 8th and 9th soundings (daytime).

3.3 Test flights

We have conducted the test flights nine times as shown in Table 3.1. The results of all flights are described in Appendix C. The development phase is divided into three major phases as follows:

1) The experimental phase with a prototype using a hand-made electric circuit with the original FINEDEW™ sensor probe;

2) The second phase with a printed circuit board with the original FINEDEW™ sensor probe; and

3) The final phase with a printed circuit board with the sensor probe modified for upper-air measurements.

In this section, the author discusses the performance of the developed chilled-mirror hygrometers. Section 3.3.1 describes the tropospheric measurement, and Section 3.3.2 describes the upper tropospheric and stratospheric measurements.

Table 3.2 List of the test flights

	Date	Place	Comments (development phase)
1	Jan. 28, 2011 14:30(LT)	Moriya, Japan (35.98 °N, 140.00 °E)	(1)
2	Nov. 04, 2011 14:01(LT)	Sapporo, Japan (43.07 °N, 141.35 °E)	(2)
3	Dec. 01, 2011 17:41(LT)	Moriya, Japan (35.98 °N, 140.00 °E)	(2)
4	Jan. 07, 2012 17:27(LT)	Biak, Indonesia (1.18 °S, 136.11 °E)	(2); simultaneously with CFH*;
5	Jan. 10, 2012 18:42(LT)	Biak, Indonesia (1.18 °S, 136.11 °E)	(2); simultaneously with CFH, FLASH*
6	Jan. 13, 2012 15:49(LT)	Biak, Indonesia (1.18 °S, 136.11 °E)	(2)
7	Jan. 10, 2013 18:00(LT)	Biak, Indonesia (1.18 °S, 136.11 °E)	(2-3); simultaneously with CFH*,
8	Apr. 25, 2013 16:40(LT)	Moriya, Japan (35.98 °N, 140.00 °E)	(3)
9	Oct. 27, 2013 9:10(LT)	Moriya, Japan (35.98 °N, 140.00 °E)	(3)

* These soundings are conducted under the Soundings of Ozone and Water in the Equatorial Region (SOWER) project.

3.3.1 Tropospheric measurements

Figure 3.10 shows the profile of the 7th descent sounding at Biak, Indonesia, taken on 10 January 2013. The housekeeping data indicate that the system was working properly at below 15 km altitude (left panel in Fig. 3.10); the PID controller kept the intensity of the scattered light constant around the target value of 1.35 V. Therefore, it is expected that the mirror temperature was at the dew/frost point temperature below 15 km.

This sounding was conducted simultaneously with the CFH. Figure 3.11 shows the profiles from the developed chilled-mirror hygrometer and the CFH, and the difference between the two measurements (developed chilled-mirror hygrometer minus the CFH measurements). The comparison results show that the dew/frost

point temperature from the developed chilled-mirror hygrometer is consistent with that from CFH within ~0.5 K below 15 km, even the supersaturated region (13 -14 km).

In general, the ambiguity of the condensate phase causes the ambiguity whether the mirror temperature was frost point or dew point temperature. When the water drops on the mirror are cooled below freezing, the water drops are often kept as liquid phase (i.e., supercooled water) until about -10 ~ -30 °C (Fujiwara et al. 2003). Once the phase transition from dew into frost occurs, the ice crystal would never go back to liquid water until the mirror temperature approaches to 0°C (e.g., Ibata and Kanai 2006). Because this profile is taken from the descent measurement, the condensate on the mirror is frost above 4.5 km where the mirror temperature becomes 0 °C, and the condensate on the mirror is dew below 4.5 km. Also, we can distinguish the condensate (dew or frost) by the scattered light signal (blue line in Fig 3.10). The fluctuation of the scattered light from dew (water drop) is much greater than that from frost as well as that of reflected light methods (e.g. CFH). However, the signal of the Snow White does not indicate a similar fluctuation of the reflected light.

3.3.2 Upper tropospheric and stratospheric measurements

Figure 3.12 shows the profile of the 5th sounding at Biak, Indonesia, taken on 10 January 2012. This sounding was conducted simultaneously with the CFH and quasi-simultaneously with FLASH-B again under the SOWER project. Figure 3.12 shows the comparison with these instruments around the UT/LS region. We see that the developed chilled-mirror hygrometer shows a significant response delay

above 15 km. The conservative PID tuning (i.e., low gain) may have caused this slow response.

In the next sounding, the 6th sounding at Biak, Indonesia, on 13 January 2012, we set the PID parameters so that the sensor response becomes much faster. Figure 3.13 shows the ascent profile of the mirror temperature and the housekeeping data for the 6th sounding. Above 15 km, large oscillations of the mirror temperature continue up to 24 km. This is due to the too active PID tuning (i.e., high gain). The oscillation period is about a minute, and the amplitude is about +/- 2°C. As is often assumed for other balloon-borne chilled-mirror hygrometers, it is expected that the true frost point temperature are within the oscillation amplitude (+/- 2°C). Above 23.5 km, the signal of the scattered light continues to decrease. This means that the mirror temperature is above the frost point temperature. At this time, the Peltier DC reaches ~2 A, which is the maximum value. Therefore, it is considered the cooling limit of the Peltier device is reached as shown in Fig. 3.11. This sounding shows that the effective measurement range with current cooling system is below about 23.5 km in the tropics.

Further PID tuning may give better measurements. However, such a significant response delay and such an oscillation with the long period (~ 1 min) were not observed in the laboratory experiments even at a low temperature of -75°C. Therefore, it is considered that other factors such as the condensate size (and condensate formation process) on the mirror may be important factors regarding the response time. Large condensates would result in much slower measurements. In the next section, we explore the behavior of dew/frost on the mirror.

3.4 Condensate on the mirror

3.4.1 Phase transition

We investigated condensate on the mirror by using an optical microscope under several conditions. Figures 3.14 and 3.15 show the behavior of the phase transition at around -0 °C. This experiment was conducted at room temperature in the laboratory of the Faculty of Env. Earth Science at Hokkaido University in February 2012.

The condensate has been dew (supercooled water) for about 800 s ((1) in Fig. 3.15) since the control was started. The dews of 5 - 10 μm are uniformly formed on the mirror. Then, frosts started to form at the edge of the mirror at 800 s (2). The ice crystal grows gradually, while the number of supercooled water droplets decrease (i.e., dews were evaporating) (3). After a few hundred seconds, the supercooled water completely disappeared on the mirror (4). As compared with the dew point and frost point temperature calculated from the RS-06G RH and temperature, the mirror temperature seems to indicate dew point under the conditions(1)-(3), and frost point under the condition(4). Under the condition (1)-(3), the fluctuation of the scattered light is large (~ ±0.02 V s^{-1}). This means that the PID controller tries to make the dew amount constant (in equilibrium). However, the mirror temperature for conditions (2),(3) is expected to be between the dew point and frost point because frost was growing and dew was evaporating. Figure 3.14 also shows the difference between the mirror temperature and the dew/frost point temperature calculated from the RS-06G measurements. The experimental results show that the mirror temperature was nearly the dew point temperature when the condensate amount on the mirror is in the mixed phase. Therefore, we can determine whether the

mirror temperature is dew point or frost point temperature by the scattered light, that is, the mirror temperature is dew point temperature when the fluctuation of the scattered light is large, and the mirror temperature is frost point temperature when the fluctuation is small(~ ±0.001 V s^{-1}). Strictly speaking, the mirror temperature should have a bias to the direction of frost point slightly until all condensates change into frost. For the period from 1000 to 1400 sec in this experiment, the mirror temperature seems to be slightly (~0.2°C) lower than dew point from the RS-06G measurements. Therefore, it leads the conclusion that there is an additional bias of ~0.2°C at the phase transition period (approximately from -10°C to -20°C of the mirror temperature during balloon ascent). In the future, the forced freezing algorithm, similar to the CFH, will be applied so that the uncertainty due to the phase ambiguity is eliminated.

3.4.2 Ice size at low temperatures

To investigate the condensates at lower temperatures, we investigated the mirror surface in the thermostatic chamber. We observed that the large ice crystals formed from supercooled water by the phase transition are maintained at low temperature (~ -30°C) for 20-30 minutes.

We evaporated these large ice crystals by heating the mirror once, and re-formed the condensates under cold enough conditions of -20°C, -40°C, and -60°C. Figure 3.16 shows the condensates on the mirror. We can see that more and smaller ice crystals form at lower temperatures. For the developed chilled-mirror hygrometer, the intensity of the detection signals corresponds to the backscattering by the condensates on the mirror, which is considered to depend on the particle size and

the emitted light wavelength. Figure 3.17 shows the relationships between the size and the intensity of scattered light, assuming the backscattering by Mie scattering (Craig and Donald 1983; Arai 2013). The relationship can be approximated by a monotonically increasing function. Scattered light by a small particle cause weak signals. Because the target level of the scattered light intensity was set as a constant of 1.3 V throughout this experiment, it is expected that more ice particles are formed on the mirror when particle size is small, that is, under cold conditions.

It is not clear that why more ice particles are formed on the mirror at lower temperatures. For cloud microphysics, the number of ice forming nuclei (IN) increases nearly exponentially with degreasing temperature (Pruppacher and Klett 1997). As in the cloud formation process, the temperature dependence of condensate number on the mirror may reflect the temperature dependence of the IN on the mirror.

The size of the ice crystals on the mirror affects the response time. Thus, we discuss the response time of chilled-mirror hygrometer using an example of the Snow White observation in Section 3.6. The growth/evaporation speed of larger particles is slow, as shown in Section 3.6. Therefore, we need to form smaller condensates on the mirror by evaporating large ice in cold enough conditions at some point in a flight to obtain faster response in the UT/LS region where water vapor concentration is low.

3.5 Measurement uncertainty

Figure 3.18 shows the uncertainty of the dew/frost point temperature measurement. There are several sources of uncertainty, which are divided into

technical factors and principle factors. Technical factors are the mirror temperature measurement (1), the stability and response of the PID controller (2), and the contamination error by cloud/rain droplet (3). Principle factors are the ambiguity of the condensate phase (4), aerosol effects (5), and curvature effect (6). Additionally, the uncertainty of the vapor equation should be considered at the conversion into vapor pressure (7). If we calculate RH and mixing ratio by volume, the uncertainty of the air temperature and pressure measurements are also considered. The combined factor of technical and principle factors is the error by a response delay (8). These details are discussed below.

The uncertainty of the temperature measurement is 0.1 K (σ =1) as discussed in Section 3.2.2. The thermal gradient of the mirror is expected within 0.015 K from the viewpoint of the thermal conductivity. According to Murai et al. (2011), however, the original FINEDEW™ has a temperature bias depending on the difference between the air temperature and dew/frost point temperature, and the correction was needed. The error is considered to be caused by the thermal flow from the heatsink. Therefore, we have re-designed the sensor probe. We prevented the thermal flow from the heatsink by separating the heatsink and PT100 thermometer thermally. Note that the original FINEDEW™ does not need to consider the thermal effect because it is calibrated by the humidity standard instead of the temperature standard. Chilled-mirror hygrometers should be fundamentally calibrated by the humidity standard because they measure the humidity. But, there is no humidity standard under the low-pressure and low-temperature conditions such as those found in the upper air. Therefore, we took the traceability for the temperature measurement instead of that as humidity as is done for the CFH,

NOAA FPH, and Snow White under the assumption that the mirror temperature equals to dew/frost point temperature if the system is working properly.

The uncertainty of the stability and time response of the PID controller depends strongly on the PID parameters, altitudes, and weather conditions. In the case of the 6th flight tests, the amplitude of the oscillations reached +/- 2.0 K in the UT/LS region. Meanwhile, in the case of the 7th test flight, such oscillations were not observed. This means that we need to determine the uncertainty associated with the PID controller for every instrument and every sounding. The uncertainty is expected to be up to ±1.2 K(= 2.0/$\sqrt{3}$) at a maximum. Further soundings under various conditions are needed to establish this component of the uncertainty statistically.

To eliminate the contamination error by cloud water droplets is the greatest challenge for the water vapor measurement using balloon ascent. We have minimized the contamination by designing the inlet tube as small as possible, and by separating the instrument from the balloon using the unwinder of 51 m long. Further improvements would be needed in cloudy condition such as for the 3rd sounding. Heating the inlet tube is one possible solution.

The ambiguity of the condensate phase can be eliminated by monitoring the scattered light fluctuations as discussed in Section 3.4.1. However, there may exist a small bias (< 0.2 K) just before the complete transition to the frost. To eliminate this uncertainty completely, the forced freezing algorithm for the phase transition, an artificial strong cooling at a preset temperature, is required.

Solution of pollutants affects the vapor pressure. If the condensates are formed by solutions, its vapor pressure should be smaller than that of pure water (the

so-called Raoult's law). We have tried to protect the mirror from cloud droplets and aerosol particles by setting the mirror angle downward at the 7th sounding, obliquely downward (30˚ to vertical direction) at the 8th and 9th sounding, and perpendicular at the other soundings. Also, the gases other than water vapor may interfere the frost point temperature measurement. For the UT/LS region, HNO_3 is adsorbed readily into the ice surfaces to form nitric acid hydrates such as nitric acid tri-hydrate (NAT), which would increase the apparent frost point temperature (Szakáll et al. 2001). However, the experimental results by Thornberry et al. (2010) show that no detectable interference in the measured frost point temperature was found for HNO_3 mixing ratio of up to 4 ppb. The actual amount is less than 0.1 ppb to several ppb in the UT/LS. We would require further study to assess the effect by aerosol particles and interference of other gases.

We may need to consider the curvature effect (surface tension) to calculate the vapor pressure from the dew/frost point temperature, when the condensate size is small. The size of the condensate on the mirror in the liquid phase is about 5 – 10 μm (Fig.3.16), and the size of the ice particles on the mirror is about 2 – 5 μm at the temperature of -60 ˚C. The saturation vapor pressure over ice particles is written as

$$\frac{e_i(r)}{e_i(\infty)} = exp\left(\frac{2\sigma}{r\rho_w \mathrm{R}T}\right) \tag{3.4}$$

where $e_i(r)$ is vapor pressure over ice with radius r, and σ is surface tension (Pruppacher and Klett 1997). Using $\sigma = 106 \pm 3$ erg cm-2 (Pruppacher and Klett 1997) and r = 1 μm, we obtain $e_i(r)/e_i(\infty) \approx 0.002$. Therefore, the particle size contributes little to the frost point temperature measurement of ~0.02 K ($\{e_i$(T+0.02)- e_i(T)$\}/ e_i$(T) $\approx$ 0.002).

The response delay is related with the PID parameters and the particle size. To assess the response time, we have to change water vapor concentrations arbitrarily. However, it is technically-difficult to change water vapor concentration at low temperatures. In this study, we use the stepwise change of the target level of the scattered light intensity instead of the stepwise change of the water vapor concentration to investigate the response time (stabilization time). Here, we define a stabilization time as a time to fit within the criterion (target level ± 0.015 V) once the stepwise change is given. The stabilization time is found within 5 sec even at -60˚C, when the stepwise change of 0.5 V is given for the target level of the scattered light (Fig. 3.19). This result suggests that an optimum PID controller and small enough condensates would results in only a few second delay even in the low-temperature conditions. In addition to these factors, we need to consider the time constant derived from the heat capacity of the mirror and PT100 when the water vapor concentration (frost point temperature) actually changes. However, this evaluation is very difficult because of the difficulty of making a stepwise change of water vapor concentration in low temperature conditions.

3.6 Discussion of the issue/problems on the Snow White hygrometer

For the chilled-mirror hygrometer developed in this study, we saw that larger ice crystals on the mirror may cause slower response. Thus, we hypothesize that the Snow White hygrometer has this problem. Figure 3.20 shows an example of the observation from the Snow White sounding. In the stratosphere, the mirror temperature (red line) indicates higher frost point temperature than the expected values even within the cooling limit, i.e., below 22 km, while it seems that the signal

of the reflected lights is almost constant (middle panel in Fig. 3.20). Such a behavior is almost always observed in the Snow White soundings at Sapporo during 2003-2013 (a total of 30 sounding). We found that the same problem (drying mirror in the LS) 28 cases out of the 30 soundings at Sapporo.

We investigate closely the signal of the reflected light as shown in the right panel of Fig.3.20. It is seen that the reflected light is gradually increasing above 14 km. This indicates that the condensates on the mirror become smaller and smaller by evaporation, that is, they are not equilibrium. This is probably because the feedback controller does not work properly. Here, let us estimate the evaporation rate of the condensate on the mirror, using the equation of the evaporation rate of a droplet falling from the cloud base (Pruppacher and Klett 1997).

In the case of a falling droplet, the evaporation rate can be calculated from

$$\frac{dr}{dt} = \frac{D_v}{r\rho_w \mathrm{R}}\left(\frac{e(T_\infty)}{T_\infty} - \frac{e(T_r)}{T_r}\right)\bar{f_v}$$

$$\bar{f_v} = 1.00 + 0.108(Sc^{\frac{1}{3}}Re^{\frac{1}{2}})^2 \qquad (3.5)$$

where r is the radius of the drop, D_v is the diffusion coefficient, ρ_w is the density of water, R is the gas constant for water vapor, $e(T_\infty)$ is vapor pressure for ambient air temperature T_∞, $e(T_r)$ is vapor pressure for drop surface temperature T_r, and , $\bar{f_v}$ is ventilation coefficient. Sc ($= \frac{\mu}{\rho D_v}$, μ is dynamic viscosity, D_v is the mass diffusivity) is the Schmidt number, and Re ($= \frac{\rho v L}{\mu}$, L is characteristic linear dimension, v is kinematic viscosity) is the Reynolds number.

In the case of a condensate on the mirror, assuming that the condensate is a spherical ice crystal, the evaporation rate can be calculated from,

$$\frac{dr}{dt} = \frac{\mathrm{D}_v}{r\rho_w \mathrm{R}_v}\left(\frac{e(\mathrm{T}_{fp})}{\mathrm{T}_a} - \frac{e(\mathrm{T}_m)}{\mathrm{T}_m}\right)\bar{f}_v \tag{3.6}$$

where T_{fp} is the expected frost point temperature in the stratosphere, and T_{m} is the mirror temperature of the Snow White. The evaporation rate depends strongly on the radius and the vertical gradient of the water vapor density near the mirror surface. Figure 3.21 shows the estimated evaporation rate for the particles with the radius of 2, 4, and 20 μm in the stratosphere. The results indicate that the condensate on the mirror remains for a long period of time if the condensate size is large enough (~20 μm) and that the small particles (~2 μm) evaporate rapidly. Therefore, we can conclude that for the Snow White, there are two key factors causing the above problem. One is that the condensates on the mirror are too large to detect the fluctuation of the frost at low temperatures. Another factor is the improper tuning of the feedback controller, which may be too conservative and cannot maintain the frost layer constant in the UT/LS region.

3.7 Summary and concluding remarks

A Peltier-based digitally-controlled chilled-mirror hygrometer has been developed to measure atmospheric water vapor accurately. The developed chilled-mirror hygrometer is environmentally-friendly and easy-to-handle in nature because this instrument does not use a cryogenic material to cool the mirror. Since January 2011, we have conducted nine test flights at Biak, Indonesia and Moriya, Japan to evaluate the performance of this instrument. The results of simultaneous measurements with the CFH at Biak, 10 January 2013 showed that the frost point temperature from the developed chilled-mirror hygrometer is consistent with that

from CFH within ~0.5 K below the troposphere. The result of the 6th sounding at Biak, 13 January 2012 showed that the developed chilled-mirror hygrometer can measure the lower stratospheric water vapor by the current Peltier cooling system. We need to reduce large oscillations in the UT/LS by a further PID tuning to reduce the measurement uncertainty.

We have also conducted several chamber and laboratory experiments. The observation of the condensates on the mirror shows that smaller ice crystals form at lower temperatures. Because the particle size affects the response time, we recognized a need to prevent large ice crystals from forming at the phase transient by making the heating algorithm some time at a flight. This algorithm is found to result in a faster response as shown in Fig.3.19.

We were able to obtain deeper understanding of the behavior of the chilled-mirror hygrometers through this development. The chilled-mirror hygrometer is often considered as an accurate hygrometer, but there are several problems that remain to be solved. The problem includes the evaluation of the PID controller, contamination errors by the cloud, aerosol effects, and measurement reliability of the mirror temperature (thermal gradient on the mirror). At the same time, we need to consider the improvement in the instrument production processes and the cost-cutting for long-term climate monitoring.

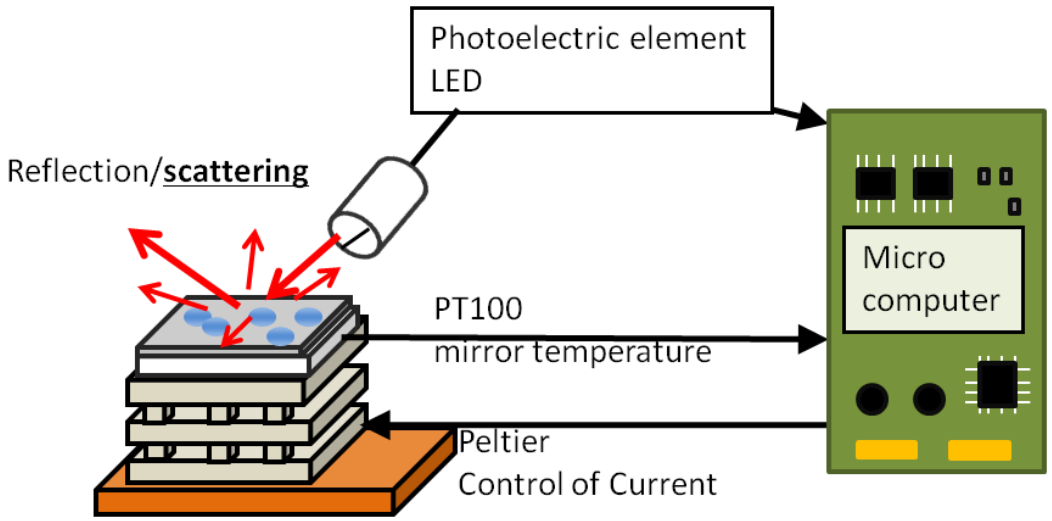

Fig. 3.1 Schematic of the measurement principle of the chilled-mirror hygrometer developed in this study.

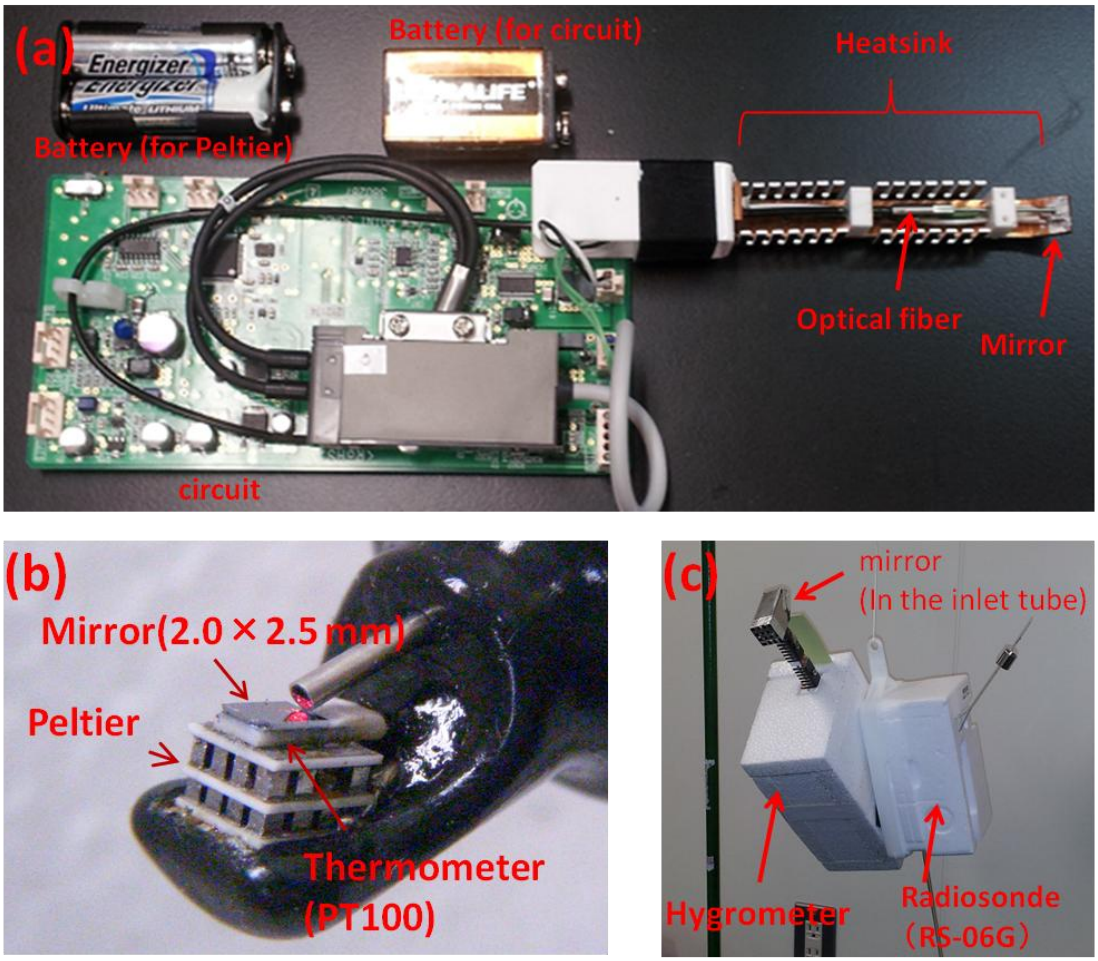

Fig. 3.2 The instrument developed in this study. (a) the sensor probe and electrical circuit, (b) a close-up of the mirror and the Peltier device part, and (c) the flight configuration with the RS-06G radiosonde at the development phase (3)

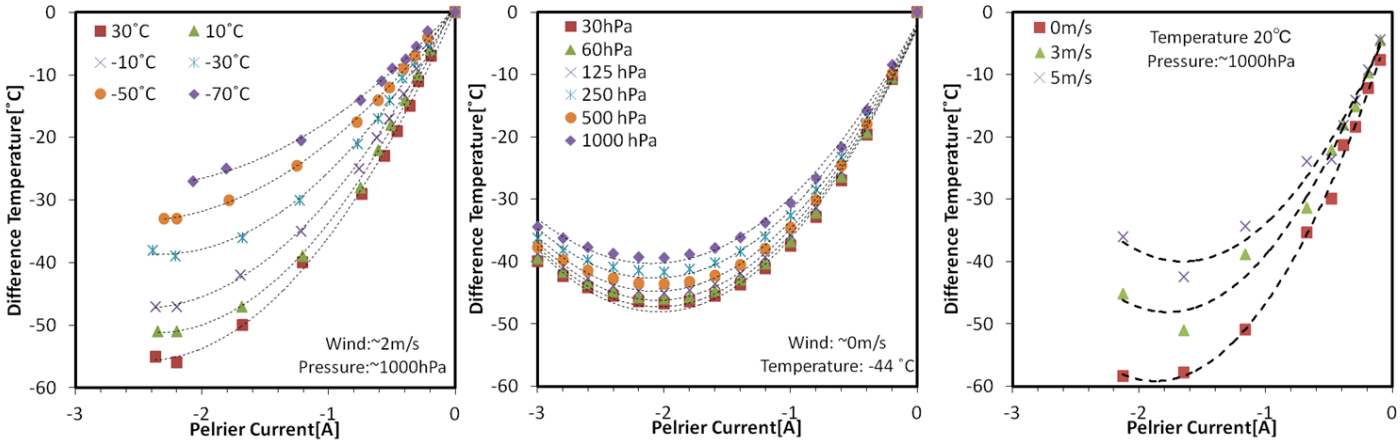

Fig. 3.3 Cooling capability of the Peltier device used in this study. Shown are the temperature differences between the cold side of the Peltier device and the ambient air against the Peltier current under various conditions obtained in a thermostatic chamber. The panels panel show the dependence on (a) air temperature, (b) air pressure, and (c) the airflow rate.

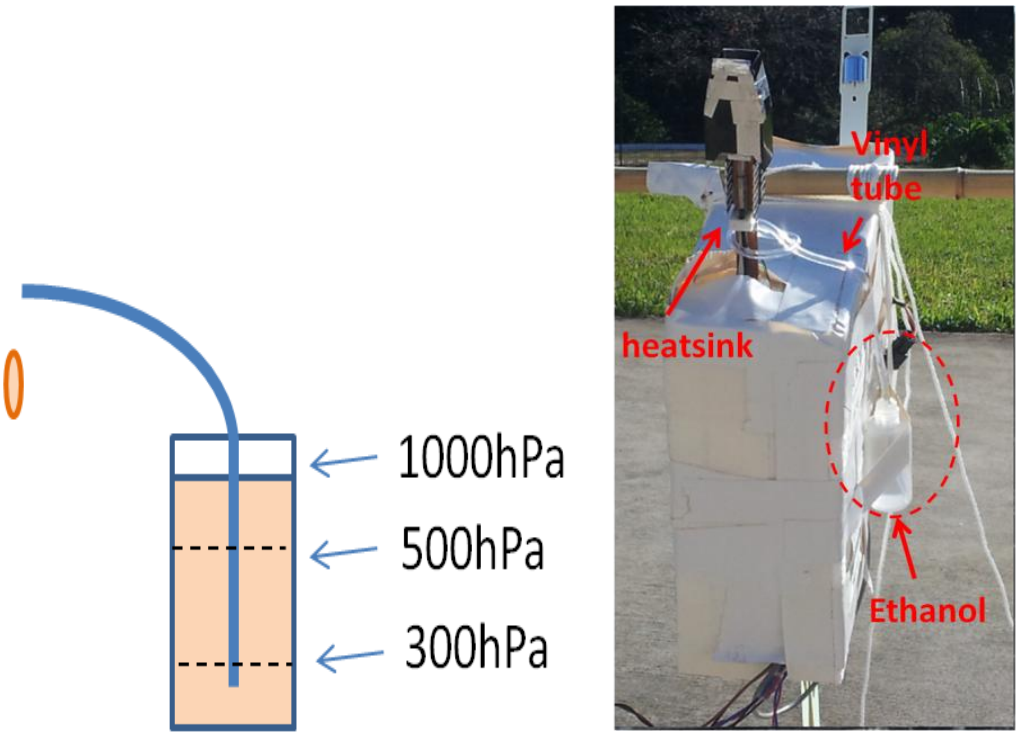

Fig. 3.4 Ethanol bottle for the heatsink cooling. The ethanol is pushed out by the air expansion in the top of bottle in low-pressure conditions.

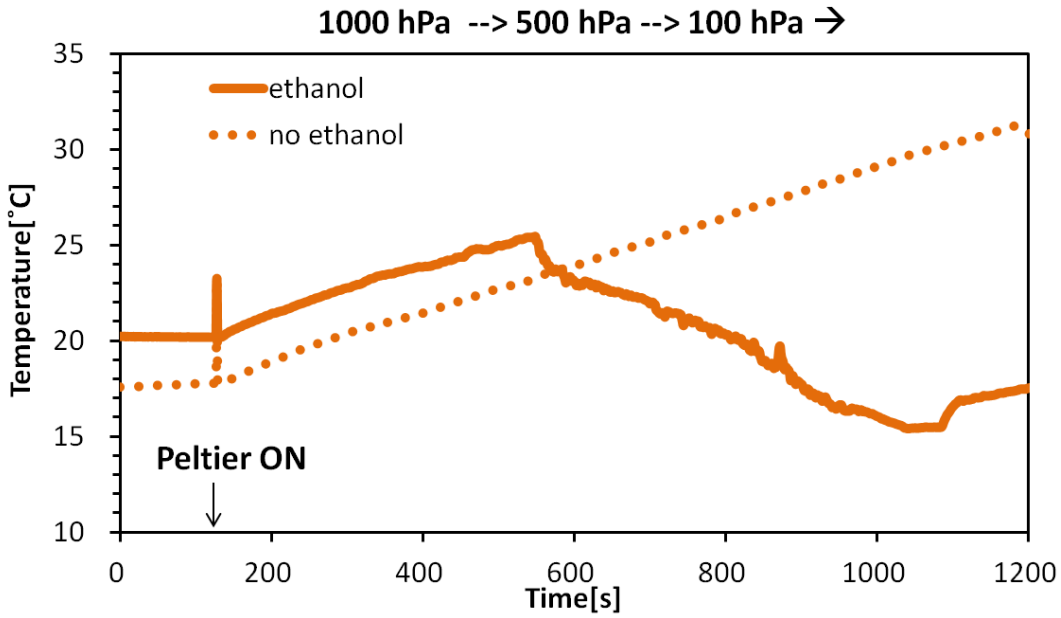

Fig. 3.5 Effect of the ethanol cooling in a pressure-controlled chamber. Solid line indicates the heatsink temperature when the ethanol cooling is used, and dashed line indicates the case where the ethanol is not used. The Peltier current starts to flow at 100 sec. The air pressure is reducing gradually (the approximate values shown at the top). Ethanol starts to be pushed out at ~500 sec for the solid curve case.

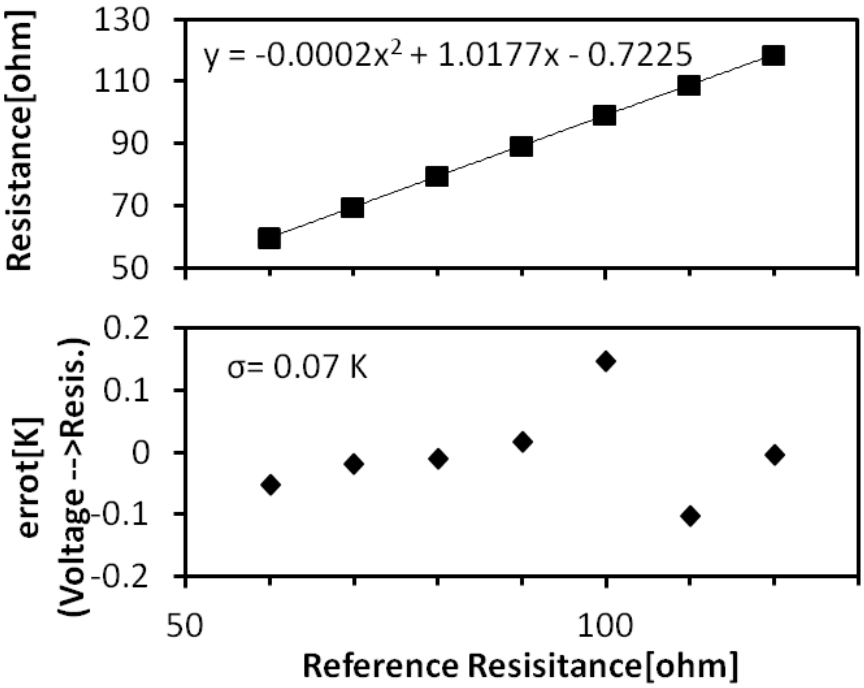

Fig. 3.6 Relationship between the reference resistance and the resistance measured by the developed circuit (top panel), and the error derived from the calibration fit (bottom panel). This error is converted from the resistance unit into temperature unit by using the relationship shown in Fig.3.7.

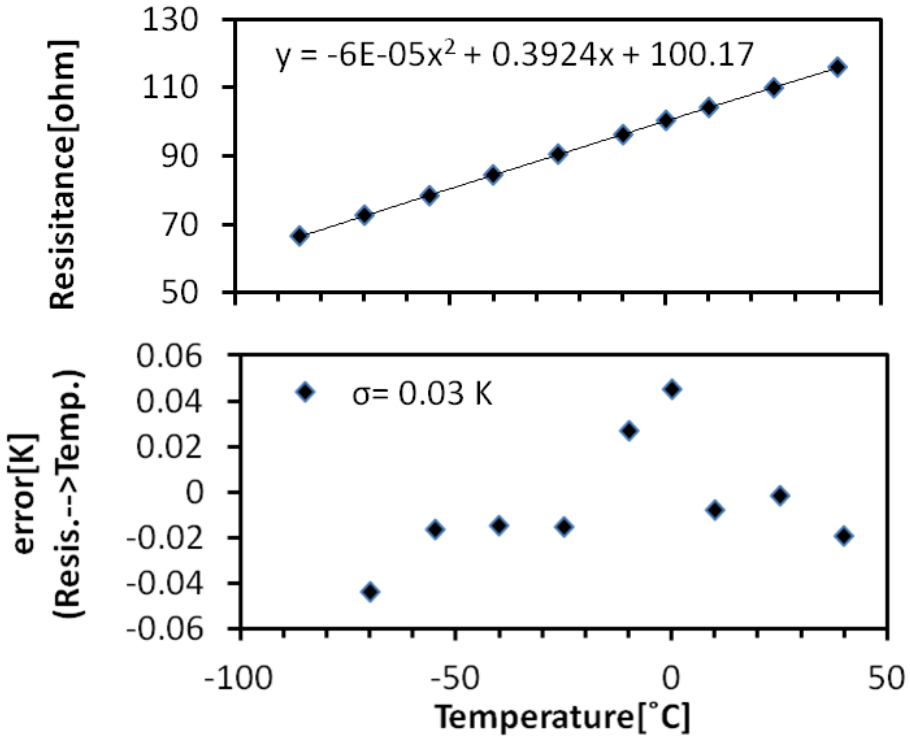

Fig. 3.7 Relationship of the resistance of the PT100 and the reference temperature (top), and the error derived from the calibration fit (bottom). The temperature is measured with a working standard at the Meisei Electric Co. LTD.

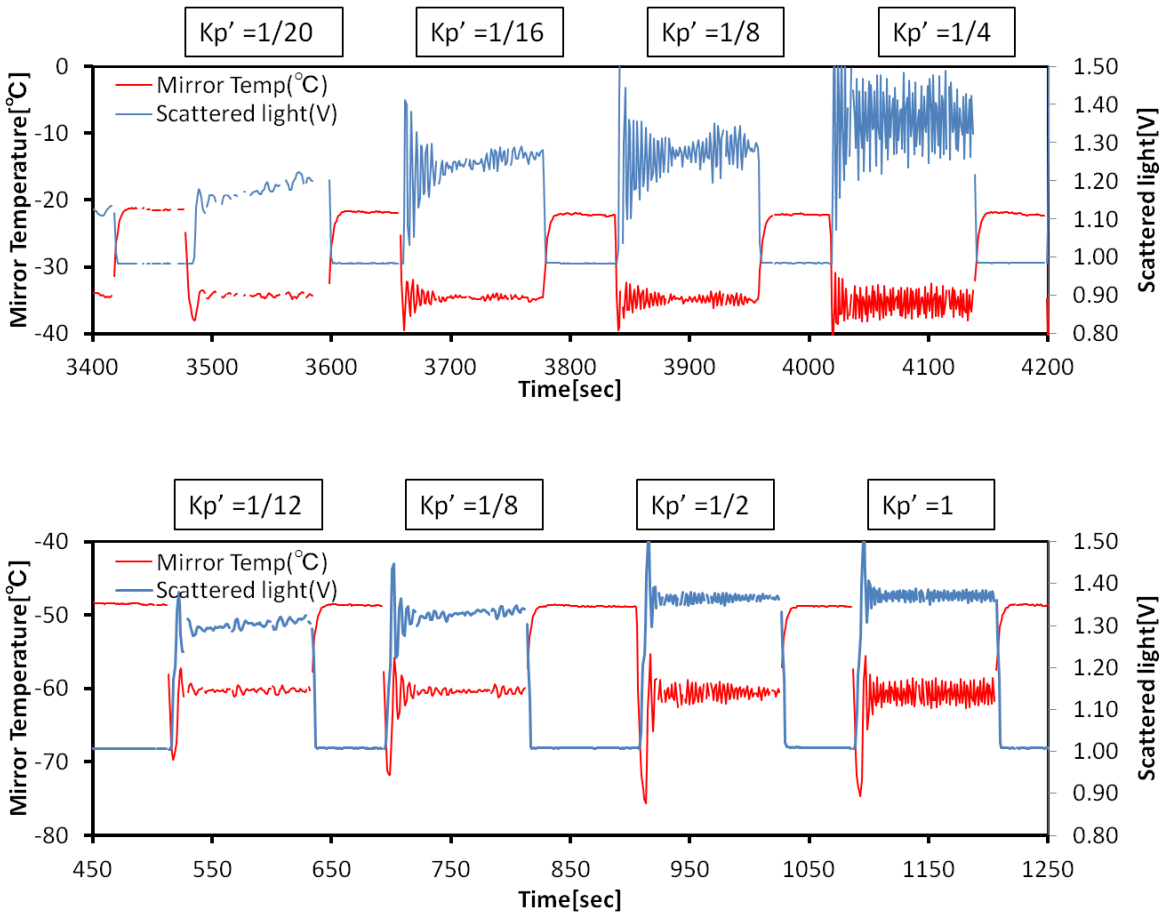

Fig. 3.8 An example of the ultimate sensitive method for T = -20 ˚C (top), and for T = -50 ˚C (bottom)

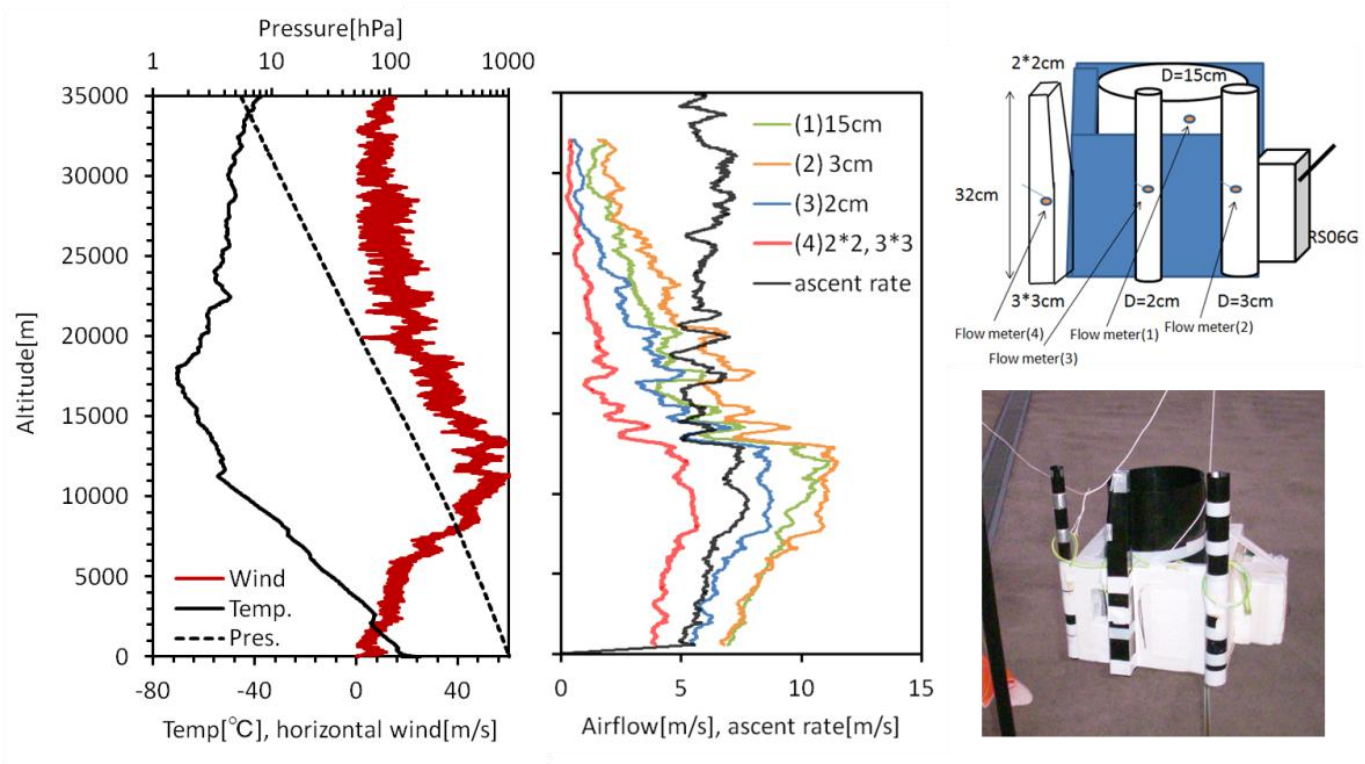

Fig. 3.9 Profiles of airflows in four different inlet tubes (right panel), air temperature, humidity, and horizontal wind taken at Moriya, Japan on 12 October 2011 (left). The effects of the pendulum motions are filtered out by a moving averaging of 100 sec.

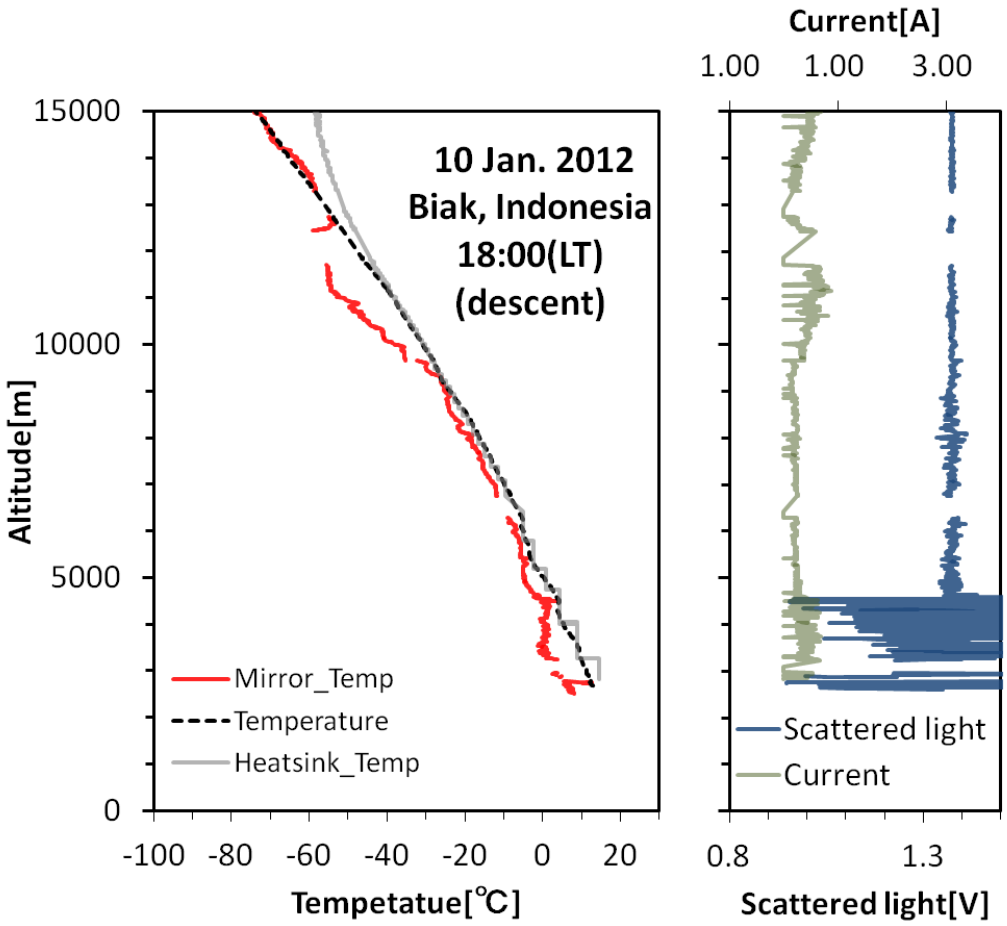

Fig. 3.10 Measured profiles for the 7th sounding taken at Biak, Indonesia on 10 January 2013. (left) Dew/frost point temperature and air temperature, (right) peltier current (green line) and intensity of the scattered light intensity (blue line) as the housekeeping data.

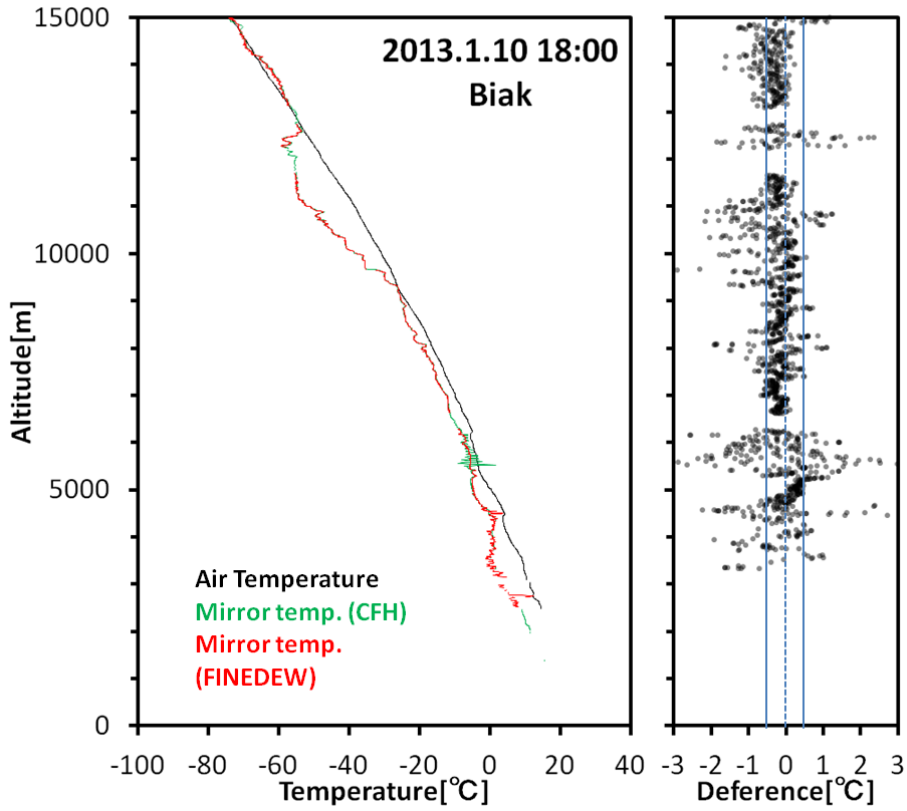

Fig. 3.11 Comparison with the CFH (left), and the difference temperature (right) for the 7th sounding taken at Biak, Indonesia on 10 January 2013.

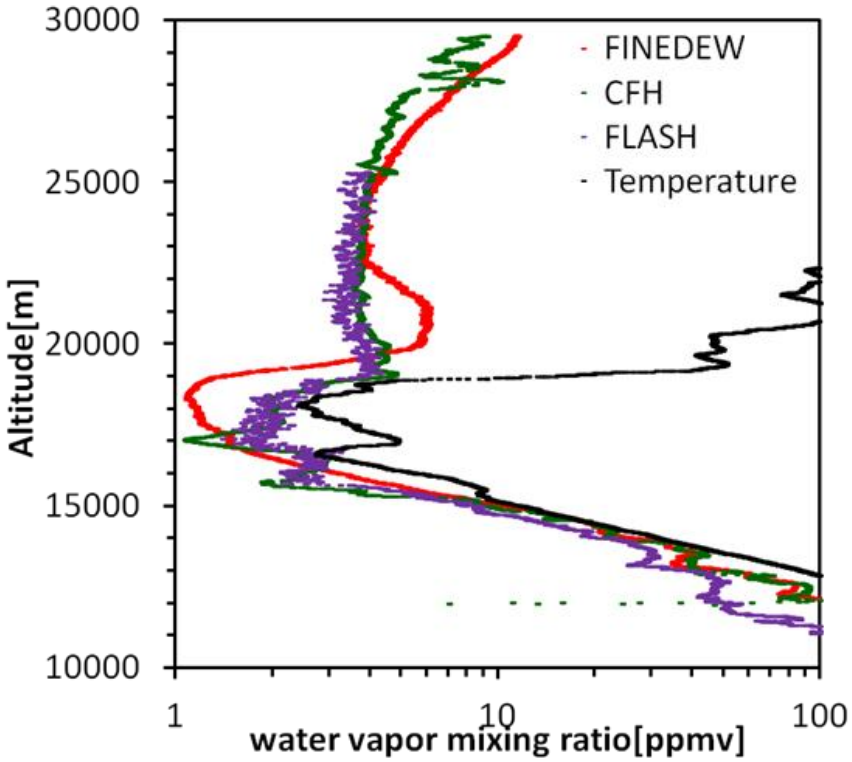

Fig. 3.12 Comparison with the CFH (green line) and FLASH-B (purple line) taken at Biak, Indonesia on 10 January 2012. Water vapor mixing ratio converted from the frost point temperature observed by the developed hygrometer (red), CFH (green), water vapor mixing ratio observed by FLASH-B (purple), and saturation mixing ratio estimated from air temperature (black) are shown.

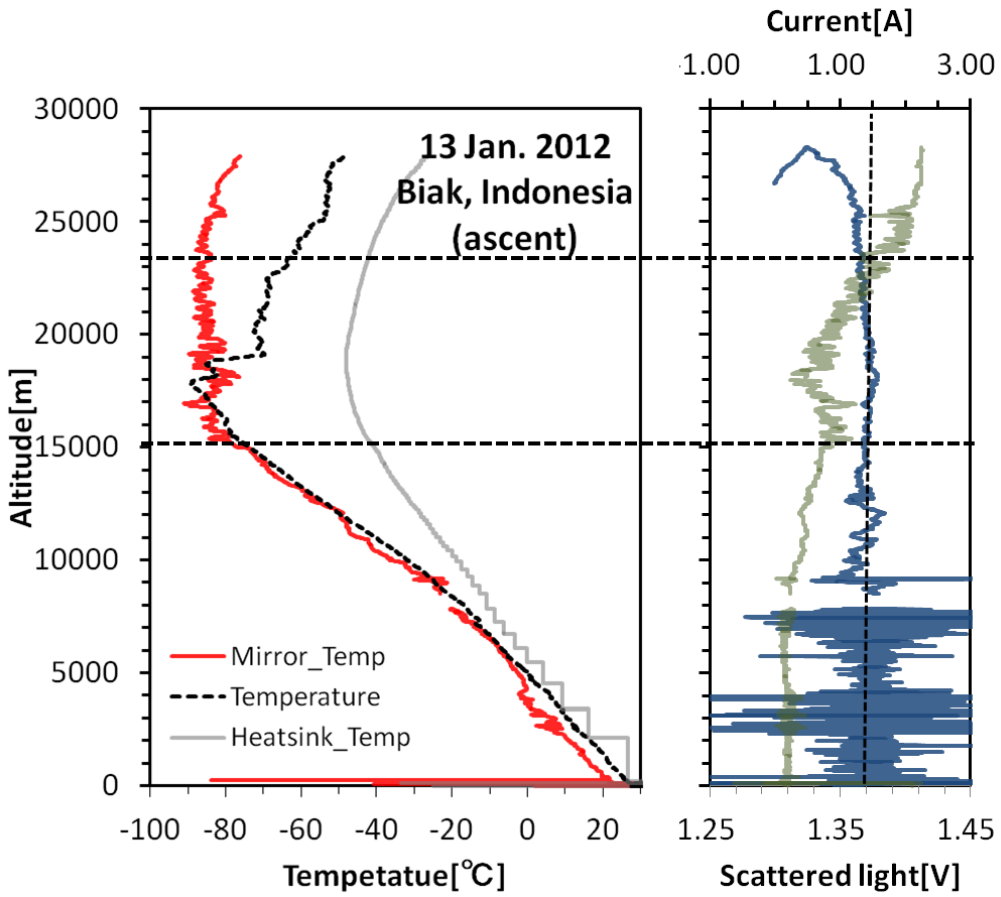

Fig. 3.13 Measured profiles for the 6th sounding taken at Biak, Indonesia on 13 January 2013. (left) Dew/frost point temperature and air temperature, (right) peltier current and intensity of the scattered light intensity as the housekeeping data.

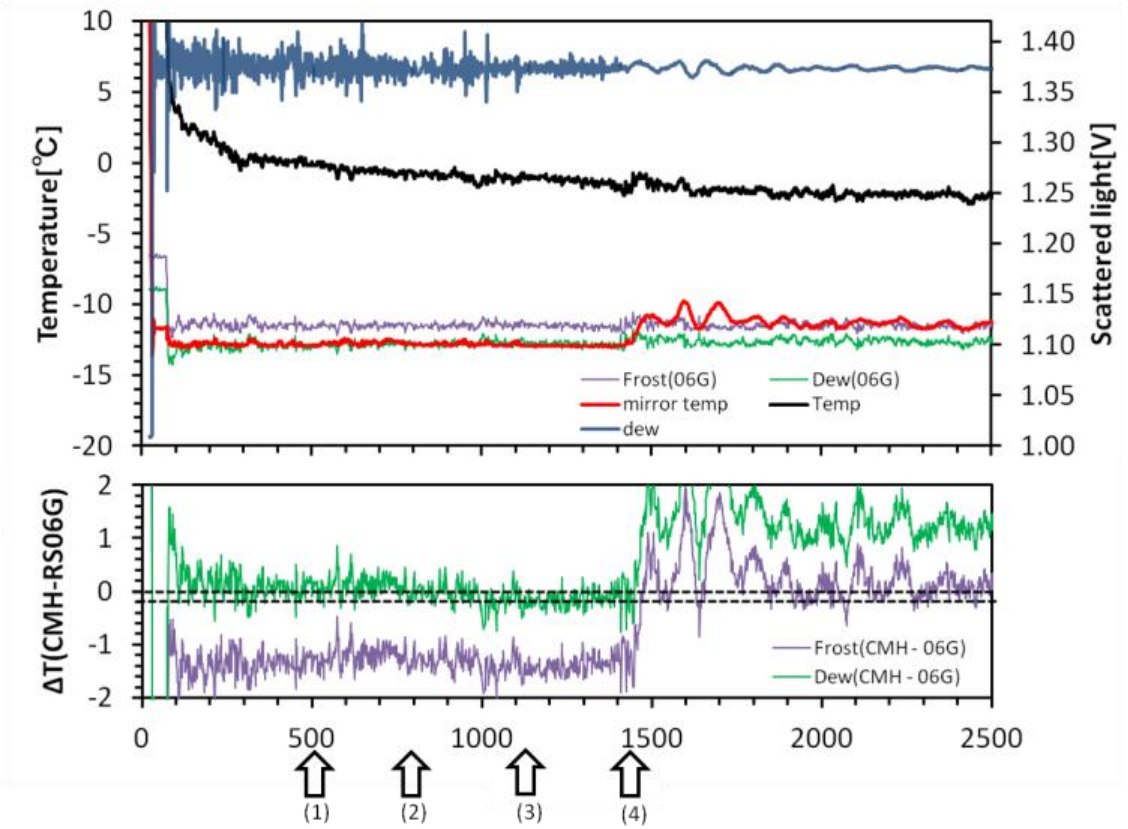

Fig. 3.14 Time series of the mirror temperature and dew/frost point temperature calculated from the Meisei RS-06G air temperature and RH in the laboratory. The RH from RS-06G is corrected by a dry bias of 2.5%RH constant which is probably due to sensor aging (Shimizu et al, 2007). Several months passed after this sensor packing is opened. Differences between the mirror temperature and the frost point temperature (purple line) and dew point temperature are shown (green line).

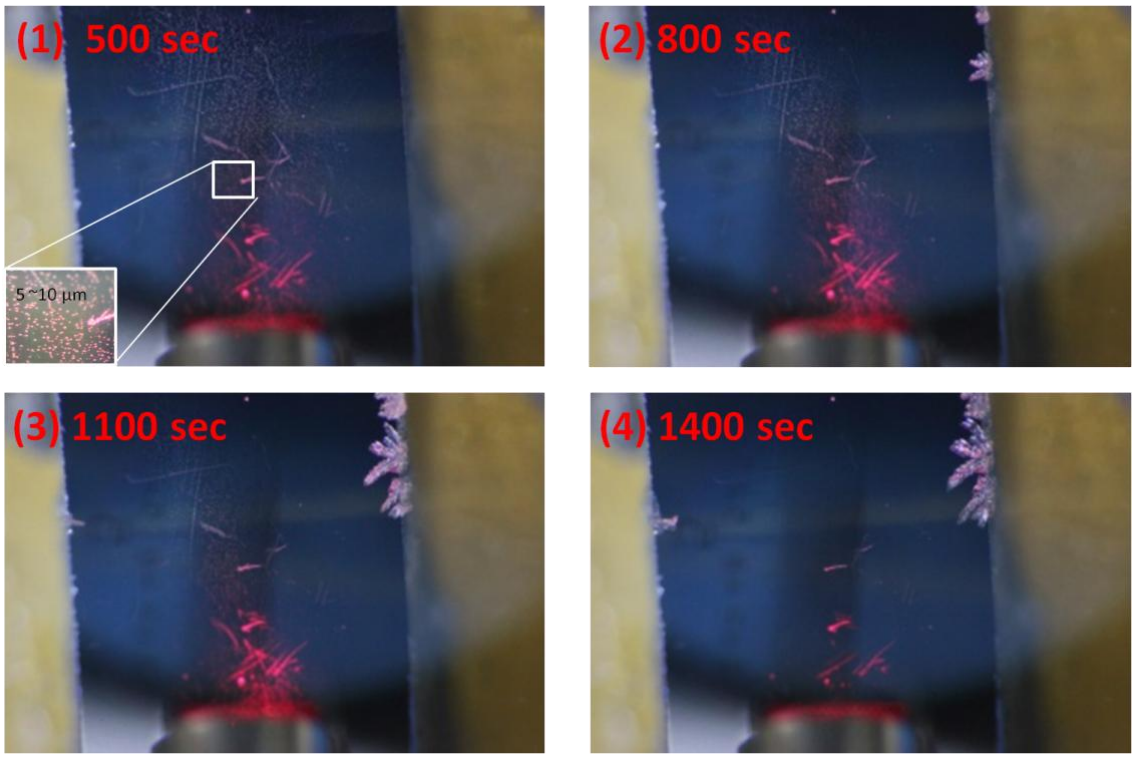

Fig. 3.15 Condensates on the mirror for the experiments shown in Fig 3.14. The photo numbers correspond to those in Fig. 3.14

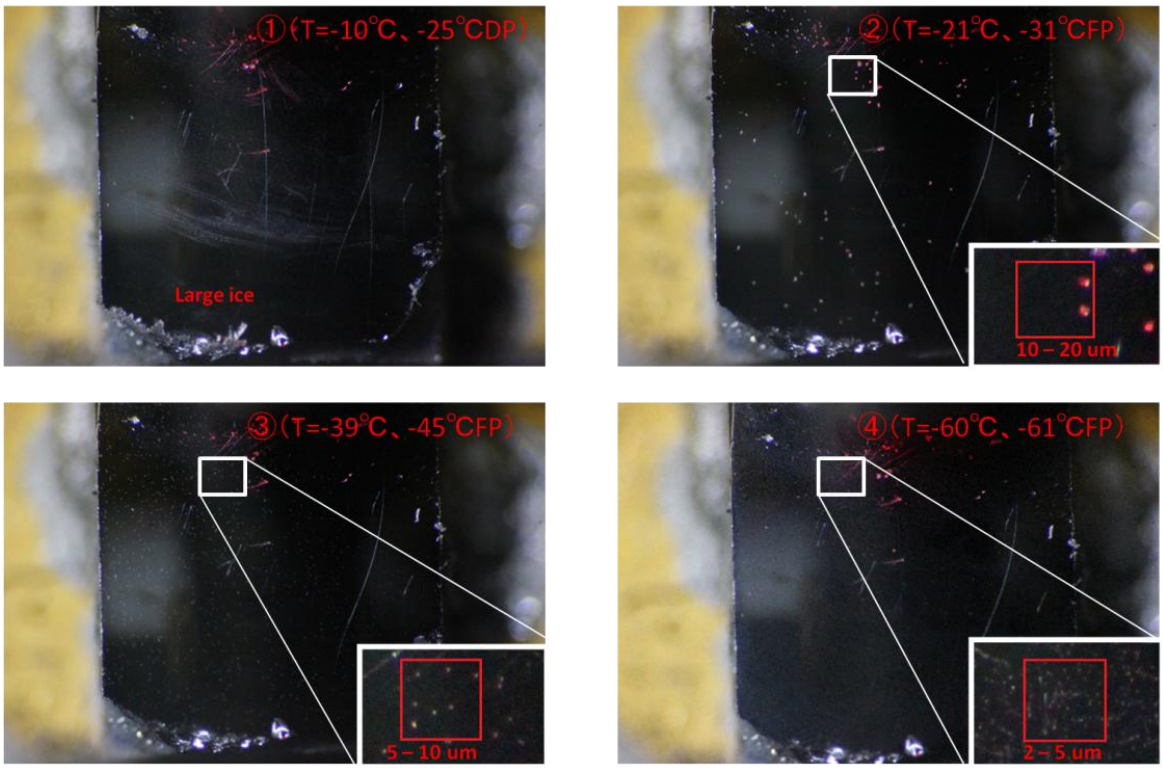

Fig. 3.16 Condensates on the mirror at temperatures of -10, -20, -40, -60°C in the thermostatic chamber.

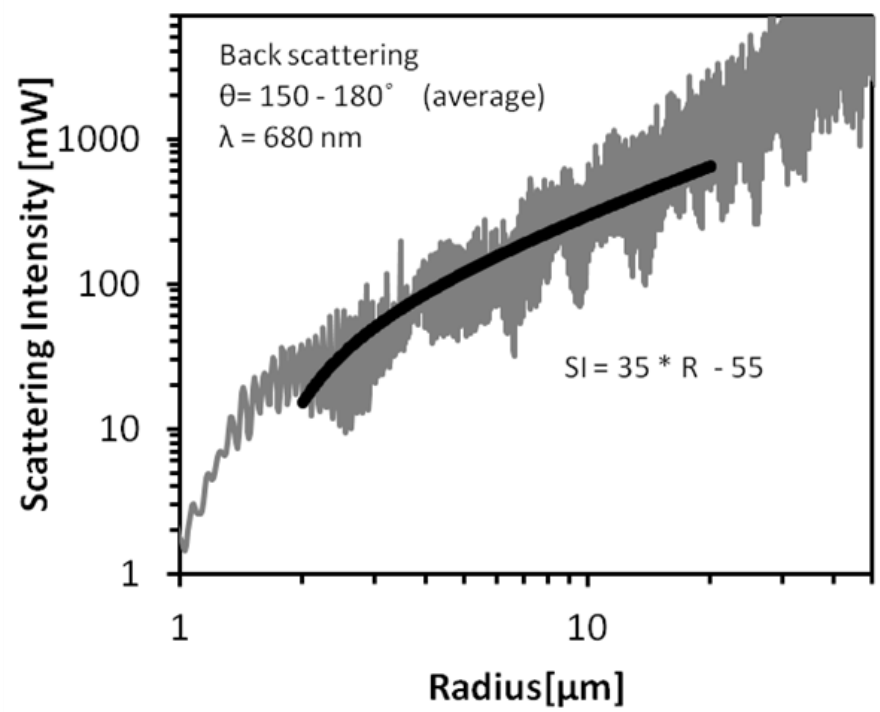

Fig. 3.17 Theoretical relationship between the particle radius and the backscattering intensity, assuming the Mie scattering process. Black line indicates a linear fit.

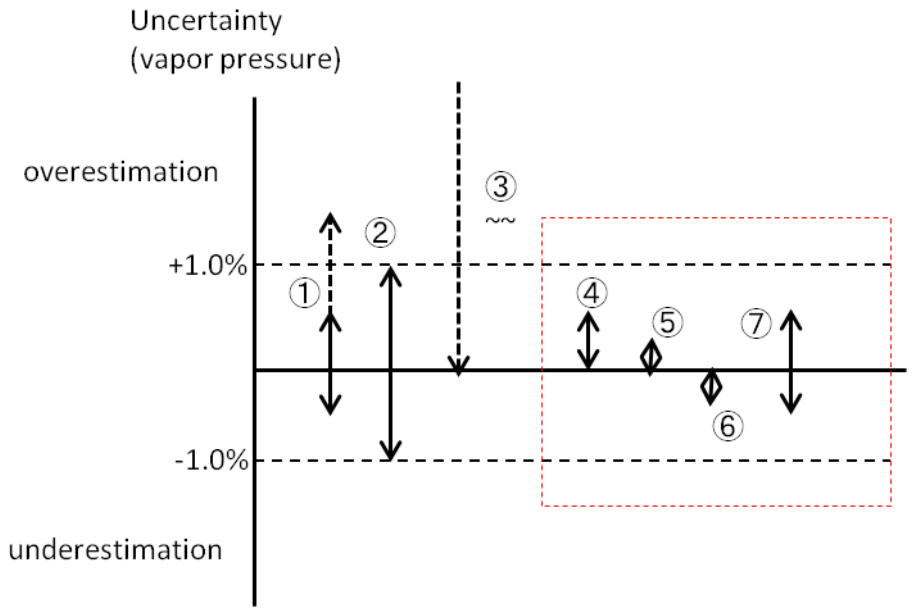

Fig. 3.18 Sources of the measurement uncertainty and its degree. The degree indicates the error of the vapor pressure calculated from the frost point temperature. (1) the mirror temperature measurement, (2) the stability and response of the PID controller, (3) the contamination error by cloud/rain droplet, (4) the ambiguity of the condensate phase, (5) aerosol effects, (6) curvature effect, (7) the uncertainty of the vapor equation s.

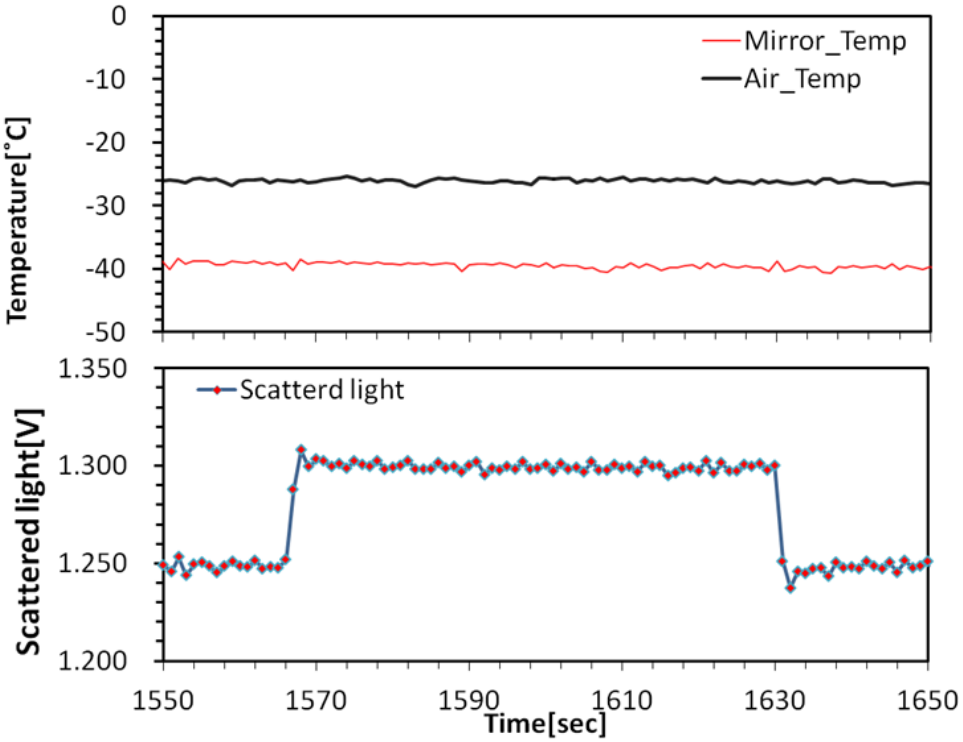

Fig. 3.19 Response of the scattered light intensity for the step functions of the target level of the scattered light intensity (1.25 --> 1.30 --> 1.25). Time series of air temperature and mirror temperature (top) and intensity of scattered light(bottom). For these cases, the stabilization time is within 3 sec.

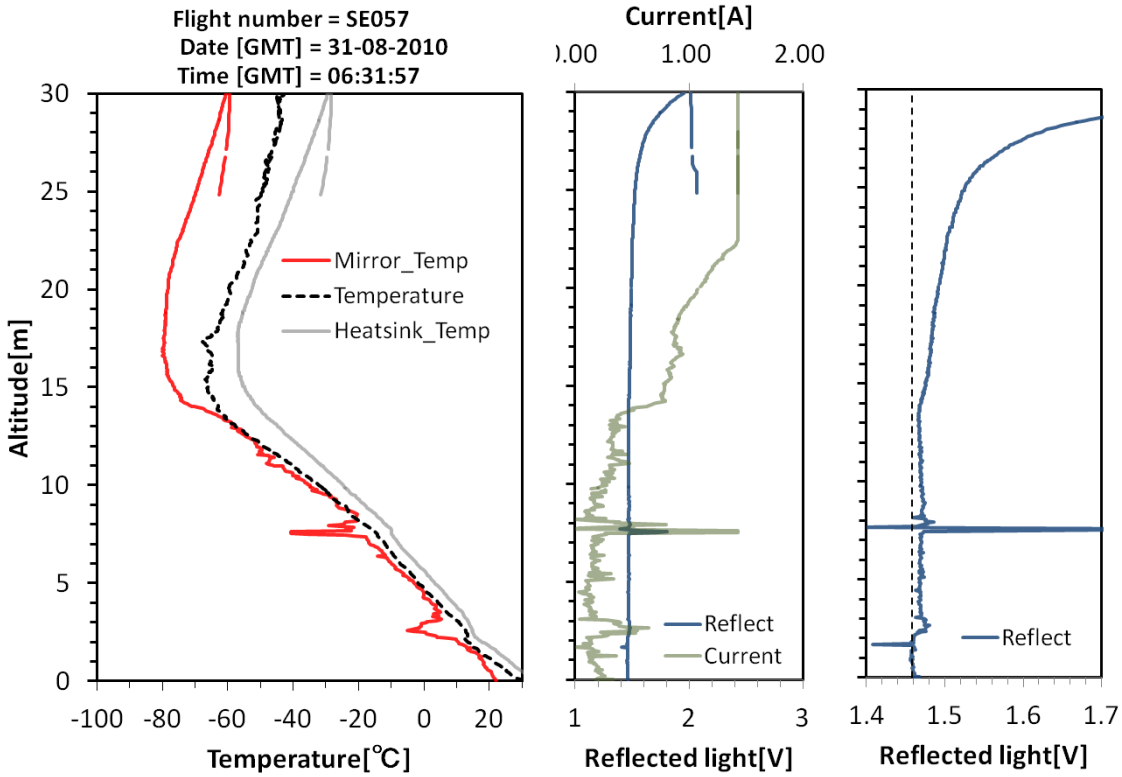

Fig. 3.20 An example of the observed profiles from the Snow White hygrometer. taken at Sapporo on 31 August 2013 (left). Mirror temperature and air temperature, (middle) peltier current and the intensity of the reflected light as housekeeping data, (right) the close-up (note the horizontal axis) of the reflected light

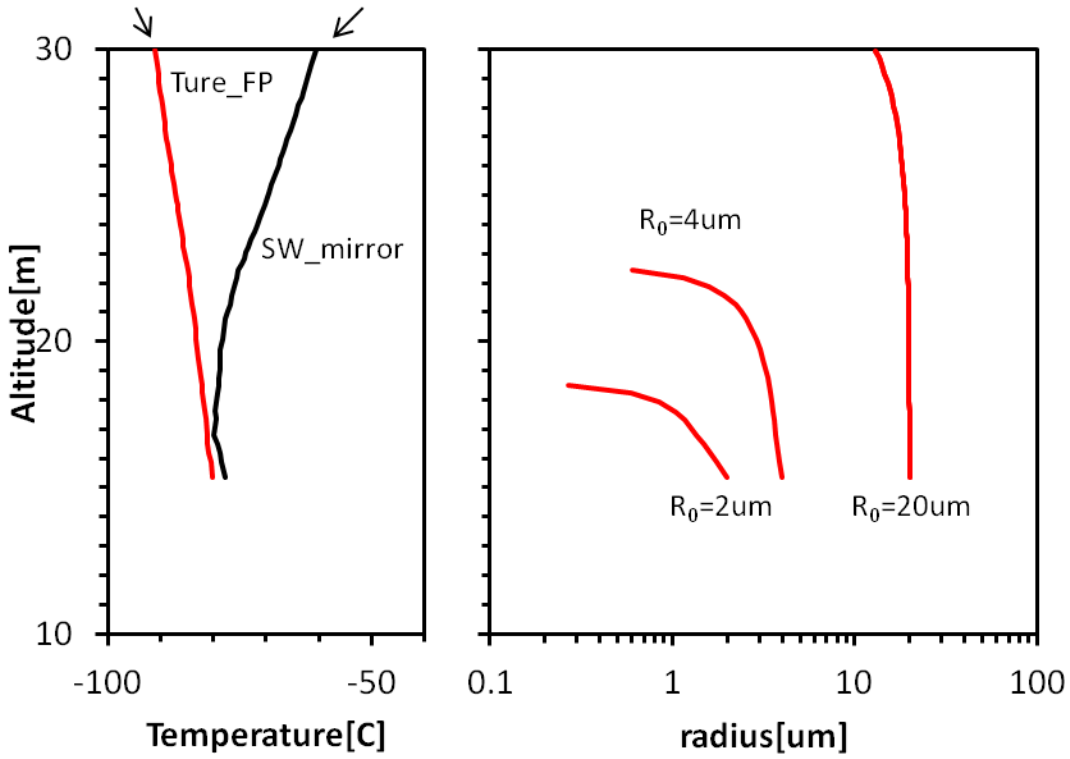

Fig. 3.21 Evaporation rate of a condensate on the mirror calculated with a simple model, assuming that the ice crystal is spherical shape. See text for the details.

Chapter 4
Summary

To assess the uncertainty of water vapor measurements from operational upper-air observation, and to improve the accuracy of the atmospheric water vapor measurements for climate monitoring, the author conducted the following researches:

In Chapter 2, the author investigated the measurement uncertainty of the Meisei RS-06G. Comparisons of RH measurements from the RS-06G radiosonde and from a chilled mirror hygrometer revealed that the RS-06G RH shows a stepwise change of ~ 3% RH at 0 °C. This is due to a discontinuous correction factor in the processing software that compensates for the temperature dependence of the RH sensor. Using the results from chamber experiments, the author developed a new temperature-dependence (T-D) correction to resolve the artificial stepwise change at 0 ˚C. Because the RS-06G radiosonde is a successor to the Meisei's previous radiosonde, RS-01G and RS2-91, on which the same RH sensor material had been installed since July 1999, the new T-D correction should be applied to the data obtained by these radiosondes as well. The author applied the new correction into the data at Japan Metrological Agency's Sapporo and Tateno stations. Because the original T-D correction has only been applied only since February 2003, the time series of RH at both stations showed apparent large downward trends between 1999 and 2009. The new T-D correction was found to result in a much smaller downward RH trend at Sapporo and almost no trend at Tateno. However, this correction does not consider

the solar radiation heating during daytime observations, contamination by cloud droplets, or slow sensor response at low temperatures. To further reduce uncertainties in humidity trends, we need more laboratory experiments and in-flight comparisons with reference instruments such as a chilled-mirror hygrometer. In addition, to extend our analysis over longer periods, we need to investigate the biases between the RS2-91 and the older radiosonde models.

In Chapter 3, a Peltier-based digitally-controlled chilled-mirror hygrometer has been developed. The developed chilled-mirror hygrometer is environmentally-friendly and easy-to-handle in nature because this instrument does not use a cryogenic material to cool the mirror. Since January 2011, we have conducted nine test flights to evaluate the performance. These results showed that the developed chilled-mirror hygrometer can measure the lower stratospheric water vapor by the current Peltier cooling system. We need to reduce large oscillations in the UT/LS by a further PID tuning to reduce the measurement uncertainty. The author has also conducted several chamber and laboratory experiments. The observation of the condensates on the mirror shows that smaller ice crystals form at lower temperatures. Because the particle size affects the response time, the author recognized a need to prevent large ice crystals from forming at the phase transient by making the heating algorithm some time at a flight. This algorithm was found to result in a faster response.

The author was able to obtain deeper understanding of the behavior of the chilled-mirror hygrometers through this development. The chilled-mirror hygrometer is often considered as an accurate hygrometer, but there are several problems that remain to be solved. The problem includes the evaluation of the PID

controller, contamination errors by the cloud, aerosol effects. At the same time, we need to consider the improvement in the instrument production processes and the cost-cutting for long-term climate monitoring.

Accurate water vapor measurements are important for various objectives such as the understanding of cloud microphysical processes and long-term trend detections. Systematic biases among various instruments hinder the application of measurement data from different types of hygrometers for the detection of long-term trends. In the troposphere, operational radiosonde sensors have large measurement uncertainties discussed in Capture 2. In the UT/LS, large discrepancies among instruments remain unresolved in spite of many years of efforts (e.g., Fahey et al. 2009; Rollins et al. 2014). The further reduction of systematic biases is critical for detecting the trends in atmospheric water vapor robustly. In the near future, the use of the hygrometer developed in this study is expected to contribute to resolving the issues of discrepancies among instruments through intercomparisons, if the remaining problems as discussed above are solved.

Appendix A.

Several equations exist for the vapor pressure of water or ice (Murphy and Koop 2005). Here, we use Buck's equations (Buck 1981) because they are used by the manufacturer to calibrate the RS-06G. Buck's equations are written as

$$e_w = f_w \times 6.1121\exp\left(\frac{17.502T}{240.97+T}\right) \quad \text{(A.1)}$$

$$e_i = f_i \times 6.1115\exp\left(\frac{22.452T}{272.55+T}\right) \quad \text{(A.2)}$$

and

$$f_w = 1.0007 + (3.46 \times 10^{-6} P) \quad \text{(A.3)}$$

$$f_i = 1.0003 + (4.18 \times 10^{-6} P) \quad \text{(A.4)}$$

where e_w and f_w are the water vapor pressure and the enhancement factor over the surface of liquid water, respectively, while e_i and f_i are those over the surface of ice, respectively. Units are °C for temperature, T, and mb (= hPa) for pressure, P. f_w and f_i correct the differences of saturation vapor pressure between pure water vapor and moist air. This correction is a weak function of temperature and pressure, averaging $f \sim 1.005$ near sea level. However, in the manufacturer's calibration and in this study, the enhancement factor is set to $f = 1$. This approximation holds with an error 0.5 % or less (WMO, 2008).

Appendix B

We estimate the measurement uncertainties associated with this study by following the guidelines in JCGM/WG1 (2008).

First, we attempt to identify the likely sources of uncertainty and express them as a standard uncertainty. In this work, the major elements of the conceivable

uncertainties are from each instrument's performance, spatial and temporal non-uniformity in the chamber, and reading errors. The accuracy of the RF-100 is ±0.1 °C according to the manufacturer's specifications. We assume that the true value exists within a rectangular ±0.1 °C distribution. Consequently, the standard uncertainty of the reference temperature measurement u_{T0} becomes

$$u_{T0} = \frac{0.1}{\sqrt{3}} = 0.058\,°C \quad \text{(B.1)}.$$

For the reference dew point sensor FDW10, the accuracy is ±0.5 °C. The standard uncertainty of the reference dew point measurements is u_{m0}, which is

$$u_{m0} = \frac{0.5}{\sqrt{3}} = 0.29\,°C \quad \text{(B.2)}.$$

To assess the uncertainty from the spatial and temporal non-uniformity in the PVC pipe, we measure the temperature and RH at three points within the pipe using the same RS-06G and obtain temperatures of +17.6 °C, +17.7 °C, and +17.7 °C, and RH levels of 27.1%, 27.3%, and 27.1%. These RH values correspond to dew point temperatures of approximately –1.6 °C, –1.4 °C, and –1.5 °C. Temporal fluctuations during measurement are small and steady, and remain within ± 0.02 °C. Consequently, we assume that the spatial and temporal non-uniformity of temperature do not exceed 0.1 °C; i.e., the air temperatures in the PVC pipe remain within a rectangular ±0.05 °C distribution, and thus the standard uncertainty u_{T1} becomes

$$u_{T1} = \frac{0.05}{\sqrt{3}} = 0.029\,°C \quad \text{(B.3)}.$$

We assume that the uncertainty of the dew point temperatures due to the spatial and temporal non-uniformity would not exceed 0.2 °C; i.e., the dew point temperatures in the PVC pipe remain within a rectangular ±0.1 °C distribution,

thus the standard uncertainty u_{m1} becomes

$$u_{m1} = \frac{0.1}{\sqrt{3}} = 0.058\ ^{\circ}\text{C} \quad \text{(B.4)}.$$

To estimate the reading errors, we complete five replicate readings for every condition and take the average of the five readings as the measurement value. For the temperature measurements, the standard uncertainties u_{T2} from the readings becomes

$$u_{T2} = \frac{s}{\sqrt{n}} = 0.029 \text{ to } 0.071\ ^{\circ}\text{C} \quad \text{(B.5)}$$

where s is the standard deviation, and n is the frequency of measurement (i.e., $n = 5$). For the dew point measurements, the standard uncertainties u_{m2} from the readings becomes

$$u_{m2} = \frac{s}{\sqrt{n}} = 0.029 \text{ to } 0.13\ ^{\circ}\text{C} \quad \text{(B.6)}.$$

Next, we determine the combined standard uncertainty from these three separate factors. The combined standard uncertainty of temperature measurement, u_T, is

$$u_T = \sqrt{{u_{T0}}^2 + {u_{T1}}^2 + {u_{T2}}^2} = 0.065 \text{ to } 0.096\ ^{\circ}\text{C} \quad \text{(B.7)}.$$

The combined standard uncertainty of dew point measurement, $u_{m,}$ is

$$u_m = \sqrt{{u_{m0}}^2 + {u_{m1}}^2 + {u_{m2}}^2} = 0.29 \text{ to } 0.32\ ^{\circ}\text{C} \quad \text{(B.8)}.$$

Furthermore, we calculate the combined standard uncertainty of RH using the law of propagation of uncertainty. The combined standard uncertainty of RH, u_{RH}, is written as

$$u_{RH} = \sqrt{\left(\frac{\partial \text{RH}}{\partial \text{T}_\text{a}}\right)^2 {u_T}^2 + \left(\frac{\partial \text{RH}}{\partial \text{T}_\text{m}}\right)^2 {u_m}^2} = 0.36\% \text{ to } 1.7\% \text{ RH} \quad \text{(B.9)}.$$

To determine the expanded uncertainty, we use $k = 2$ as level of confidence. Thus, the expanded uncertainty of RH, U_{RH}, becomes

$$U_{RH} = k \times u_{RH} = 0.72\% \text{ to } 3.4\% \text{ RH} \quad \text{(B.10)}.$$

The values of U_{RH} for each condition are shown in Fig. 2.4.

Appendix C

The results of all the flight tests are provided in Appendix C.

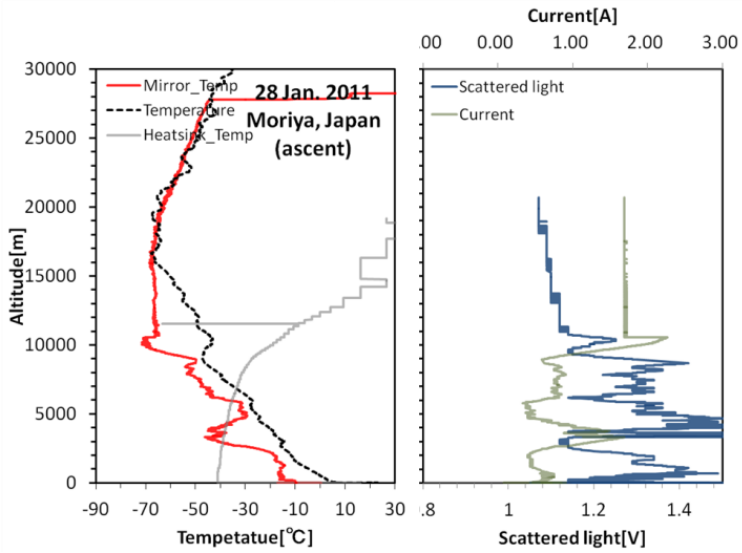

Fig. C.1 A profile of the 1st sounding taken at Moriya, Japan on 28 January 2011(daytime, 14:30LT).

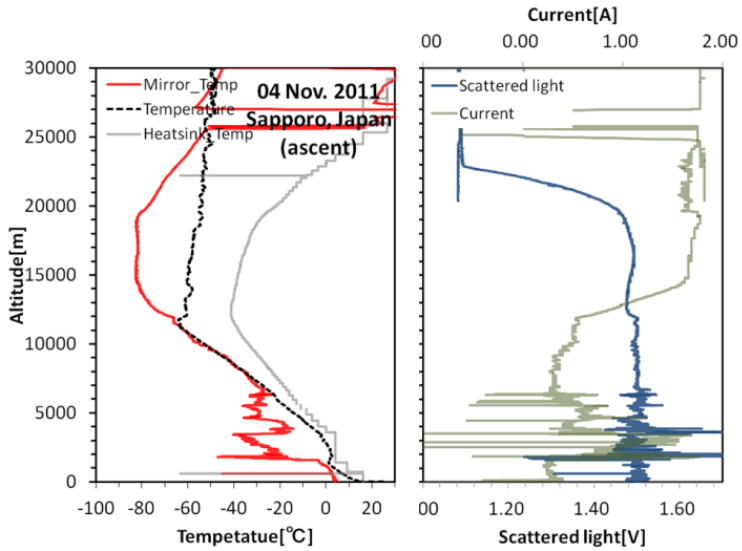

Fig. C.2 A profile of the 2nd sounding taken at Sapporo, Japan on 4 November 2011 (daytime, 14:01LT).

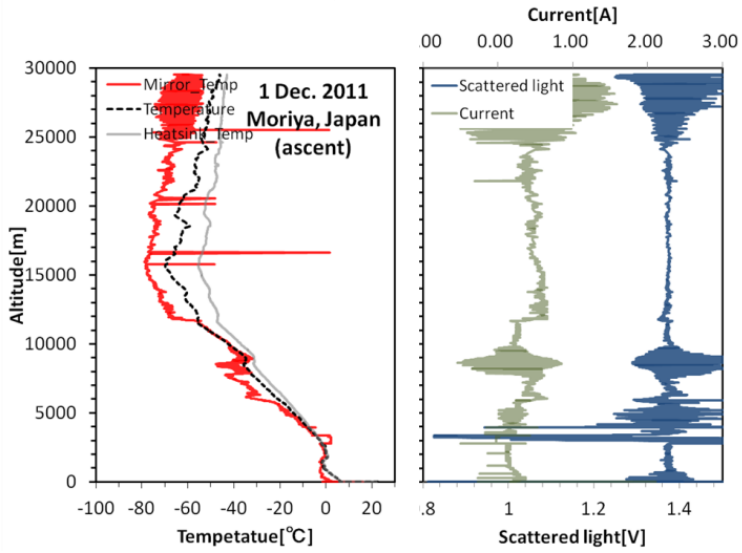

Fig. C.3　A profile of the 3rd sounding taken at Moriya, Japan on 1 December 2011 (nighttime, 17:41LT).

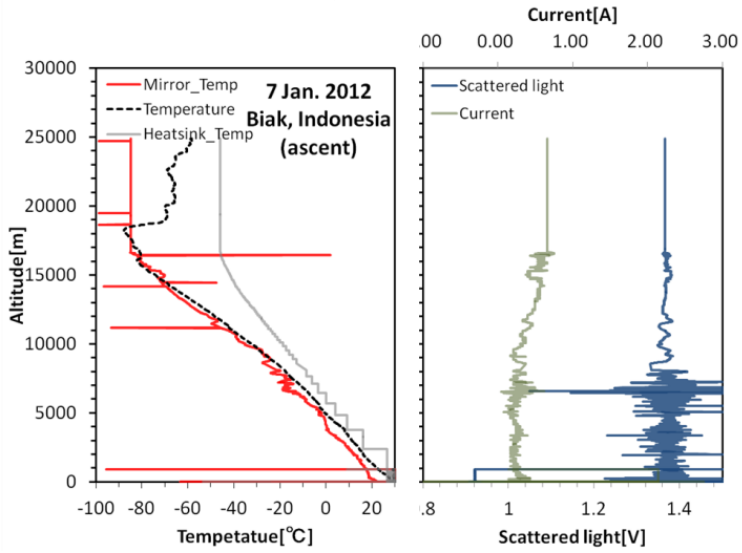

Fig. C.4　A profile of the 4th sounding taken at Biak, Indonesia on 7 January 2012 (daytime, 17:27LT).

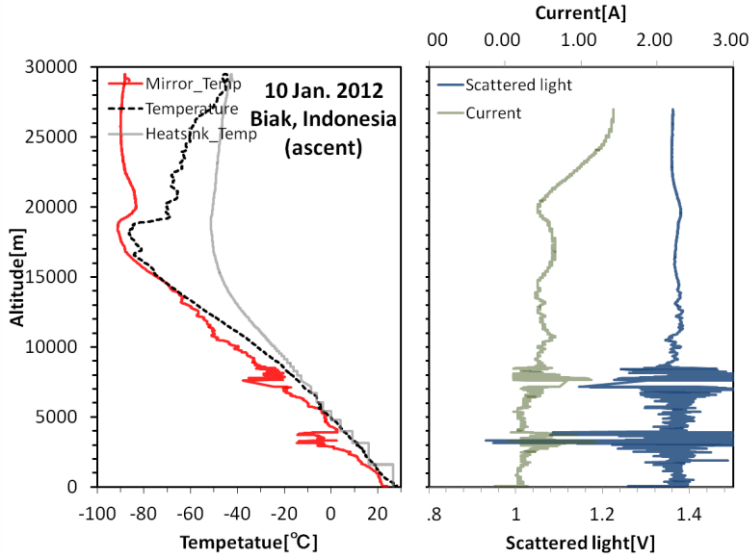

Fig. C.5　A profile of the 5th sounding taken at Biak, Indonesia on 10 January 2012 (nighttime, 18:42LT).

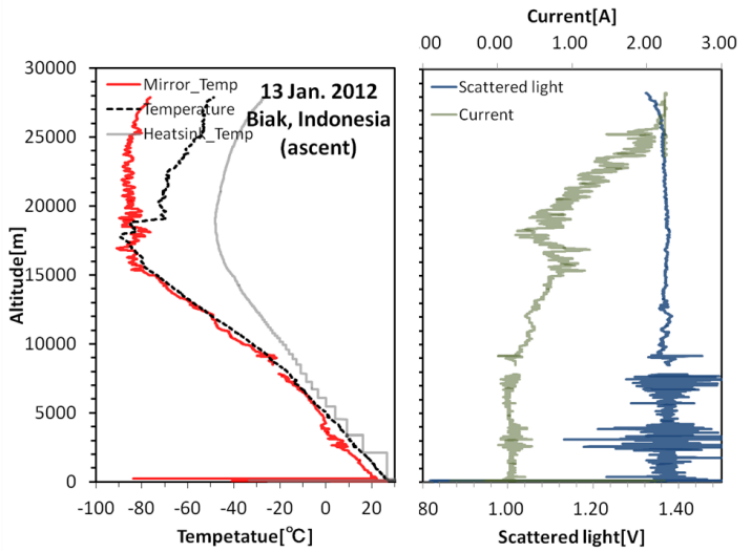

Fig. B.6　A profile of the 6th sounding taken at Biak, Indonesia on 13 January 2012 (daytime, 15:49LT)..

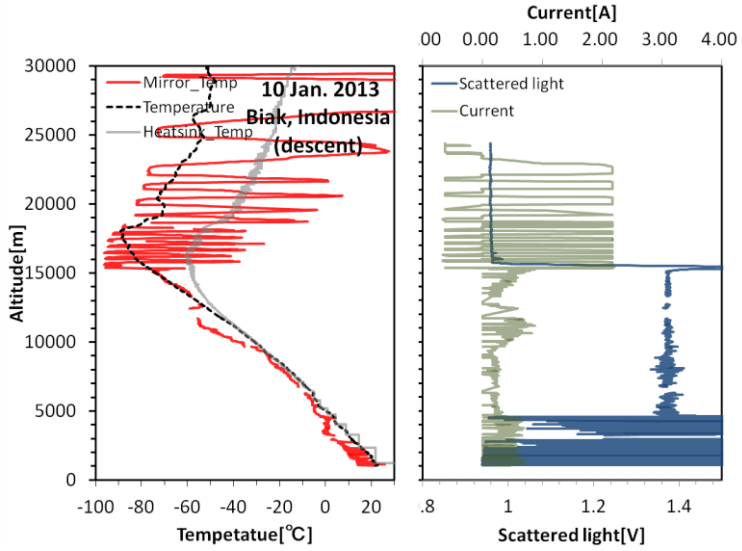

Fig. B.7　A profile of the 7th sounding taken at Biak, Indonesia on 10 January 2013 (daytime, 18:00LT).

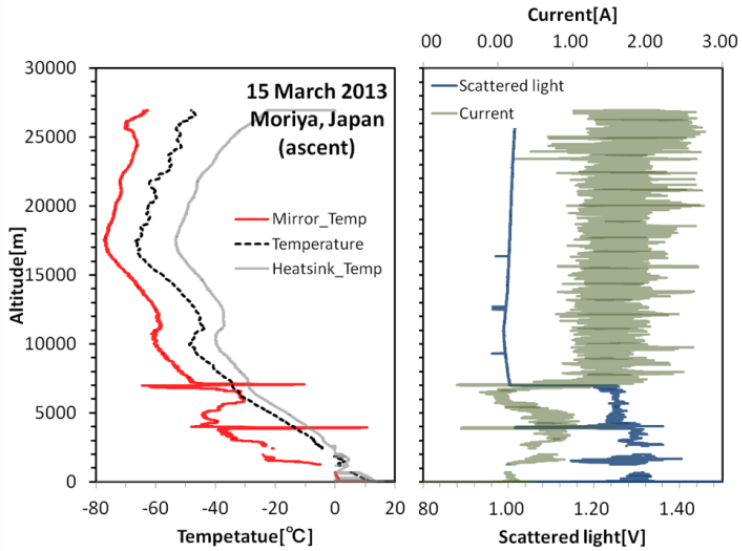

Fig. B.8　A profile of the 8th sounding taken at Moriya, Japan on 25 April 2013 (daytime, 16:40LT).

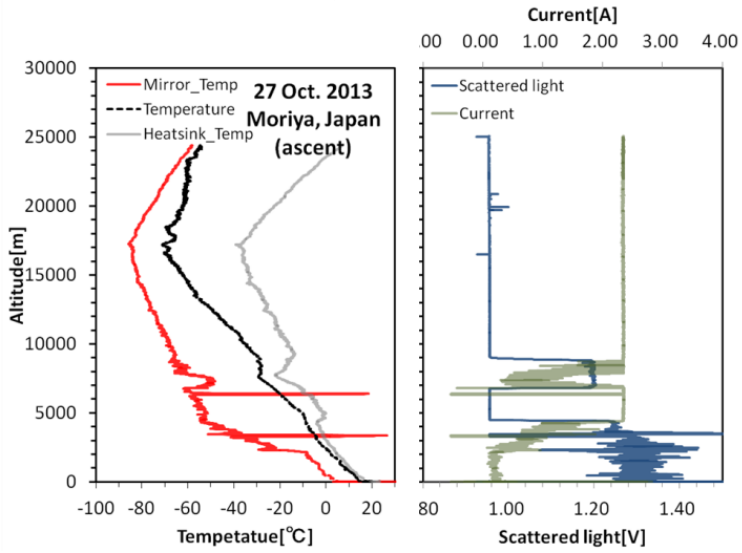

Fig. B.9　A profile of the 9th sounding taken at Moriya, Japan on 27 October 2013 (daytime, 9:10LT).

Acknowledgments

The author would like to express my deepest gratitude of Dr. M. Fujiwara for his guidance and support. The author would like to appreciate the collaboration and encouragement from Dr. K. Shimizu of the Meisei Electric Co. Ltd., Mr. M. Ibata and Mr. Y. Kanai of the Azbil Corporation. The author thank the member of the Soundings of Ozone and Water in the Equatorial Region (SOWER) project, the members of Lembaga Penerbangan dan Antariksa Nasional (LAPAN) of Indonesia, and the staff of the Meisei Electric Co. Ltd. for their collaboration at the test soundings. Laboratory experiments were conducted using the facilities of the Meisei Electric Co. Ltd. The RS-06G radiosondes were provided by the Meisei Electric Co. Ltd. The use of the FDW10 was supported by the Azbil Corporation. The author also thank Dr. F. Hasebe, Dr. Y. Fujiyoshi of Hokkaido University, Dr. H. Vömel of GRUAN lead center, Dr. D. Hurst of NOAA, Dr. K. Yoneyama of JAMSTEC, Dr. H. Abe of the National Metrology Institute of Japan, and the SOWER colleagues for providing useful comments and suggestions, and the JMA Aerological Observatory and the Meisei Electric Co. Ltd. for providing information about operational soundings. This work was in part supported by the Japanese Ministry of Education, Culture, Sports, Science and Technology (MEXT) through a Grant-in-Aid for Scientific Research (22740306), and the Institute of Space and Astronautical Science/Japan Aero-space Exploration Agency (ISAS/JAXA).

Finally, the author would like to thank my family for their support and encouragement.

References

Amano, M., 2010: A survey on the measurement methods and standards of trace moisture in gases. Repot of the National Metrology Institute of Japan, Vol. 8, No.3, 331.

Brewer, A. W., 1949: Evidence for a world circulation provided by the measurements of helium and water vapor distribution in the stratosphere. Quart. J. Roy. Meteor. Soc., 75, 351–363.

Buck, A. L. 1981: New equations for computing vapor pressure and enhancement factor, J. Appl. Meteorol., 20, 1527-1532.

Bolton, D., 1980: The computation of equivalent potential temperature. *Mon. Wea. Rev.*, **108**, 1046–1053.

Craig, F. B., Donald, R. H.., 1983: Absorption and Scattering of Light by Small Particles, A Wiley-Interscience Publication, 530pp.

Cziczo D. J., Froyd K. D., Hoose C., Jensen E. J.., Diao M., Zondlo M. A. , Smith J. B., Twohy C. H., Murphy D. M.. 2013: Clarifying the dominant sources and mechanisms of cirrus cloud formation, Science. 349, 1320-4.

Dai, A., J. Wang, P. W. Thorne, D. E. Parker, L. Haimberger, and X. L. Wang, 2011: A new approach to homogenize daily radiosonde humidity data. *J. Climate,* **24**, 965–991.

Dee D. P., and Coauthors, 2011: The ERA-Interim reanalysis: configuration and performance of the data assimilation system, Quart. J. Roy. Meteor. Soc., 137, 553-597.

Durre, I., R. S. Vose, and D. B. Wuertz, 2006: Overview of the Integrated Global Radiosonde Archive. J. Climate, 19, 53–68.

Elliott, W. P., 1995: On detecting long-term changes in atmospheric moisture, Climatic Change, 31, 349-367.

Fahey, D. W., R. S. Gao, and O. Möhler, 2009: Summary of the AquaVIT Water Vapor Intercomparison: Static Experiments. https://aquavit.icg.kfa-juelich.de/WhitePaper/AquaVITWhitePaper_Final_23Oct2009_6MB.pdf

Fueglistaler, S., Y.S. Liu, T.J. Flannaghan, P.H. Haynes, D.P. Dee, W.J. Read, E.E. Remsberg, L.W. Thomason, D.F. Hurst, J.R. Lanzante, P.F. Bernath 2013: The relation between atmospheric humidity and temperature trends for stratospheric water, J. Geophys. Res., 118, 1052-1074.

Fujiyoshi, Y. 2010: Update of radiosonde sensor and appearance frequency of upper-level cloud, *TENKI*, **57**, 511-512. (in Japanese)

Fujiwara, M., M. Shiotani, F. Hasebe, H. Vömel, S. J. Oltmans, P. W. Ruppert, T. Horinouchi, and T. Tsuda, 2003: Performance of the Meteolabor "Snow White" chilled-mirror hygrometer in the tropical troposphere: Comparisons with the Vaisala RS80 A/H-Humicap sensors, J. Atmos. Oceanic Technol., 20, 1534-1542., doi:10.1175/1520-0426(2003)020<1534:POTMSW>2.0.CO;2.

Fujiwara, M., H. Vömel, F. Hasebe, M. Shiotani, S.-Y. Ogino, S. Iwasaki, N. Nishi, T. Shibata, K. Shimizu, E. Nishimoto, J. M. Valverde-Canossa, H. B. Selkirk, and S. J. Oltmans, 2010: Seasonal to decadal variations of water vapor in the tropical lower stratosphere observed with balloon-borne cryogenic frost point hygrometers, J. Geophys. Res., 115, D18304, doi:10.1029/2010JD014179.

GCOS (Global Climate Observing System), 2009: GRUAN Implementation Plan 2009-2013, GCOS-134, WMO-TD-No. 1506, 53 pp.

http://www.wmo.int/pages/prog/gcos/Publications/gcos-134.pdf

Haimberger L, Tavolato C, Sperka S. 2008: Toward elimination of the warm bias in historic radiosonde temperature records: Some new results from a comprehensive intercomparison of upper-air data. J. Climate, 21, 4587–4606.

Hansford, G. M., Freshwater, R. A., Eden, L., Turnbull, K. F. V., Hadaway, D. E., Ostanin, V. P., and Jones, R. L., 2006: Lightweight dew-/frost-point hygrometer based on a surface-acoustic-wave sensor for balloon-borne atmospheric water vapor profile sounding, Rev. Sci. Instrum., 77, 014502, doi:10.1063/1.2140275.

Held, I. M., and B. J. Soden, 2000: Water vapor feedback and global warming, Annu. Rev. Energy Environ., 25, 441-475.

Houze, R., A., 1993: Cloud Dynamics, Academic Press, California, 573 pp.

Hurst, D. F., S. J. Oltmans, H. Vömel, K. H. Rosenlof, S. M. Davis, E. A. Ray, E. G. Hall, and A. F. Jordan, 2011: Stratospheric water vapor trends over Boulder, Colorado: Analysis of the 30 year Boulder record, J. Geophys. Res., 116, D02306, doi:10.1029/2010JD015065.

Ibata K. and Y. Kanai, 2008: Development of the micro chilled mirror hygrometer, Proceedings of the 5th International Symposium on Humidity and Moisture – ISHM 2006 Brazil on CD-ROM (ISBN 978-85-86920-04-2), index161.

Immler, F. J., J. Dykema, T. Gardiner, D. N. Whiteman, P. W. Thorne, and H. Vömel, 2010: Reference Quality Upper-Air Measurements: guidance for developing GRUAN data products, Atmos. Meas. Technol., 3, 1217–1231, doi:10.5194/amt-3-1217-2010.

Ishihara, M., 2004: Presentation on Recent National Tests/Comparisons. Recent Tests and Comparisons of Radiosonde Operated by Japan Meteorological Agency.

WMO commission for instruments and methods of observation, Papers presented at the joint meeting of the CIMO expert team on upper-air systems intercomparisons and the international organizing committee on upper-air systems intercomparisons, 8 pp, http://www.wmo.int/pages/prog/www/IMOP/meetings/Upper-Air/Systems-Intercomp/Doc3-2(3).pdf

Jakob, C., 2002: Ice clouds in numerical weather prediction models: Progress, problems, and prospects. Cirrus, D. K. Lynch et al., Eds., Oxford University Press, 480pp.

Japan Meteorological Agency, 1995: *Manual Guide of Upper-air Observation*. Japan Meteorological Agency (in Japanese).

Japan Meteorological Agency, 2012: *Climate Change Monitoring Report 2011*. Japan Meteorological Agency, 59-60. (in Japanese)

JCGM/WG 1 (Joint Committee for Guides in Metrology/ Working Group 1), 2008: Evaluation of measurement data – Guide to the expression of uncertainty in measurement, 100, 134 pp., http://www.bipm.org/utils/common/documents/jcgm/JCGM_100_2008_E.pdf

Jensen, E., and L. Pfister, 2005: Transport and freeze-drying in the tropical tropopause layer. J. Geophys. Res. 109, D02207

Jensen, E., J. B. Smith, L. Pfister1, J. V. Pittman, E. M. Weinstock, D. S. Sayres, R. L. Herman, R. F. Troy, K. Rosenlof, T. L. Thompson, A. M. Fridlind, P. K. Hudson, D. J. Cziczo, A. J. Heymsfield, C. Schmitt, and J. C. Wilson, 2005: Ice supersaturations exceeding 100% at the cold tropical tropopause: Implications for cirrus formation and dehydration. Atmos. Chem. Phys. 5, 851–862

Kley. D., and E. Stone, 1978: Measurements of water vapor in the stratosphere by photodissociation with Ly-a (1216 A) light, Rev. Sci. Instrum, 49, 691-697, doi:10.1063/1.1135596.

Kobayashi, E., Y. Noto, S. Wakino, H. Yoshii, T. Ohyoshi, S. Saito, Y. Baba, 2012: Comparison of Meisei RS2-91 rawinsondes and Vaisala RS92-SGP radiosondes at Tateno for the data continuity for climatic data analysis. *J. Meteor. Soc. Japan*, **90**, 923-945.

Korolev, A. V., and I. P. Mazin, 2003: Supersaturation of water vapor in clouds. J. Atmos. Sci., 60, 2957–2974.

Mastenbrook, H. J., and S. J. Oltmans, 1983: Stratospheric Water vapor variability for Washington DC/Boulder, CO: 1964-82, J. Atmos. Sci., 40, 2157-2165., doi:10.1175/1520-0469(1983)040<2157:SWVVFW>2.0.CO;2.

Murphy, D., and T. Koop, 2005: Review of the vapour pressures of ice and supercooled water for atmospheric applications. Quart. J. Roy. Meteor. Soc., 131, 1539–1565.

Murray, B. J., Knopf, D. A., and Bertram, A. K., 2005: The formation of cubic ice under conditions relevant to earth's atmosphere, Nature, 434, 202–205, doi:10.1038/nature03403,

Murray, B. J., Wilson, T. W., Dobbie, S., Cui, Z. Q., Al-Jumur, S., M¨ohler, O., Schnaiter, M., Wagner, R., Benz, S., Niemand, M., Saathoff, H., Ebert, V., Wagner, S., and Karcher, B. 2010: Heterogeneous nucleation of ice particles on glassy aerosols under cirrus conditions, Nature Geosci., 3, 233–237, doi:10.1038/ngeo817,

Miloshevich, L. M., H. Vömel, A. Paukkunen, A. J. Heymsfield, and S. J. Oltmans,

2001: Characterization and Correction of Relative Humidity Measurements from Vaisala RS80-A Radiosondes at Cold Temperatures. J. Atmos. Oceanic Technol., 18, 135-156.

Miloshevich, L. M., A. Paukkunen, H. Vömel, and S. J. Oltmans, 2004: Development and validation of a time-lag correction for Vaisala radiosonde humidity measurements. J. Atmos. Oceanic Technol., 21, 1305-1327.

Miloshevich, L., H. Vömel, D. Whiteman, B. Lesht, F. Schmidlin and F Russo, 2006: Absolute accuracy of water vapor measurements from six operational radiosonde types launched during AWEX-G and implications for AIRS validation, J. Geophys. Res., 111, D09S10, doi:10.1029/2005JD006083.

Miloshevich, L. M., H. Vömel, D. N. Whiteman, and T. Leblanc, 2009: Accuracy assessment and correction of Vaisala RS92 radiosonde water vapor measurements. J. Geophys. Res., 114, D11305, doi:10.1029/2008JD011565.

Montzka, S. A., L. Kuijpers, M. O. Battle, M. Aydin, K. R. Verhulst, E. S. Saltzman, and D. W. Fahey, 2010: Recent increases in global HFC-23 emissions. Geophys. Res. Lett., 37, L02808, doi:10.1029/2009GL041195.

Morrissey, J. F. and F. J. Brousaides, 1970: Temperature-induced errors in the ML-476 humidity data, J. Appl. Meteor., 8, 805-808.

Murphy, D., and T. Koop, 2005: Review of the vapour pressures of ice and supercooled water for atmospheric applications. Quart. J. Roy. Meteor. Soc., 131, 1539–1565., doi:10.1256/qj.04.94.

NOAA (National Oceanic and Atmospheric Administration), NASA (National Aeronautics and Space Administration), and USAF (United States Air Force), 1976: U. S. Standard Atmosphere, U. S. Government Printing Office, Washington,

D.C., 227pp.

Oltmans, S., H. Vömel, D. Hofmann, K. Rosenlof, and D. Kley, 2000: The increase in stratospheric water vapor from balloonborne frostpoint hygrometer measurements at Washington, D. C., and Boulder, Colorado, Geophys. Res. Lett., 27, 3453–3456, doi:10.1029/2000GL012133.

Orikasa, N., and M. Murakami, 1997: A new version of hydrometeor videosonde for cirrus cloud observations. J. Meteor. Soc. Japan, 75, 1033-1039.

Peter, T., C. Marcolli, P. Spichtinger, T. Corti, M. Baker, T. Koop, 2006: When Dry Air Is Too Humid. Science, 5804, 1399-1402.

Pruppacher, H. R., and J. D. Klett, 1997: Microphysics of Clouds and Precipitation. 2nd ed., Kluwer Academic Publishers, Dordrecht, 954pp.

Rollins1 A. W., T. D. Thornberry, R. S. Gao, J. B. Smith, D. S. Sayres, M. R. Sargent, C. Schiller, M. Krämer, N. Spelten, D. F. Hurst, A. F. Jordan, E. G. Hall, H. Vömel, G. S. Diskin, J. R. Podolske, L. E. Christensen, K. H. Rosenlof, E. J. Jensen, D. W. Fahey, 2014: Evaluation of UT/LS hygrometer accuracy by intercomparison during the NASA MACPEX mission, J. Geophys. Res., doi: 10.1002/2013JD020817

Sakota Y., K. Naganuma, Y. Hagiwara, N. Inoue, A. Mita, 1999: RS-91 rawinsonde, *Meteorological Research Note*, **194**, 3-24. (in Japanese)

Schroeder, S. R., 2008: Adjusting archived radiosonde data using complete validated and inferred radiosonde metadata to compute unbiased atmospheric temperature and moisture trends, 20th Conference on Climate Variability and Change, New Orleans, Pester P4.5, https://ams.confex.com/ams/88Annual/techprogram/paper_130838.htm

Seidel,D. J., F.H. Berger,H. J.Diamond, J.Dykema,D. Goodrich, F. Immler,W.Murray, T. Peterson,D. Sisterson,M. Sommer, P. Thorne, H.Vömel, and J.Wang, 2009: Reference upper-air observations for climate: rationale, progress, and plans. *Bull Am. Meteorol. Soc.*, **90**, 361–369.

Sherwood, Steven C., 2007: Simultaneous detection of climate change and observing biases in a network with incomplete sampling. *J. Climate*, **20**, 4047–4062.

Shibue, N., T. Abe, and N. Kizu, 2000: Comparison of new and old type humidity sensors for RS2-91 radiosonde. (in Japanese). Tech. Rep. Aerol. Obs., 60, 9–16.

Shimizu K., T.Asanuma, K.Yamaguchi, and K.Yoshikawa, 2008: Upgraded Thermistor for Unbiased Measurements -Evaluation of New GPS Radiosonde RS-06G, IOM 97, Papers presented at the WMO technical Conference on Instruments and Methods of observation (TECO 2008), http://www.wmo.int/pages/prog/www/IMOP/publications/IOM-96_TECO-2008/P1(09)_Shimizu_Japan.pdf

Soden, B. J., D. L. Jackson, V. Ramaswamy, M. D. Schwarzkopf, and X. Huang, 2005: The radiative signature of upper tropospheric moistening. *Science*, **310**, 841-844.

Solomon, S., K. Rosenlof, R. Portmann, J. Daniel, S. Davis, T. Sanford, and G.-K. Plattner, 2010: Contributions of stratospheric water vapor to decadal changes in the rate of global warming, Science, 327, 1219–1223, doi:10.1126/science.1182488.

SPARC (Stratospheric Processes And their Role in Climate), 2000: SPARC assessment of upper tropospheric and stratospheric water vapour (Kley, D., J. M. Russell, and C. Phillips, eds.), WCRP 113, 312 pp., World Meteorol. Organ., Geneva, Switzerland.

Sugidachi, T. and M. Fujiwara, 2013: Correction of the stepwise change observed at 0˚C in Meisei RS2-91, RS-01G, and RS-06G radiosonde relative humidity profiles. *J. Meteor. Soc. Japan,* **91**, 323-336.

Sugidachi, T., 2011: Development of a balloon-borne hygrometer for climate monitoring, master's thesis at Graduate school of Environmental Science, Hokkaido University, 138 pp. (*in Japanese*) http://wwwoa.ees.hokudai.ac.jp/~takuji-sugi/doc/M-ron_all.pdf

Szak´all, M., Bozoki, Z., Kraemer, M., Spelten, N., Moehler, O., and Schurath, U., 2001: Evaluation of a Photoacoustic Detector for Water Vapor Measurements under Simulated Tropospheric/Lower Stratospheric Conditions, Environ. Sci. Technol., 35, 4881–4885.

Thornberry, T., Gierczak, T., Gao, R. S., V¨omel, H., Watts, L. A., Burkholder, J. B., and Fahey, D. W., 2011: Laboratory evaluation of the effect of nitric acid uptake on frost point hygrometer performance, Atmos. Meas. Tech., 4, 289–296, doi:10.5194/amt-4-289-2011.

Trenberth, K., J. Fasullo, and L. Smith, 2005: Trends and variability in column-integrated atmospheric water vapor. *Clim. Dyn.,* **24**, 741-758.

Vömel, H., S. J. Oltmans, D. Kley, and P. J. Crutzen, 1995b: New evidence for the stratospheric dehydration mechanism in the equatorial Pacific, Geophys. Res. Lett., 22, 3235–3238, doi:10.1029/95GL02940.

Vömel. H, M. Fujiwara, M. Shiotani, F. Hasebe, S. J. Oltmans, and J. E. Barnes, 2003: The Behavior of the Snow White Chilled-Mirror Hygrometer in Extremely Dry Conditions, J. Atmos. Oceanic Technol, 20 1560-1567., doi:10.1175/1520-0426(2003)020<1560:TBOTSW>2.0.CO;2

Vömel, H., D. E. David, and K. Smith, 2007a: Accuracy of tropospheric and stratospheric water vapor measurements by the cryogenic frost point hygrometer: Instrumental details and observations, J. Geophys. Res., 12, D08305.

Vömel, H., H. Selkirk, L. Miloshevich, J. Valverde-Canossa, J. Valdés, E. Kyrö, R. Kivi, W. Stolz, G. Peng, and J. A. Diaz, 2007b: Radiation dry bias of the Vaisala RS92 humidity sensor. J. Atmos. Oceanic Technol., 24, 953-963.

Vömel, H., V. Yushkov, S. Khaykin, L. Korshunov, E. Kyrö, and R. Kivi, 2007b: Intercomparisons of Stratospheric Water Vapor Sensors: FLASH-B and NOAA/CMDL Frost-Point Hygrometer. J. Atmos. Oceanic Technol., 24, 941–952., doi:10.1175/JTECH2007.1.

Wang, J., H. L. Cole, D. J. Carlson, E. R. Miller, K. Beierle, A. Paukkunen, and T. K. Laine, 2002: Corrections of humidity measurement errors from the Vaisala RS80 Radiosonde-Application to TOGA COARE data. J. Atmos. Oceanic Technol., 19, 981–1002.

Wang, J., L. Zhang, A. Dai, F. Immler, M. Sommer, and H. Vömel, 2013: Radiation dry bias correction of Vaisala RS92 humidity data and its impacts on historical radiosonde data. *J. Atmos. Oceanic Technol.*, **30**, 197–214

Whiteman D., Kevin C. Vermeesch, Luke D. Oman, Elizabeth C. Weatherhead. 2011: The relative importance of random error and observation frequency in detecting trends in upper tropospheric water vapor, J. Geophys. Res. 116, D21118

Williams, S. L., and D. T. Acheson, 1976: Thermal Time Constants of U.S Radiosonde Sensors Used in GATE, NOAA technical memorandum EDS CEDDA-7, NOAA (National Oceanic and Atmospheric Administration) EDS (Environmental Data Service) CEDDA (Center for Experiment Design and Data

Analysis), Washington, DC, 16 pp.

WMO (World Meteorological Organization), 1995: Manual on Codes, WMO-No.306, 503 pp. http://www.wmo.int/pages/prog/www/WMOCodes/Manual/WMO306_Vol-I-1-PartA.pdf

WMO (World Meteorological Organization), 2008: Guide to Meteorological Instruments and Methods of Observation -Seventh edition, WMO-No.8 (2008 edition. Update in 2010), 716 pp. http://www.wmo.int/pages/prog/www/IMOP/CIMO-Guide.html

WMO (World Meteorological Organization), 2011: WMO Intercomparison of high quality radiosonde systems Yangjiang, China, 12 July – 3 August 2010, IOM 107 edited by J. Nash, T. Oakley, H. Vömel, LI Wei, 248 pp. http://www.wmo.int/pages/prog/www/IMOP/publications/IOM-107_Yangjiang.pdf

WMO (World Meteorological Organization), 2013: The GCOS Reference UpperAir Network (GRUAN) GUIDE version1.1.0.3, 116pp. http://www.wmo.int/pages/prog/gcos/Publications/gcos-171.pdf#search='WIGOS+GRUAN+guide'

Yoneyama K., M. Fujita, N. Sato, M. Fujiwara, Y. Inai and F. Hasebe, 2008: Correction for radiation dry bias found in RS92 radiosonde data during the MISMO field experiment, SOLA, 4, 13-16.

Yushkov, V., V. Astakhov, and S. Merkulov, 1998: Optical balloon hygrometer for upper-troposphere and stratosphere water vapor measurements. Optical Remote Sensing of the Atmosphere and Clouds, The International Society for Optical Engineering (SPIE Proceedings Vol. 3501), 439–445.

Yushkov, V., S. Merkoulov, V. Astakhov, J. P. Pommereau, and A. Garnier, 2000: A Lyman alpha hygrometer for long duration IR Montgolfier during the Lagrangian-THESEO experiment. Proc. Fifth European Symp. on Stratospheric Ozone, Saint-Jean-de-Luz, France, European Commission, 400–403.

Ziegler, J.G. and N.B. Nichols, 1942: Optimum Settings for Automatic Controllers, Trans. ASME, Vol. 64, pp.759-768.